Title
Hydrological Underpinnings of Mountain Snowpack Responses to Warming Storms

Author
Haleakala, Kayden

Publication Date
2022

Peer reviewed|Thesis/dissertation

UNIVERSITY OF CALIFORNIA

Los Angeles

Hydrological Underpinnings of Mountain Snowpack Responses to Warming Storms

A dissertation submitted in partial satisfaction of the requirements for the degree Doctor of Philosophy in Civil Engineering

by

Kayden Haleakala

2022

ABSTRACT OF THE DISSERTATION

Hydrological Underpinnings

of Mountain Snowpack Responses

to Warming Storms

by

Kayden Haleakala

Doctor of Philosophy in Civil Engineering

University of California, Los Angeles, 2022

Professor Mekonnen Gebremichael, Chair

Midlatitude mountain snowpacks are a critical freshwater resource. However, climate warming is endangering its natural water tower function by decreasing the fraction of winter precipitation falling as snow in an intensifying precipitation regime. In a warmer future, snowpacks may therefore shift from seasonal reservoirs to posing more flood hazards, stressing current ecosystems and water resource management practices. Successful adaptation and hazard preparation to snowpack shifts is predicated on a first-principles understanding of its driving processes. However, most long-term observations and model-projections are incapable of resolving process-level snowpack behaviors, leaving an incomplete toolkit for assessing and interpreting environmental threat levels in snow-fed watersheds. This dissertation addresses this problem by investigating process-level snowpack behaviors during warm storms in California's

Sierra Nevada through sub-daily snow, soil and hydrometeorological measurements, and with supporting observations from atmospheric reanalyses and satellite remote sensing in three studies. The first study delineates an hourly relationship between air temperature, atmospheric moisture, and changes to snow water equivalent (SWE) spanning the Sierra during water years 2010-2019. Conditions balancing precipitable water (humidity) and snowfall requirements (temperature) favor SWE accumulation. SWE increases are observed above 1.0˚C when moisture supplies are modest or snowpacks sufficiently deep, and are otherwise immediately followed by SWE loss. The second study focuses on this SWE "oscillation" in the Northern Sierra during rain-on-snow (ROS) events in January and February 2017. Snowmelt was a weaker driver in ROS flooding than previously documented. Snowpacks may rather "passively" route rainwater through snow, where the saturation and liquid drainage of snow causes observed SWE to rise and immediately fall. The final study elaborates on this case study to other ROS events in water years 2017-2019. Results describe both the limitations common to standard daily observations, and the importance of storm sequencing on augmenting ROS impact. Sierra Nevada watersheds remember large prior storm inputs to soils and streams that imminent storms stand on top of. These observations present a nuanced and integrated perspective to understanding how snowpacks respond to warm storms, which may be beneficial to future water resource and flood risk forecasting interpretations and discussions.

The dissertation of Kayden Haleakala is approved.

Steven Adam Margulis

Jeff Dozier

Dennis P. Lettenmaier

Mekonnen Gebremichael, Chair

University of California, Los Angeles

2022

Table of Contents

List of Figures

List of Tables

ACKNOWLEDGEMENTS

To the unwitting community that assisted in this expedition uphill:

My advisor, Mekonnen Gebremichael – your balancing of guidance against a freedom to explore other trails have been key to my development as a thinker; and the opportunities to teach have been key to my development as a communicator. Thank you for being receptive to unique circumstances and for encouraging me through each challenge as they arrived, both in and outside of research.

My committee members, Steve Margulis, Dennis Lettenmaier, and Jeff Dozier – your coursework and early feedback laid a significant foundation for answering questions. Thank you for all of the insightful discussions that always managed to carve interesting pathways forward or illuminate trail hazards ahead.

Ty Brandt and Benjamin Hatchett – your open arms and willingness to field and test ideas always made research more fun than work. The “keep it simple” principle is something I will continue to practice in my work and life. Thank you for being big brothers in these formative years.

Ed Maurer – you were the role model and impetus of this entire venture. Thank you for all of the early guidance, invigorating conversations, and skill-focused teaching that marked the first few steps along this path.

Friendly colleagues, classmates, and lab mates – Akash Koppa, Sarfaraz Alam, Haowen Yue, Rouhin Mitra, Yu-Chuan Tien, Miguel A.B. Rodriguez, Maria Winters, M.P. Delisle, Joe Lucey, Jacob Schaperow, Yufei Liu, Yiwen Fang, Manon von Kaenel, Dongyue Li, Emilie Tarouilly,

Zhaoxin Ban, Huilin Huang, Jessica Fayne, Mike Fischella, Lu Su, Mu Xiao, Andrew Schwartz, Ned Bair, Timbo Stillinger, and Anne Heggli – thank you for adding your own enriching flavor to this experience.

My family – Malia, James, Princess, and Blaise – you have been supportive in each turn of this adventure irrespective of the outcome. Thank you for always finding time to hear grievances and celebrate successes that sound like a different language.

My brother, Kamana'o – you are always my reminder of what truly matters. Thank you for being my north star.

My wife, Ali – who has been my core temperature at each moment in a long-standing task – you are the strong, compassionate companion that very few are lucky enough to find in one lifetime. Thank you for your uplifting presence at every step.

This body of work itself would not have been possible without the support provided by the UCLA Department of Civil and Environmental Engineering, its Summer Mentored Research Fellowship, and the University of California Research Initiatives UC-National Laboratory Fees Research Program (Award LFR-18-548316).

Co-authors Dennis P. Lettenmaier (DPL), Jeff Dozier (JD), Mekonnen Gebremichael (MG), W. Tyler Brandt (WTB), and Benjamin Hatchett (BH) contributed to completing this dissertation.

Chapter 2 is a version of Haleakala et al. (2021). DPL, JD and I (KH) conceptualized the study; KH conducted the analysis and wrote the manuscript first draft; and MG, DPL, and JD helped revise the manuscript.

Chapter 3 of this dissertation is under review for publication at the time of writing. WTB and KH conceptualized the study and conducted the analysis; KH wrote the first manuscript draft; and BH, DPL and MG helped revise the manuscript.

Chapter 4 of this dissertation is in preparation to be submitted for publication at the time of writing. KH conceptualized the study, conducted the analysis, and wrote the first manuscript draft; and WTB, BH, and MG helped revise the manuscript. MG supervised all chapters.

You have all been instrumental in this climb to the mountaintop.

Thank you everyone – we did it.

VITA

EDUCATION

MS in Civil Engineering (Water Resources), degree with Distinction **June 2017**

Santa Clara University – California

BS in Civil Engineering (Water Resources), Cum Laude **June 2016**

Santa Clara University – California

PEER-REVIEWED PUBLICATIONS

Brandt. W.T., **Haleakala, K.**, Hatchett, B.J., Pan, M. (2022). A review of the hydrologic response mechanisms during mountain rain-on-snow. *Frontiers in Earth Science*, 10, 791760, DOI: 10.3389/feart.2022.791760

Haleakala, K., Yue, H. Mitra, R., Alam, S., Bushara, A.I., Gebremichael, M. (2022). The evolving roles of intensity and wet season timing in rainfall regimes surrounding the Red Sea. *Environmental Research Letters*, 17(14), 044039, DOI:10.1088/1748-9326/ac5560

Haleakala, K., Gebremichael, M., Dozier, J., & Lettenmaier, D. P. (2021). Factors Governing Winter Snow Accumulation and Ablation Susceptibility across the Sierra Nevada (United States). *Journal of Hydrometeorology*, 22(6), 1455-1472, DOI:10.1175/JHM-D-20-0257.1

ARTICLES SUBMITTED / IN REVIEW

Brandt, W.T., Cannon, F., Cooper, A., Delle Monache, L., **Haleakala, K**., Hatchett, B.J., McGurk, B., Pan, M., Ralph, F.M. Complementary observations aid identification of the mountain rain-snow transition. *Geophysical Research Letters*, submitted, preprint DOI: 10.1002/essoar.10510466.1

Haleakala, K., Brandt., W.T., Hatchett B.J., Lettenmaier, D.P., Gebremichael, M. Rain-on-snow was not a major contributor to the Oroville Dam flood of February 2017. *PNAS Nexus*, in review.

RECENT CONFERENCE PRESENTATIONS

(Poster) **Haleakala, K**., Brandt, W.T., Hatchett, B.J., Gebremichael, M. (2022). Presence and Structure of Rain-on-Snow Events in and between Western U.S. Mountain Ranges. Poster presented at Western Snow Conference, Salt Lake City, Utah.

(Oral) **Haleakala, K**., Brandt, W.T., Hatchett, B.J., Gebremichael, M., Lettenmaier, D.P. (2022). A tale of two snowpacks: Active versus passive responses to rain-on-snow. Seminar presented at American Geophysical Union Fall Meeting, New Orleans, Louisiana.

(Oral) Brandt, W.T., Cannon, F., Cooper, A., **Haleakala, K.,** Hatchett, B.J., McGurk, B., Pan, M.. (2021). Grappling with the mountain rain-snow transition: the snow pillow rain-on-snow response. Seminar presented at Yosemite Hydroclimate Workshop, Virtual.

(Oral) **Haleakala, K**., Gebremichael, M., Dozier, J., Lettenmaier, D.P. (2020). Winter Snowpack Responses to Near-Freezing Storms in the Sierra Nevada, U.S.A. Seminar presented at American Geophysical Union Fall Meeting, Virtual.

(Poster) **Haleakala, K**., Gebremichael, M., Dozier, J., Lettenmaier, D.P. (2019). Regional-Scale Controls on Snow Accumulation in the Sierra Nevada, U.S.A. Poster presented at American Geophysical Union Fall Meeting, San Francisco, California.

(Oral) Gebremichael, M., Alam, S., **Haleakala, K**. (2019). Montane and Groundwater Reservoirs Under Climate Change. Seminar presented at Headwaters to Groundwater Forum at University of California, Davis, California.

(Poster) **Haleakala, K**., Gebremichael, M., Margulis, S. (2019) Looking Behind the Curtain of Advanced Snowpack Estimation in the Sierra Nevada, California. Poster presented at International Precipitation Conference 12, University of California, Irvine, California.

RESEARCH & PROFESSIONAL EXPERIENCE

Graduate Student Researcher **January 2018 – Present**

Department of Civil & Environmental Engineering, University of California, Los Angeles – California

Teaching Assistant **January 2020 – April 2020**

Department of Civil & Environmental Engineering, University of California, Los Angeles – California

Water Resources Research Assistant **June 2015 – June 2017**

Department of Civil Engineering, Santa Clara University – California

Graduate Engineering Intern **June 2016 – September 2017**

Watershed Design & Construction, Santa Clara Valley Water District – California

Chapter 1 Introduction

1.1 Background and motivation

Mountain snowpacks provide freshwater to approximately 2 billion people worldwide (Viviroli et al. 2007; Immerzeel et al. 2020). In the Western United States, snowmelt from snow-dominated watersheds provide over 70 percent of runoff (Li et al. 2017). This is a pillar of water resources in California – west-facing watersheds in the Sierra Nevada (the focus region of this dissertation) drain snowmelt to the Central Valley, which produces over half of the nation's fruits, nuts, and vegetables. Snowpack, along with the precipitation systems that accumulate them, vary strongly from year to year. Low-snowpack years can exacerbate drought and negatively impact hydropower production (Bartos and Chester 2015), crop production (Pathak et al. 2018), and wildfire risk (Westerling et al. 2006). Large snowpacks can exacerbate flood risk (Kattelmann 1997a; Berghuijs et al. 2016). These benefits and hazards to natural and social systems make snowpack behaviors crucial to understand and forecast successfully.

Anthropogenic impacts on aerosol production resulting in enhanced radiative forcing and warming temperatures alters snowpacks' natural water tower function by reducing both the fraction of winter precipitation falling as snow (Dettinger et al. 2004a; Knowles et al. 2006; Feng and Hu 2007; Kunkel et al. 2009; McCabe et al. 2018) and its albedo, accelerating snowmelt (Skiles et al. 2018). As a result, peak snowpacks and streamflow volumes have decreased and shifted earlier in the year (Kapnick and Hall 2010, 2012; Stewart et al. 2005; Fritze et al. 2011; Westerling 2016; Dudley et al. 2017; Mote et al. 2018; Wasko et al. 2020). These trends are expected to persist in a warmer future as shown by statistical extrapolation (Bales et al. 2015; Howat and Tulaczyk 2005; Huning and AghaKouchak 2018) and model scenarios from global climate model projections (Maurer 2007; Pierce and Cayan 2013; Sun et al. 2016, 2019; Rhoades

et al. 2018; Huang et al. 2018; Fyfe et al. 2017). Moreover, the winter precipitation regimes that favor snowpack accumulation (e.g., atmospheric rivers, or ARs; (Serreze et al. 2001; Guan et al. 2010) are projected to intensify (Gershunov et al. 2019; Rhoades et al. 2020). Snowpacks may therefore shift from seasonal reservoirs to posing more social and environmental hazards, stressing current ecosystems and water resource management practices.

Successful adaptation and hazard and water resource preparation to these shifts is predicated on a first-principles understanding of the processes driving snowpack behaviors. However, most long-term observations and model projections are incapable of resolving process-level snowpack behaviors, leaving an incomplete toolkit for assessing and interpreting environmental threat levels in snow-fed watersheds.

1.2 Snowpack accumulation with regard to warming temperatures

In the Sierra Nevada, snowpack accumulates from a few orographically enhanced storms each year (Dettinger et al. 2004b; Huning and Margulis 2017; Lute and Abatzoglou 2014). Many of these are driven by ARs (Guan et al. 2010, 2013; Goldenson et al. 2018; Eldardiry et al. 2019). Snowpacks tend to accumulate les in warmer, lower-elevation regions, and more in colder, high-elevation regions (Mote 2006; Pierce et al. 2008; Zeng et al. 2018). Studies characterizing the controls on mountain range-scale snow accumulation often do so indirectly by considering the seasonal maximum snow water equivalent (SWE), or the 01 April SWE, in relation to cold season precipitation and temperature (Mote 2006; Huning and AghaKouchak 2018; Zeng et al. 2018). This approach focuses on the overall end-of-winter SWE and the preceding meteorological conditions. While shedding some light on conditions responsible for accumulated SWE, the accumulation process itself remains unresolved by such gross

characterizations. Conversely, research focused entirely on process-level snowpack evolution (Jennings et al. 2018) are limited to narrow spatial domains.

This tradeoff leaves a knowledge gap regarding snow accumulation drivers that few studies have addressed at spatiotemporal scales representing both storms and mountain ranges. In the Sierra Nevada's American River basin, Lundquist et al. (2008) quantified a strong (90%) likelihood of snow accumulation at temperatures below 0˚C that reduces to a near-equal likelihood of snow accumulation or melt at temperatures around 1.5˚C. Across the Sierra Nevada, Guan et al. (2010) found ARs to contribute up to 40% of snow accumulation, correlating strongly with below-0˚C temperatures. Seligman et al. (2014) quantified the snowpack energy deficits imparted by spring storm events in western Montana, noting the importance of snowfall over re-freeze events in delaying snowmelt. Hu & Nolin (2019) evaluated the frequency of snow accumulation days occurring at warmer minimum temperatures during AR conditions, vs. colder temperatures during storms not involving ARs, over the Western United States.

Non-linear warming-related shifts from snowfall to rainfall add to this gap regarding snow accumulation mechanics in mountain ranges. The rain-snow transition (along with rain-on-snow events, discussed in detail in Section 1.3) are expected to recede uphill (Klos et al. 2014). At the event-scale, the melting of falling snow is tempered by latent cooling from a humidity gradient (Harpold et al. 2017b), latent heat loss from melting, and adiabatic cooling from vertical motion (Minder et al. 2011). This demonstrates that the precip phase transition from snow to rain depends on atmospheric structure beyond temperature alone, as does the snowpack itself (Harpold and Brooks 2018). Few studies investigate the boundary governing whether SWE accumulates or ablates when temperatures are near or above the triple point (Lundquist et al.

2008; Guan et al. 2010). None consider jointly the role of atmospheric moisture in controlling mountain snowpack changes at a sub-daily timescale across an entire mountain range.

1.3 Snowpack responses to rain-on-snow

Mountain rain-on-snow (ROS) produces some of the largest and most damaging floods in the Western United States (Li et al. 2019; Tarouilly et al. 2021; Welty and Zeng 2021). In the Sierra Nevada, ROS flooding commonly occurs due to landfalling ARs, which contribute warm, humid, and windy conditions and prolonged precipitation with anomalously high snow levels over vast, typically snowfall-dominated landscapes (Corringham et al. 2019; Guan et al. 2016; Hatchett et al. 2017; Ingram 2013; Kattelmann 1997a). Climate warming will likely elevate flood risk throughout the 21st century, driven both by increasing precipitation extremes (Gershunov et al. 2019; Rhoades et al. 2020) and shifts in precipitation phase from snow to rain over a snow cover receding upslope (Musselman et al. 2018). These changes make ROS a transient but immediate flood hazard to forecast successfully. Accurate modeling and forecasting of ROS in turn depends on accurate physical interpretations of flood generation, both on a storm-by-storm basis and in the broader context of how the wet season shapes snowpack and watershed responses altogether. Improving societal ROS flood preparedness therefore requires two connected components of predictive understanding.

First, the degree to which snowmelt amplifies runoff during ROS is crucial yet highly-variable (Brandt et al. 2022). It is often quantified by comparing the snowmelt volume to the sum of rainfall and snowmelt, or terrestrial water input (TWI), and can range from 0% (Juras et al. 2017; Rücker et al. 2019) to 60% (Garvelmann et al. 2015) of TWI. Snowmelt is the product of the energy balance, and can only begin once energy inputs exceed the snowpack's heat capacity (i.e., its cold content) (DeWalle and Rango 2008). Once the cold content has been satisfied,

meteorological conditions can drive a positive energy balance through favorably high humidity, air temperatures, and wind speeds inducing snowmelt (DeWalle and Rango 2008). Case studies historically indicate turbulent and (longwave) radiative fluxes during extreme ROS dominate ROS induced snowmelt. Several examples of these "active" contributions to TWI range between 21-56% in the United States Pacific Northwest (Marks et al. 1998), 13-26% in the Swiss Alps (Rössler et al. 2014), 37% in the Sierra Nevada (Henn et al. 2020), and 2-60% in Black Forest, Germany (Garvelmann and Weiler 2014; Garvelmann et al. 2015). Other energy balance components can also be important, including the ground heat flux (Pomeroy et al. 2016) and the heat advection from rainfall (McGowan et al. 2021) – two typically neglected terms (DeWalle and Rango 2008). When studied in aggregate, however, net radiation dominates snowmelt, (Li et al. 2019; Mazurkiewicz et al. 2008), which tends to contribute no more than 30% to TWI (Trubilowicz and Moore 2017; Wayand et al. 2015; Würzer et al. 2016). Importantly, the degree to which snowmelt "actively" drives ROS flooding is also modified by basin properties (e.g., topography, tributary area, vegetation, and the preceding snow-covered area), storm characteristics (e.g., rainfall duration, intensity, and temperature), and antecedent snowpack conditions (e.g., cold content, liquid water content, and the presence of ice lenses or crusts) (Berris and Harr 1987; Garvelmann et al. 2015; Juras et al. 2017; Kattelmann 1997a,b; Marks et al. 1998; Rössler et al. 2014; Singh et al. 1997; Würzer et al. 2016). Finally, if cold content is not satisfied over large parts of a watershed, snowpacks can play a more "passive" role in ROS. In the Sierra Nevada, rainfall contributions to TWI can be as high as ~77-95% (Bergman 1983; Kattelmann 1997a).

The second component to predictive understanding of ROS involves how liquid travels through snow, which impacts both runoff timing and volume. Two flow regimes broadly

characterize this. First, rain and/or snowmelt may flow as a uniform wetting front (or "matrix flow"), propagating vertically and evenly through the snowpack. While matrix flow is observed in shallow, mature or melting snow (Hirashima et al. 2019; Webb et al. 2018b; Würzer et al. 2017), and is a key assumption of flow in most physically-based models to date (Andreadis et al. 2009; Bartelt and Lehning 2002; Colbeck 1975a; Jordan 1991), it is far from ubiquitous. Second, a preferential flow regime consists of pathways that instead collect and preferentially route liquid through the snowpack laterally – across melt-freeze crusts or capillary barriers – or vertically through "macropores" or "flow fingers" (Kattelmann 1985; Kattelmann and Dozier 1999; Marsh and Woo 1984). Rainfall (Singh et al. 1997) or a near-melting (i.e., low cold content) snowpack (Kattelmann and Dozier 1999; Wankiewicz 1978) can "prime" a snowpack to develop a high-conductivity flow-path network by "connecting the plumbing." Preferential flow enables the "passive" character of snow during ROS, quickly routing rainfall vertically or laterally into streams (Juras et al. 2017; Webb et al. 2021; Würzer et al. 2017), and advancing TWI timing from days to weeks (Kattelmann and Dozier 1999) – sometimes as fast as 6-7 m hr^{-1} (Eiriksson et al. 2013; Singh et al. 1997). On the other hand, crusts within a snowpack's stratigraphy can suspend liquid and delay snowpack outflow by hours (Conway and Benedict 1994; Kattelmann 1997b; Marsh and Woo 1984). The flow regime itself and its effect on runoff timing and volume is also modulated by the intensity of rainfall and preexisting snowpack liquid water content (LWC) (Brandt et al. 2022; Juras et al. 2017; Singh et al. 1997; Würzer et al. 2016).

Given these nuances, physically-grounded interpretations of ROS are crucial to classifying hazards to human and environmental systems. However, this is challenged by a lack of observations capable of detailing the above-mentioned mechanisms in space and time at scale. Matrix and preferential flow regimes co-exist and evolve (Hirashima et al. 2019; Webb et al.

2018b; Yamaguchi et al. 2018); and few locations host the instrumentation necessary to model the energy balance explicitly (Bair et al. 2018; Bales et al. 2006). Standard observations from long-standing networks (Schaefer and Johnson 1992; Serreze et al. 1999) (e.g., daily telemetered precipitation, temperature, and snow depth and/or water equivalent) may mischaracterize precipitation phase (Marks et al. 2013) and only provide a bulk snowpack representation. In turn, the use and validation of hydrologic models necessary for ROS flood forecasting in snow-dominated basins may leave important processes unresolved or misrepresented through calibration.

1.4 Research objectives and dissertation overview

Given the above-mentioned knowledge gaps and challenges this dissertation investigates process-level snowpack behaviors during warm storms in California's Sierra Nevada using sub-daily snow, soil, stream, and hydrometeorological measurements, and with supporting observations from atmospheric reanalyses and satellite remote sensing. The research objectives of this dissertation are as follows: (1) Assess the physiographic underpinnings of snow accumulation dependence on air temperature and storm characteristics; (2) delineate the governing snowpack conditions and underlying processes of snowpack response to storms with temperatures near the triple point; (3) identify the likely flood-driving mechanism(s) during ROS at the basin scale.

The remainder of this dissertation is divided into three chapters. Chapter 2 delineates an hourly relationship between air temperature, atmospheric moisture, and changes to SWE spanning the Sierra during water years 2010-2019. Chapter 3 focuses on a peculiar SWE "oscillation" in the Northern Sierra during rain-on-snow (ROS) events in January and February

2017. Chapter 4 elaborates on this case study to other ROS events in water years 2017-2019 to distinguish relatively benign from hazardous ROS.

Chapter 2 Factors governing winter snow accumulation and ablation susceptibility

Kayden Haleakala, Mekonnen Gebremichael, Jeff Dozier, and Dennis P. Lettenmaier

2.1 Data and methods

We obtained raw hourly snow pillow data for a set of stations operated by the California Department of Water Resources (DWR, available from the California Data Exchange Center at https://cdec.water.ca.gov/) that span an elevational and latitudinal transect along the Sierra Nevada (Figure 2.1a, 2.1b). After screening the data for spurious measurements (Appendix B), we used the processed hourly SWE and air temperature to construct distributions of SWE accumulation across temperatures during storms. We screened collocated hourly snow depth measurements, where and when available. We used atmospheric reanalysis data to diagnose synoptic storm characteristics.

2.1.1 Snow and surface meteorology data

DWR manages a network of 139 automated monitoring stations in the Sierra Nevada that measure hourly temperature and SWE. Most of these sites also measure hourly snow depth and precipitation. Temperature sensors are typically mounted on a pole or mast and their height can vary between 5 and 10 meters, depending on the maximum depth at a site. Snow pillows record the weight of snow, which is converted to SWE. Sites measuring snow depth include ultrasonic depth sensors that measure the travel time of an acoustic pulse reflected from the snow surface.

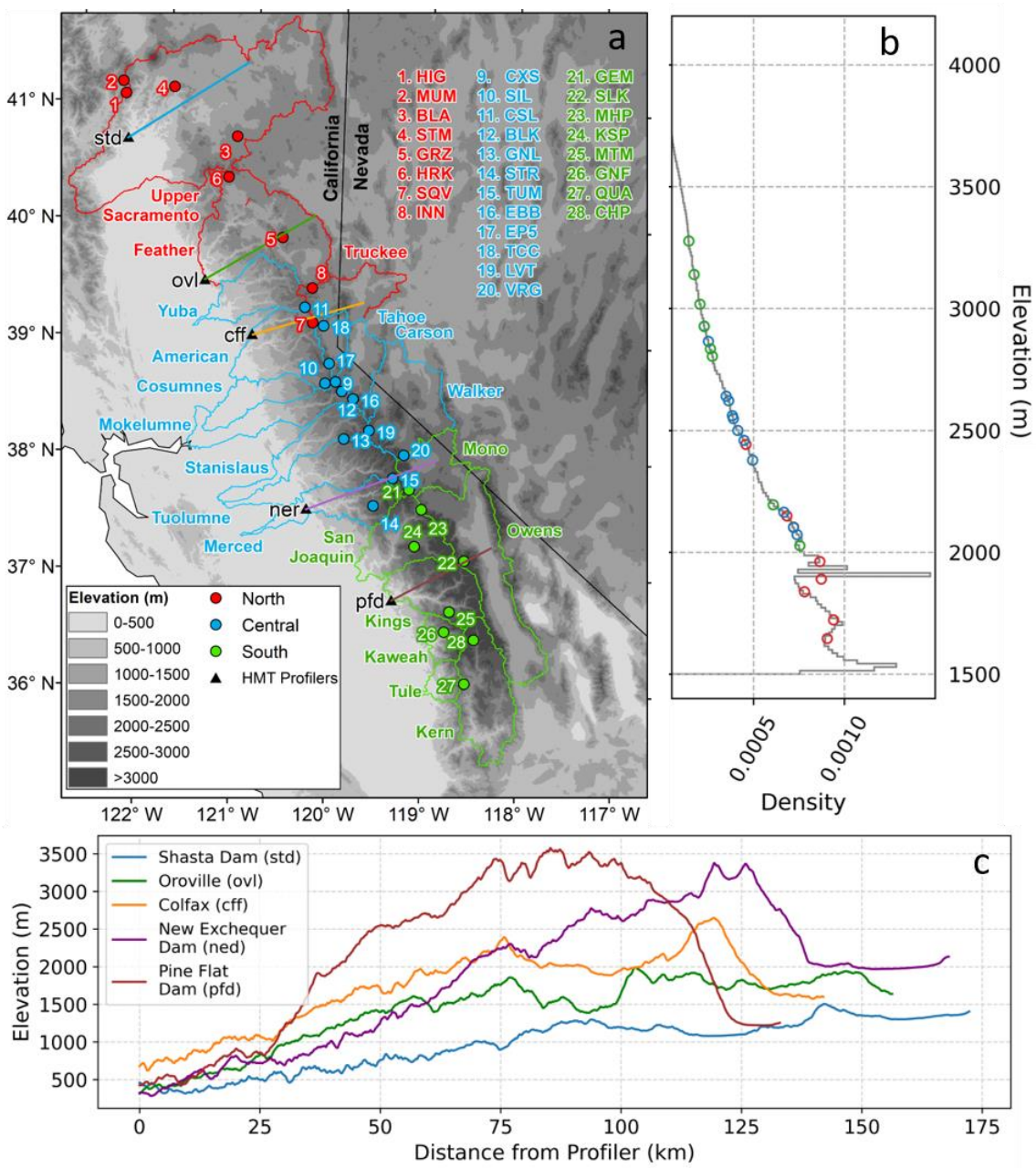

Figure 2.1 (a) Twenty-eight snow pillow sites used in this study. Snow pillows and watersheds are grouped into northern, central, and southern subregions. (b) Elevation distribution of land area above 1500 m encompassing the study sites. (c) Elevation profiles extending downwind from NOAA Hydrometeorology Testbed radar profilers shown in (a).

The exposure of the snow pillow sites varies, but sites are typically located in flat clearings surrounded by trees that shelter them from wind redistribution of snow. Relative to the

neighboring forest, however, snowfall at a pillow can be greater from lack of intercepted snowfall and local wind effects (e.g., reduced wind leeward of the forest resulting in enhanced snow deposition). Compared to the forests, the clearings experience more downwelling solar radiation (Marks and Dozier 1992), less downward longwave radiation, and greater wind speeds that enhance turbulent heat flux (Marks et al. 1998). Solar radiation differences are likely small given low sun elevations and shorter day lengths during most of the snow accumulation season, although longwave radiation during overcast contributes to snowmelt (Mazurkiewicz et al. 2008). Snow bridging can occur at snow pillows, causing recorded SWE to decrease or remain unchanged during storms until the bridge breaks, causing a spike in the pillow data. We have attempted to identify and flag such events (Appendix B). Depth sensors risk reporting false observations during storms from reflecting the signal of a falling hydrometeor rather than the static snow surface. Wind scouring or horizontal drift of fallen snow can also bias the recorded depth during the snow season. Furthermore, hourly snow pillow measurements can exhibit considerable noise due to battery voltage dependence on temperature (Appendix C; Figure C1, C2), which can result in large, erroneous fluctuations with diurnal temperature cycles. These artifacts risk noise being mistaken for a signal during snow accumulation or ablation periods (defined in Section 2.1.3), although this characteristic was primarily observed during stationary periods insignificant to our analyses and did not considerably impact our results.

Notwithstanding these sources of error, the DWR snow pillow network provides arguably the most comprehensive set of high-elevation measurements available at an hourly timescale in the Sierra Nevada. Figure 2.1a shows the locations of the 28 stations we used, most of which have hourly observations of temperature and SWE over the period water years (WY) 2010 through 2019. Several sites do not have snow depth measurements available, and several

individual site-years were screened from analysis after quality control (Appendix B). We selected these stations from the network of DWR snow pillows based on data availability, quality, and their representation of elevational and latitudinal gradients over the entire Sierra Nevada. We describe the selection process in detail in Appendix A. We disregarded some individual site-years due to missing or poor-quality temperature and/or SWE data (Table A1).

Snowpack telemetry sites cooperatively managed by the Natural Resources Conservation Service (NRCS) have demonstrated temperature sensor biases resulting in artificial warming trends (Oyler et al. 2015; Rangwala et al. 2015). While no related issues are reported for the DWR network (Lundquist & Huggett, 2008 compared DWR- and NRCS-deployed temperature sensors in the Tuolumne basin), we investigated temperature biases for the selected sites to be conservative, because they could compromise relationships derived as a function of air temperature. No inconsistencies were found for any site within the analyzed time period (Appendix D; Figures D1 and D2).

2.1.2 Synoptic-scale storm characteristics

Mountain precipitation gauges are handicapped during snowstorms by wind-driven undercatch (Meyer et al. 2012), timing issues during snow accumulation (Bair et al. 2018), and inability to capture spatial heterogeneity. Moreover, heating in tipping bucket gauges can enhance evaporation. While a quality control routine might avoid some of these issues, we deemed collocated gauges untrustworthy as a stand-alone measurement of hourly winter precipitation, which is better approximated by incremental SWE.

We therefore considered synoptic atmospheric (column) conditions during SWE accumulation or ablation events (defined in Section 2.1.3). We derived integrated vapor transport (IVT) from the ERA5 global reanalysis, chosen for its fine horizontal (31 km), vertical (37

pressure levels), and temporal (hourly) resolutions (Hersbach et al. 2020). IVT was taken over 27 pressure levels from the surface (Psfc) to 100 hPa. IVT magnitude (kg m^{-1} s^{-1}) is given by Lavers et al. (2012)

$$\text{IVT}=\sqrt{\left(\frac{1}{g}\int_{P_{sfc}}^{10{,}000\ Pa} qu dp\right)^2+\left(\frac{1}{g}\int_{P_{sfc}}^{10{,}000\ Pa} qv dp\right)^2}, \quad Eq\ (2.1)$$

where g is the gravitational acceleration (m s^{-2}), q is the specific humidity (kg kg^{-1}), u and v are zonal and meridional wind components (m s-*1*), and p is the pressure (Pa).

Nearest-grid values were assigned to each site to characterize overlying precipitable water and wind fields. ERA5 pressure levels were truncated at the surface air pressure at each site, which was calculated as a function of elevation using the barometric formula for a standard atmosphere following the moist adiabatic lapse rate (NASA et al. 1976). We screened for outliers in IVT (due to known wind field errors in early WY 2010) by filtering values outside of 150 percent of the inter-decile range.

From IVT we derive two additional measures of synoptic properties during SWE change events. The first uses ΔSWE, which we define as the back-looking difference in hourly SWE. The synoptic measure is the unitless ratio of ΔSWE to IVT, given by

$$R=\frac{\Delta SWE}{3600\left(IVT/\rho_d\ x\right)}, \quad Eq\ (2.2)$$

where ΔSWE and IVT are hourly values, x is the path length of IVT, which is the 31-km ERA5 grid size, and ρd is the density of dry air. Dry air density was calculated as a function of site elevation and temperature (NASA et al. 1976). The denominator in Eq. (1.2) effectively converts IVT from a horizontal moisture flux to the resulting moisture depth accumulated over the hour at a particular location. The value R compares roughly to the "drying ratio," defined by Smith et al. (2003) and Kirshbaum & Smith (2008) as the ratio of horizontally-integrated precipitation

(perpendicular to a mountain) to the IVT incident to the upwind foothills. Whereas *R* expresses moisture loss from orographic precipitation along its entire horizontal travel path, we define R here at a point to roughly express precipitation efficiency. We therefore consider this measure only during periods of SWE accumulation. It should be noted that modeled wind fields and grid cell average (31-km) elevations are often smoothed and muted in complex terrain, especially when representing a point observation. This smoothing may result in physically impossible values (i.e., *R* above 1), although no such case occurred in this study.

The second measure estimates the advected energy from this moisture flux and is considered both during periods of SWE accumulation and ablation. We define the term *A* (W m^{-2}) as

$$A = c_p \left(\frac{3600\, IVT}{x}\right) T, \quad Eq\ (2.3)$$

where c_p is the specific heat capacity of dry air and *T* is the site air temperature. This advection term corresponds to the energy imparted by the moisture flux integrated over the atmospheric column, and therefore takes on values much greater than those exchanged between the land surface and lower boundary layer.

2.1.3 Snowpack change events and corresponding distributions

We consider the distribution of SWE changes across a range of air temperatures during the accumulation season and the roles of storm characteristics in that relationship. We defined the accumulation season from the later of 1 November and the hour at which SWE first exceeded 2.5 cm, to the hour of peak SWE.

Within each season, we diagnosed SWE accumulation (ablation) events by considering days in which the 24-hour average SWE change is consecutively positive (negative) with absolute values above the 0.254-cm (0.1-inch) snow pillow resolution (Lundquist et al. 2015;

Serreze et al. 2001). SWE can oscillate at an hourly timescale, likely from wind redistribution, variations in overlying air mass (Brandt et al. 2020), or temperature-calibration issues with the snow pillow (Appendix C) that are not associated with storm conditions. We therefore use daily values to automate the detection of most SWE change events, as done in Serreze et al., (2001) which detected a total of 1,669 accumulation events and 544 ablation events. Other, short-duration (i.e., less than 3 days) or subtle, events (e.g., with longer, gradual SWE change) were detected manually, resulting in a total of 2,393 accumulation and 809 ablation events.

We computed hourly ΔSWE with the set of SWE change events. Increments were placed into 0.5˚C temperature bins centered at 0.0˚C, where a given temperature corresponded to the time step preceding a ΔSWE increment or decrement. For a batch of accumulation (or ablation) events, the net sum of ΔSWE values in each bin produced a distribution of net SWE accumulation (or ablation). We also constructed joint distributions by simultaneously binning ΔSWE increments into temperature and ΔSWE bins (at 0.254-cm widths) or IVT bins (at 25-kg m^{-1} s^{-1} widths).

We calculated net distributions for each site and calculated composite distributions by grouping sites into northern, central, and southern regions. The groupings were performed by watershed (Figure 2.1a), following DWR classifications for snow survey regions (https://cdec.water.ca.gov/snowapp/sweq.action). Figure 2.2a shows the average temperature during accumulation events for each site, demonstrating that this grouping also represents a decreasing storm-temperature gradient southward, which follows the general increasing elevation gradient of the Sierra Nevada. This grouping yielded 71, 112, and 82 site-years of SWE and temperature data in the north, central, and south regions, respectively (Table A1).

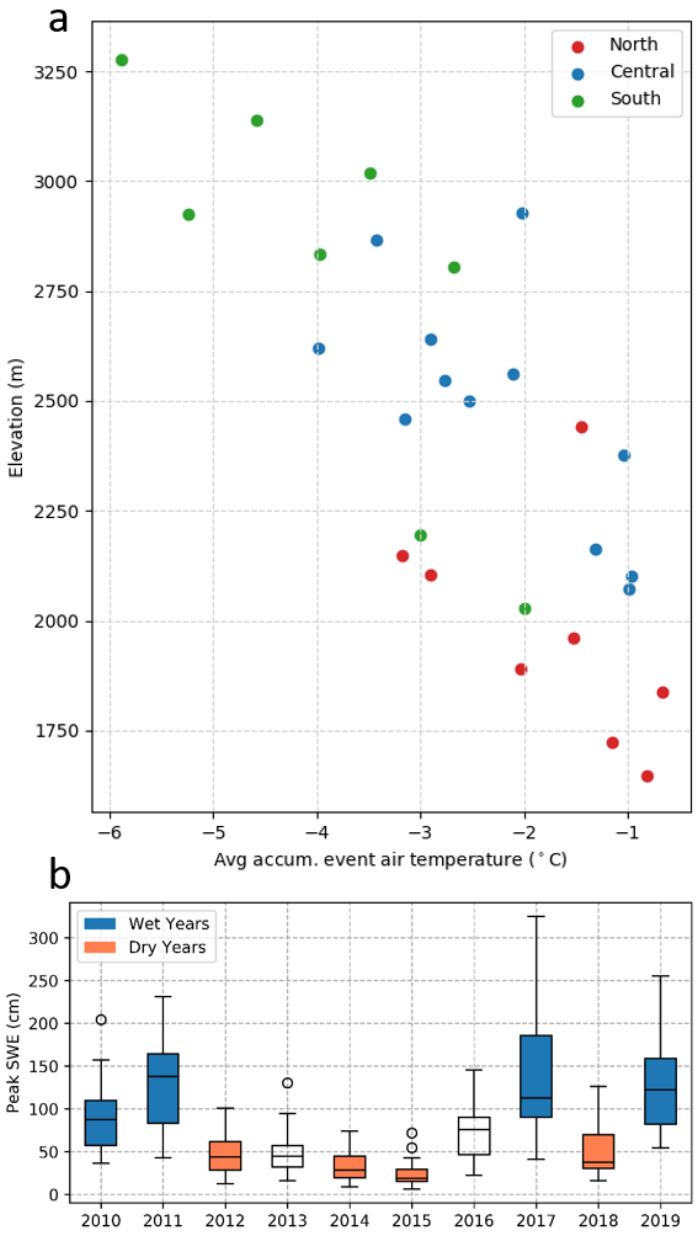

Figure 2.2 (a). Mean snow accumulation event air temperature for WY 2010 through 2019 plotted against snow pillow elevation. (b) Distribution of peak SWE across snow pillows for each season, demonstrating the assignment of wet and dry years.

We assessed the interannual variability of events by partitioning the WY 2010 through 2019 record into wet and dry years. We defined wet (dry) years by considering the 4 seasons having the highest (lowest) median peak SWE across all sites (Figure 2.2b). While this brief

record fails to sample the historical snowpack climatology, the selected wet and dry years are among the wettest and driest on record (Huning and Margulis 2017), thus appropriately bracketing interseasonal snowpack variability.

We detail the extent to which SWE accumulates or ablates under certain conditions by calculating the probability distribution of SWE accumulation and ablation conditioned on various snowpack and atmospheric characteristics. For a given variable X, we calculated the conditional likelihood of SWE accumulation,

$$Prob(\Delta SWE > 0 \mid X > x), \qquad x \in [min(X), Q_{98}(X)], \quad Eq\ (2.4)$$

where $Q_{98}(X)$ is the 98th quantile of X, for the sample of all SWE change events in each subregion and overall. Incrementing X across its range of observed values up to Q_{98} produces a distribution of conditional probabilities of a SWE change event accumulating SWE. To analyze antecedent event conditions, we considered conditional distributions across initial SWE, snow depth, bulk snow density, and the average 12-hour temperature preceding an event. For prevailing event conditions, we considered temperature, IVT, A, and event duration. We classify events by applying a threshold of 1.0˚C to the median air temperature during an event, above (below) which we consider "warm" ("cold"). We compared warm and cold events in each distribution.

2.2 Results

2.2.1 Topographic and synoptic characteristics

Temperature distributions of net SWE accumulation for individual sites (defined in Section 2.1.3) are shown in Figure 2.3, sorted by elevation (left) and region (right). Note the elevation distribution changes by region. The role of elevation in SWE accumulation temperatures manifests in a general cooling and broadening of distributions with altitude, where

interquartile ranges (IQRs) vary from -2.0 to 0.5˚C at 1722 m up to -8.0 to -1.5˚C at 3018 m and bound median temperatures of -0.5 and -4.5˚C, respectively. The decreasing temperature gradient is most pronounced at southern sites, which span the broadest elevation range (Figure 2.3, upper-right panel). All sites have median temperatures at or below 0.0˚C, but upper quartiles warm from 0.0˚C at southern sites, to 1.0-1.5˚C at central and northern (lower-elevation) sites.

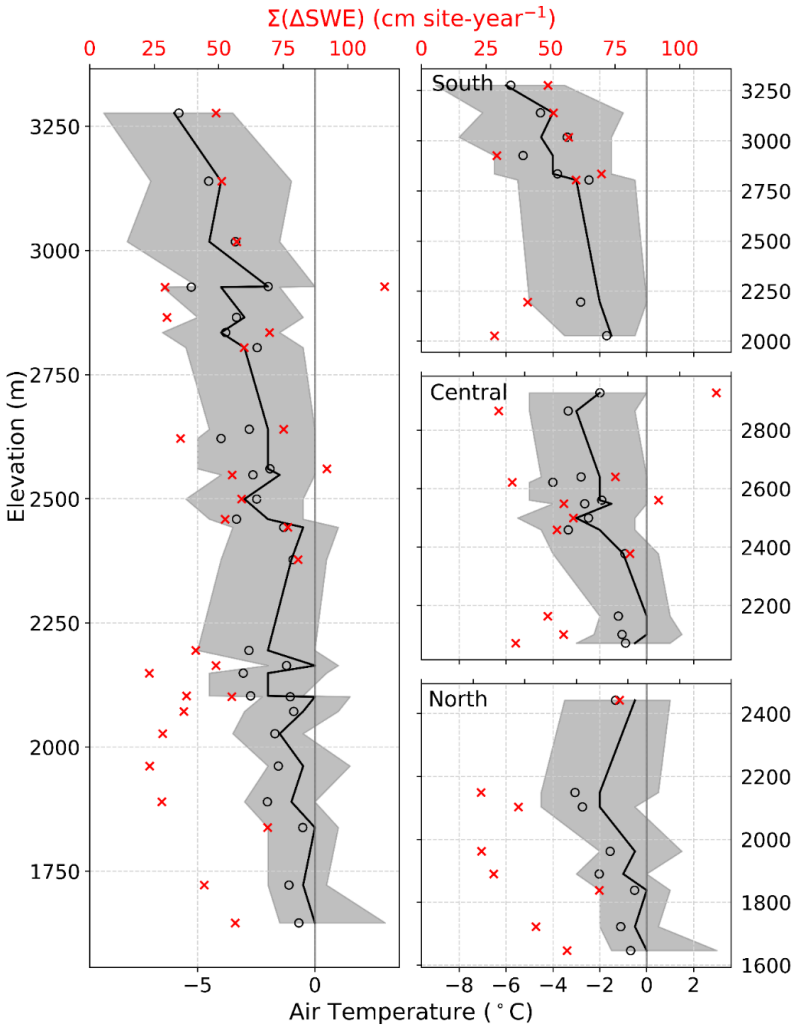

Figure 2.3 Elevation profiles of the temperature distribution of persistent SWE accumulation for (left) all sites and (right) those within each Sierra Nevada subregion. Grey shading indicates the interquartile range of 0.5˚C temperature bins between which half of the persistent SWE accumulates. The solid line indicates the distribution median. Open circles show the accumulation event average temperature, while red crosses indicate the seasonal average SWE accumulation (upper y-axis).

While temperature IQRs grow at higher sites, and while lower sites tend to accumulate the least SWE (e.g., 23 cm/site-year at 2149 m and 1962 m), total accumulated SWE depends less on altitude and more on orographic effects when temperature is no longer a limiting factor (Mote 2006), as accumulation is not necessarily greatest at the highest or coldest sites. For instance, two high-elevation sites (2927 m and 2926 m) have overlapping IQRs and considerably different seasonal SWE. Of the seven sites accumulating below the lower quartile of seasonal SWE (37 cm), four are relatively further east than neighboring sites, spanning all three subregions between 1962 and 2926 m. Seven sites accumulate above the upper quartile of seasonal SWE (62 cm), five of which are near the Sierra Nevada crest and span each subregion between 2010 and 2927 m. We discuss site variability further in Section 2.3.1.

The elevational and latitudinal transects of sites demonstrate a northward gradient of storm intensity. Joint distributions of temperature with hourly ΔSWE and IVT are shown for each subregion in the top and bottom rows of Figure 2.4, colored by the contribution of each bin to seasonal SWE accumulation. At southern sites, SWE accumulation covers a broad temperature range and modest ΔSWE values (1 percent of increments are above 0.95 cm hr^{-1}, top row of Figure 2.4). Central and northern SWE accumulations gradually display the opposite behavior, covering narrower temperature ranges and more intense ΔSWE (with 1 percent of increments above 1.11 cm hr^{-1}). However, this greater concentration of SWE accumulation is accompanied by ablation (negative ΔSWE) at similar magnitudes. While ablation reduces some seasonal SWE accumulation, it does not make a region unproductive, but rather reflects the efficiency at which SWE accumulates. For instance, integrating the distributions for all and positive-only ΔSWE shows the difference between net and gross SWE accumulation, respectively. Differences

increase from 8 percent at Southern sites up to 11 and 14 percent at northern and central sites, but they accumulate net amounts of 54, 58, and 70 cm per site-year, respectively.

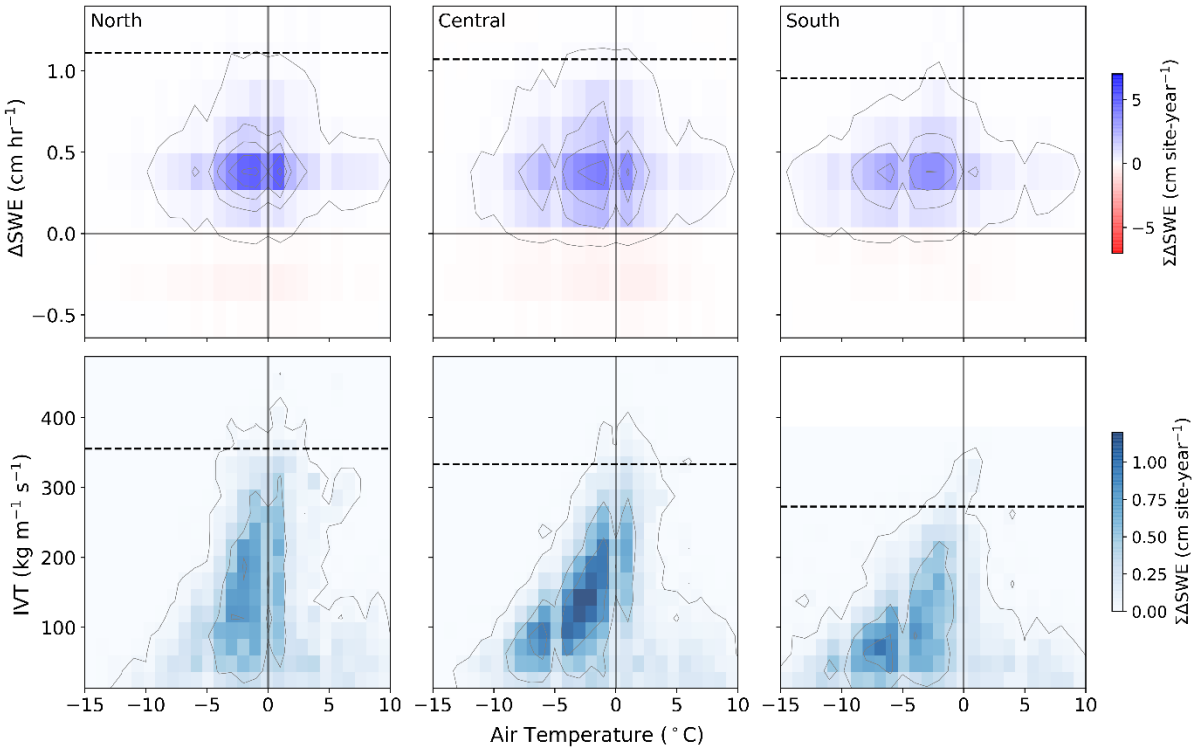

Figure 2.4 Joint distributions of air temperature (using 1˚C bins) with hourly ΔSWE (top, using 0.254-cm bins) and hourly IVT (bottom, using 25 kg m -1 s-1) for (left to right) north, central, and south regions. Distributions are colored and contoured by the average seasonal accumulated SWE during defined accumulation events. Contour lines are spaced by (top row) 12 and (bottom row) 4 mm per site-year intervals. Dashed lines indicate the 99th quantile of the marginal distributions across positive ΔSWE and IVT.

Regional differences in net SWE accumulation are in part explained by less available moisture at high elevations (bottom row of Figure 2.4). Temperature-IVT distributions demonstrate a gradual increase in IVT with temperature up to about 1.5˚C, but the IVT under which 99 percent of SWE accumulates decreases from 355 to 273 kg m-1 s-1 southward. At warmer temperatures, IVT magnitudes drop to below 225 kg m^{-1} s^{-1} during most hours of SWE accumulation. The greatest concentrations of SWE accumulation in temperature-IVT space

behave in modest accord with the Clausius-Clapeyron relation, which appears to impose an upper limit of SWE accumulation at a given temperature and is also apparent in temperature-integrated water vapor space (not shown). These windows demonstrate that SWE accumulation favors synoptic conditions able to balance snow formulation (requiring colder temperatures) while holding optimal moisture (at warmer temperatures).

2.2.2 Interannual variability

Figure 2.5 shows the marginal distributions of ΔSWE increments during accumulation events in wet and dry years for each region, demonstrating that SWE accumulates more efficiently (i.e., with relatively less negative ΔSWE) in wet-year storms than in dry-year storms. The ratio of the net total of all ΔSWE increments to the gross total of all positive ΔSWE increments ranges from 0.83 to 0.88 (0.87 to 0.93) in dry (wet) years. Northern sites demonstrate the greatest change in this ratio from dry to wet years (0.83 to 0.92), while southern sites' ratios remain high and change the least (0.88 to 0.93).

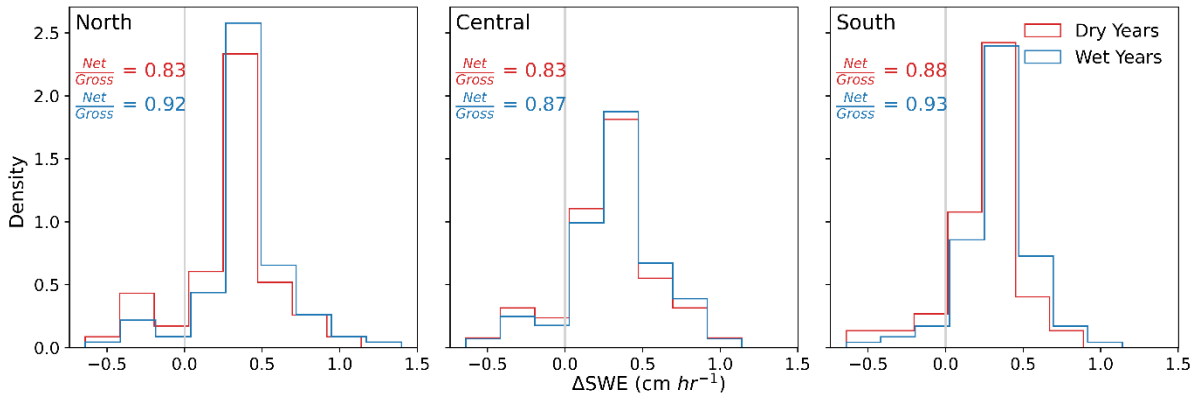

Figure 2.5 Histograms of ΔSWE increments (with 0.254-cm bins) during accumulation events in wet versus dry years for (left to right) north, central, and south regions. Net-to-Gross values indicate the ratio of the sum of all ΔSWE increments to the sum of all positive increments.

Figure 2.6a and 2.6b show that wet years have both more storms per season and more SWE accumulation per storm compared to dry years. Each bar shows the median and IQR for

each metric. The number of events per season varies similarly in wet and dry years with nearly identical IQRs, while the upper quartile of event SWE (Figure 2.6b) is considerably higher in wet years, demonstrating a heavier supply in leading SWE accumulation events. This follows from enhanced IVT (Figure 2.6e) and colder temperatures (Figure 2.6c). For all regions, wet and dry year differences in these metrics (and in the ΔSWE distributions in Figure 2.5) were deemed statistically significant (α=0.01) by an unpaired Mann-Whitney U test.

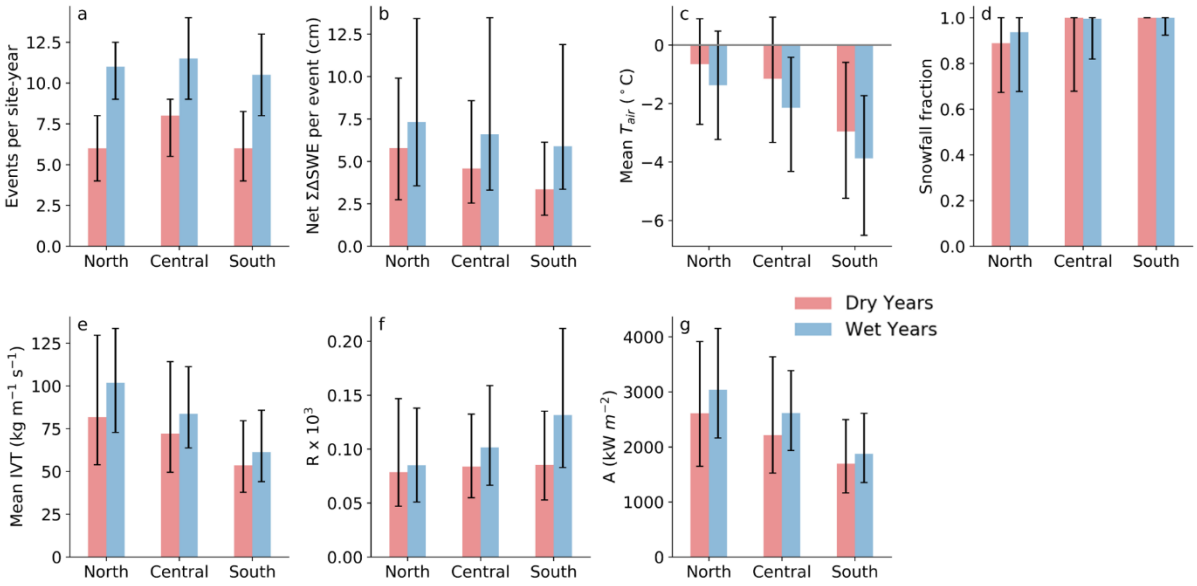

Figure 2.6 Medians (bars) and IQRs (error bars) of (a) SWE accumulation events per site-year, (b) net SWE accumulation per event, (c) average event air temperature, (d) event snowfall fraction, (e) average event IVT, (f) the ratio of gross SWE change to event total IVT, and (g) average event energy advection from the integrated moisture flux. Results are partitioned into (blue) wet years and (red) dry years.

While wet years are characterized by colder temperatures and greater SWE per storm, the likely form of precipitation shows no significant difference. We inferred precipitation phase from the upwind NOAA snow level radar (Johnston et al. 2017) nearest each snow pillow (Figure 2.1a), where a radar melting level height above the snow pillow elevation indicated possible rain, whereas lower melting levels indicated highly probable snow (we describe the radars and their

snow pillow assignments in Appendix E). The snowfall fraction, estimated by the proportion of time the radar melting level resided below site elevation, was persistently above 0.85 (Figure 6d). The lowest snowfall fractions were observed at northern sites, where storms most often go above melting temperatures.

Wet years also carry significantly ($\alpha = 0.05$) greater ΔSWE to IVT ratios (*R*, Figure 2.6f) and greater advected energy in the atmospheric column (*A*, Figure 2.6g) compared to dry years. Dry-year *R* values are similar across the range while increasing southward in wet years, corresponding to a southward gradient of decreasing SWE accumulation (Figure 2.6b) and IVT (Figure 2.6e) in dry-year storms. Values of *A* in both wet and dry years decrease southward (Figure 2.6g), following lower temperatures and IVT.

2.2.3 Snow accumulation versus midwinter ablation – antecedent conditions

The extent to which SWE increases or decreases during a storm is governed by antecedent snowpack and prevailing storm conditions. We detail these by considering the likelihood of an event resulting in SWE accumulation or ablation given certain preceding and prevailing snowpack and atmospheric measurements (Section 2.1.3). Controlling antecedent conditions are described in Figure 2.7, which shows the probability of SWE accumulation and ablation given measurements above certain values for the prior 12-hour average temperature and initial SWE, snow depth, and bulk snow density. These metrics are plotted for all sites and for each subregion. We distinguished warm (dashed lines) from cold (solid lines) events with a median temperature threshold of 1.0˚C during events.

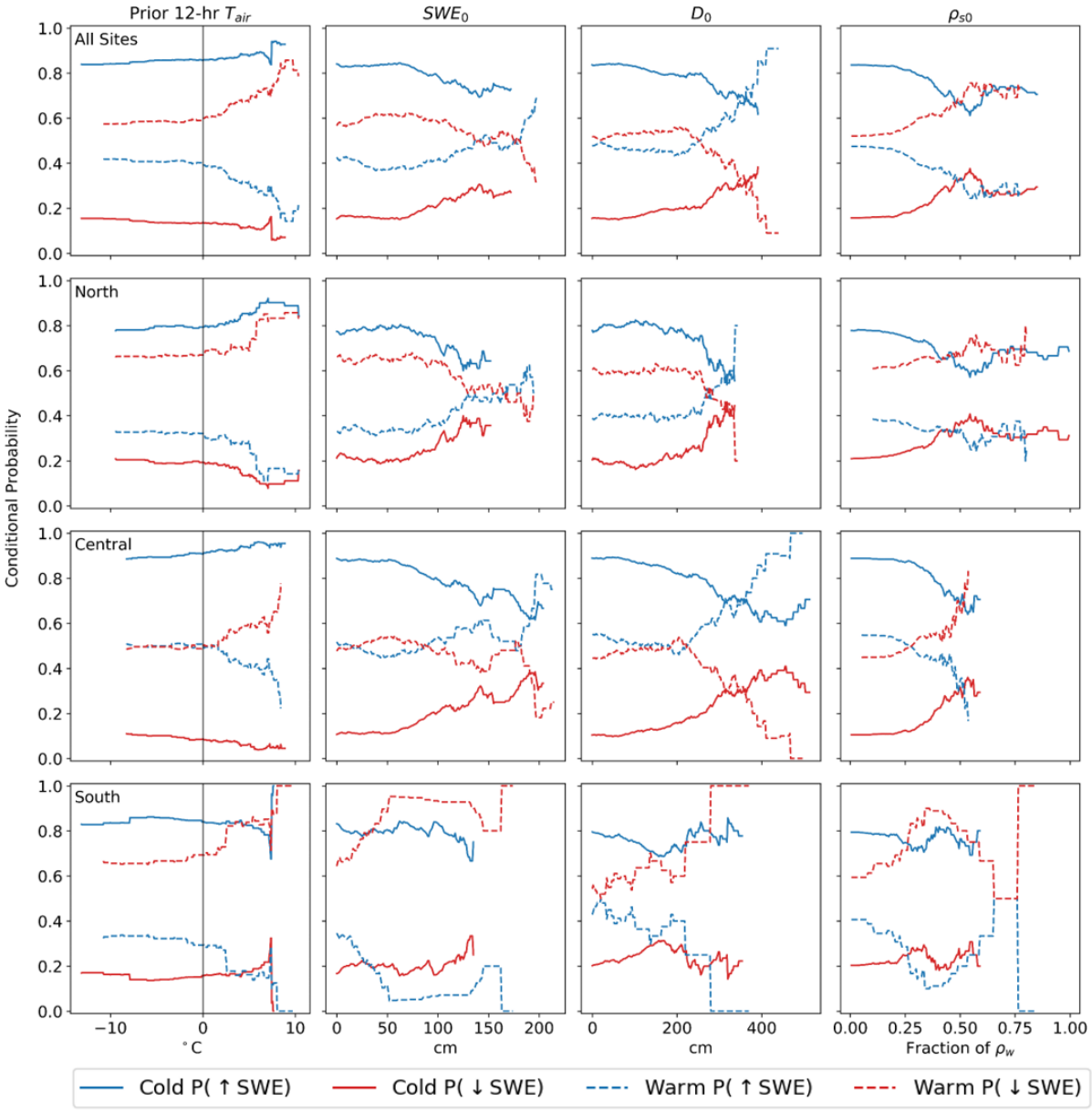

Figure 2.7 Antecedent event conditions governing SWE accumulation or ablation. Panels show the conditional probabilities of SWE accumulation (blue) and ablation (red) given values above (left to right) the 12-hour average air temperature before an event, initial SWE, initial D, and initial bulk snow density. The top row of subplots includes all sites; the lower three subset sites by north, central, and south subregions. Solid (dashed) lines indicate cold (warm) events, defined by a 1.0˚C event median temperature threshold.

Preceding temperature generally does not influence accumulation/ablation likelihood.

Cold accumulation events occur more frequently than ablation events irrespective of temperature

everywhere. The opposite occurs for warm events, in which ablation outnumbers accumulation, resulting in higher ablation likelihoods. However, warm events at central sites show a nearly equal likelihood of accumulation as ablation if the preceding 12 hours are below the melting temperature.

Initial snowpack states play more decisive roles in the fate of SWE during warm events. While cold accumulation events outnumber cold ablation events, warm events tend to result in accumulation when the snowpack is deep and ablation when it is shallow. This behavior predominates at northern and central sites. Overall accumulation likelihood surpasses ablation when depths exceed 250 cm. Snowpacks with densities below ~300 kg m^{-3} demonstrate the strongest accumulation likelihood in a warm event, although this does not exceed ablation likelihood except in the central Sierra Nevada. Ablation likelihood increases rapidly with denser snowpacks. The southern region demonstrates opposite behavior for initial snowpack conditions due in part to warm events being dominated by a relatively low-elevation site where warm ablation events outnumber warm accumulation events.

2.2.3 Snow accumulation versus midwinter ablation – prevailing event conditions

Figure 2.8 shows event conditions outlining the likelihoods of SWE accumulation and ablation for cold and warm event temperature, IVT, duration, and advected energy from moisture flux in the atmospheric column (Section 2.1.2). Median temperatures distinguished warm events, dominated by ablation, from cold events, which are dominated by accumulation. The likelihood of either tends toward the other when temperatures approach 0.0˚C.

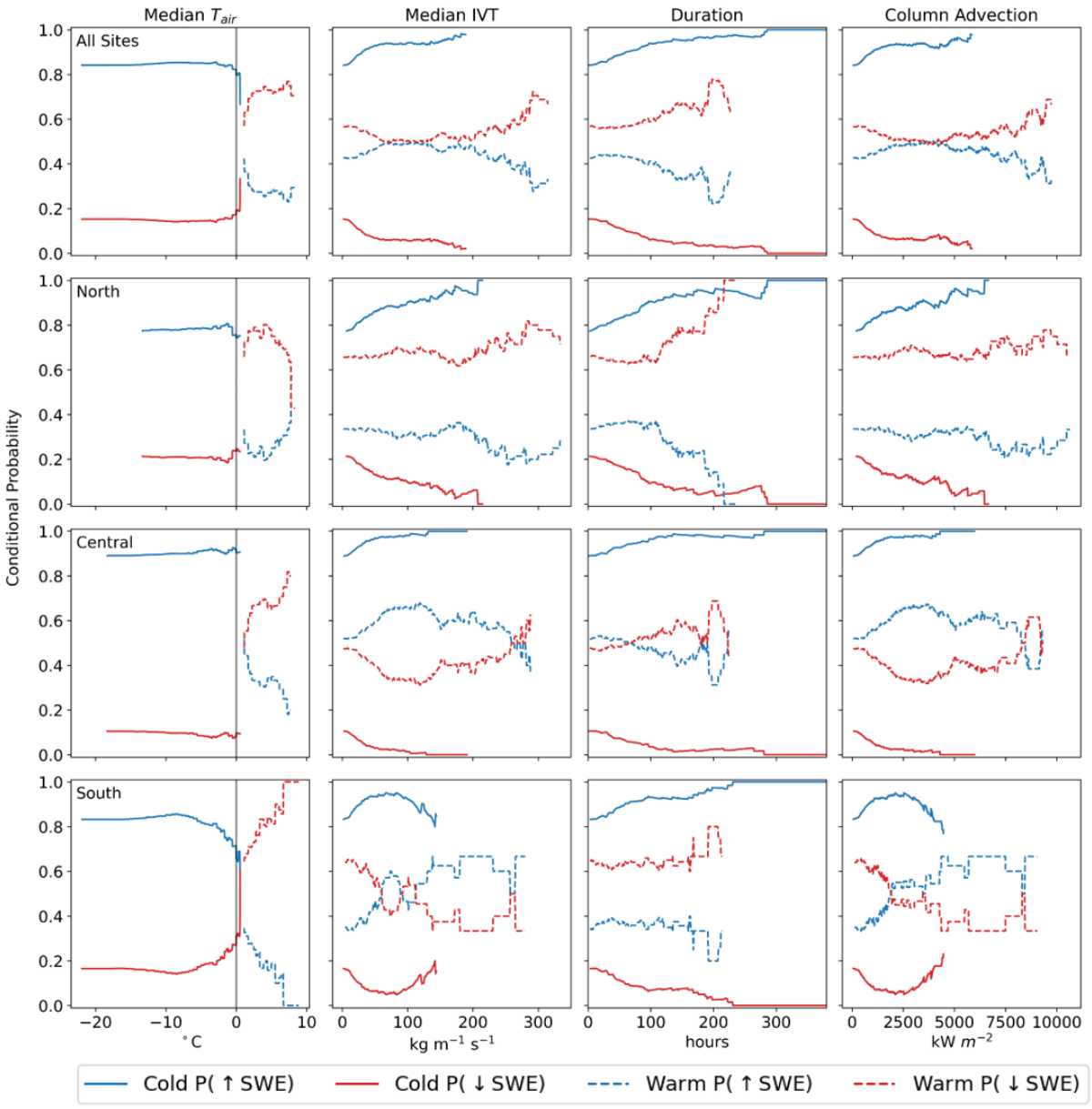

Figure 2.8 Same as Figure 2.7, but for prevailing event conditions (left to right) median event temperature, median event IVT, event duration, and the event energy advection from the integrated moisture flux. Solid (dashed) lines show relationships for cold (warm) events.

Across the range, the accumulation likelihood is unaffected by cold event IVT, duration, or advection. The same is true for warm events at northern sites, as consistently warmer temperatures at lower elevations predisposes the region to more ablation events irrespective of synoptic conditions. Central and southern sites demonstrate some sensitivity to IVT and

corresponding advection during warm events, as increased transports result in decreased accumulation in the central Sierra and increased accumulation in the southern Sierra. At central sites, high ablation likelihoods given large IVT is driven by atmospheric river events in WY 2017 and 2019 that melted snow at multiple sites. High ablation likelihood given low IVT at southern sites is attributed largely to one high-elevation site (CHP, 3139 m) demonstrating frequent SWE oscillations likely caused by wind redistribution.

Warm event durations weakly affect ablation likelihood (Figure 2.8), except for brief events at central sites, which demonstrate a greater accumulation likelihood for events lasting less than 5 days. Generally, warm SWE accumulation becomes more likely in short storms, although ablation is the most probable outcome.

2.3 Discussion

2.3.1 Orographic signatures and interannual variability in snow accumulation

We constructed distributions of hourly SWE changes across air temperature to assess its role in snow accumulation across the Sierra Nevada. We also investigated the joint influence of synoptic characteristics. Temperature distributions of net SWE accumulation cool and broaden with increasing elevation and decreasing latitude, indicating warmer, low-elevation SWE accumulation to be governed by temperature. Higher, colder sites are more limited by precipitation (Mote 2006; Scalzitti et al. 2016) and therefore governed by synoptic-scale circulation (Lundquist et al. 2010).

Seasonal SWE magnitude is thus tied strongly to orographic effects. Generally, the "wettest" sites occupy windward basins or are near the crest in leeward basins. "Dry" sites reside further east in the lee or at low elevations to the north. This relationship likely indicates a tendency for snow accumulation to be greatest on windward slopes of high-elevation ranges and

near the crest or on leeward slopes of low-elevation ranges (Barros and Lettenmaier 1994; Roe 2005), demonstrating favorable positions during southwesterly atmospheric rivers (Huning and Margulis 2018; Lundquist et al. 2015). Southern sites are relatively dry despite their high elevation, consistent with suggestions that higher, flatter terrain (Figure 2.1c) reduces orographic uplift and exhausts precipitable water (Kirchner et al. 2014; Huning and Margulis 2018). Exceptional SWE accumulation at sites far north (HIG) and downwind (GNL) may signify preferential deposition from south-southeasterly barrier jets (Huning and Margulis 2018; Lundquist et al. 2010, 2015) rather than atmospheric rivers (Brandt et al. 2020), although this suggestion would require more spatially explicit SWE change information.

We demarcate interannual variability in SWE accumulation with colder temperatures, higher storm frequency, and greater SWE and IVT per storm during wet years compared to dry years. Wet years carry more moisture in their leading storms (Figure 2.6e), resulting in a longer tail in event-accumulated SWE (Figure 2.6b). This is consistent with other work demonstrating wet-year atmospheric rivers bringing greater precipitation and SWE accumulation (Eldardiry et al. 2019) due to enhanced IVT (Huning and Margulis 2018). Huning & Margulis (2017) observed about 12-16 (7-11) snowstorms and more (fewer) storm-days during wet (dry) seasons, which agree with our results (where site sampling accounts for minor differences). We complement these prior research efforts by delineating SWE accumulation drivers at an hourly timescale that may be muffled by gross characterizations at longer timescales across a mountain transect.

2.3.2 Beneath the temperature dependence of snow accumulation

The control temperature imparts on SWE accumulation is strongly moderated by the moisture available to condense into solid precipitation. The joint distributions of net ΔSWE with

temperature and IVT with temperature (Figure 2.4) show that SWE accumulation favors conditions maximizing atmospheric moisture subject to the constraint of snow formation. In other words, the most productive SWE accumulation represents a tradeoff between moisture supply (limited by colder temperatures) and ice nucleation (limited by melting at 0˚C). Sufficiently cold conditions permit snow to form via vapor deposition and rimming of supercooled droplets, which shift to raindrop coalescence at the melting point. Colder temperatures are accompanied by enhanced condensation rates which promote efficient orographic precipitation relative to IVT (Albano et al. 2020; Kirshbaum and Smith 2008).

While southern sites are often cold and efficient in this manner (Figure 2.6f), this principle may limit their capacity to hold moisture, resulting in less seasonal SWE accumulation compared to the warmer, lower sites further north. Seasonal SWE accumulation differences are also emphasized by the fact that relatively fewer storms land in the southern Sierra Nevada (Bales et al. 2006). Northern and central sites accumulate SWE less efficiently, perhaps from evaporation of falling precipitation (Kirshbaum and Smith 2008) or experiencing both rain and snow during storms. Nonetheless, these less favorable conditions are outpaced by moisture supply when conditions are favorable during SWE accumulation events. Our results are consistent with Guan et al. (2010), who observed a similar tradeoff between snowfall fraction, temperature, and precipitable water, and with O'Hara et al. (2009), who found precipitable water and moisture stream orientation to be the leading drivers of heavy snowfall in the Sierra Nevada.

Results also show modest SWE accumulation above 0˚C, likely resulting from one (or a combination of) two mechanisms. The first is the tendency for latent cooling to attenuate the melting of snowfall. Increased hydrometeor mass may further reduce melting due to increased fall velocity and time required to melt (Minder et al. 2011). Warm SWE accumulation may

therefore result from mixed-phase precipitation avoiding melt before reaching the surface, which is likely the case in conditions still near 0˚C as the cooling effect lowers temperature as a result (Kain et al. 2000). The second mechanism (discussed in Section 2.3.3) is the refreezing of infiltrated rainfall within a snowpack, which is more likely at higher air temperatures.

2.3.3 Snow accumulation versus midwinter ablation

We calculated the likelihood of SWE accumulation or ablation conditioned on various snow and meteorological characteristics to delineate the factors governing snowpack response to warm storms. Across the Sierra Nevada at an hourly timescale, we reaffirm the capability of snow accumulating at temperatures above 0˚C (Lundquist et al. 2008; Guan et al. 2010). This is unsurprising given that most storms last longer than 24 hours and reflect diurnal behavior, meaning that events near but predominantly below 0°C would still reflect warm SWE accumulation. However, results also show nontrivial SWE accumulation likelihoods when the median event temperature is above 0˚C.

At northern and central (southern) sites, 16-17 (6) percent of SWE accumulation events were classified as warm (i.e., with a median temperature above 1.0˚C, Table 1), which coincided with deep, low-density snowpacks (indicating cold, unsaturated conditions) and brief, weak storm conditions. This is in agreement with Lundquist et al. (2008), who illustrated the importance of preexisting snow properties to the fate of precipitation. Shallower antecedent snow or intense, warm storms with strong IVT primarily resulted in ablation, shown by warm events having greater ablation likelihood for large advection rates accompanying IVT. This is likely more correlational than causal, as precipitation advection contributes little to snowmelt (Li et al. 2019; Marks and Dozier 1992). Conditions favoring ablation may instead point to unmeasured drivers, such as warmer temperatures indicating the role of enhanced longwave radiation in

cloudy conditions (Mazurkiewicz et al. 2008), or enhanced IVT indicating the role of strong winds driving turbulent exchange (Marks et al. 1998).

While we demonstrate that not all warm events result in ablation, they do not necessarily preserve seasonal snow storage despite appearing to do so at an hourly timescale. Between 22 and 39 percent of warm SWE accumulation events were immediately followed by midwinter ablation or seasonal snowmelt (Table 2.1), with southern (northern) sites demonstrating this behavior least (most) often. Results show that accumulation and ablation become equally likely around 0.6˚C, about 1 degree colder than reported by Lundquist et al. (2008) likely due to our data sample covering a higher elevation range (up to 3277 m) and temporal frequency (hourly). It should be noted that our observations do not evenly sample the Sierra Nevada hypsometry, as much of it occupies the 1500-2000-m elevation band (Figure 2.1b). This suggests that the likelihood of ablation following warm accumulation events may be greater than reported here, as relatively lower-elevation areas currently occupy more of the transient snow zone. Snow pillows were installed to support forecasts of seasonal runoff, so most are well above the transient snow zone.

Nonetheless, the tendency for some warm events to contribute to SWE accumulation without subsequent ablation indicates a positive surface energy balance competing (and losing) against the snowpack's developed cold content and liquid water retention (Jennings et al. 2018; Seligman et al. 2014). During rainfall in these cases, the latent heat released from refreezing after infiltration would not overcome the internal energy deficit of the snowpack, and the snowpack column itself would be deep and porous enough so as not to release more liquid than it captures.

Table 2.1 SWE accumulation and ablation event statistics by region and time period.

		# accumulation events (per site-year)	# warm accumulation events (per site-year)	Fraction of accumulation events that are warm	# (fraction) of warm accum events followed by ablation	# ablation events (per site-year)	# warm ablation events (per site-year)
South	Wet years	318 (11.4)	13 (0.5)	0.04	6 (0.46)	105 (3.4)	32 (1.1)
	Dry years	179 (6.4)	21 (0.8)	0.12	1 (0.05)	52 (1.9)	21 (0.8)
	All years	635 (8.9)	38 (0.5)	0.06	8 (0.22)	183 (2.6)	65 (0.9)
Central	Wet years	578 (12)	80 (1.7)	0.14	23 (0.31)	115 (2.4)	73 (1.5)
	Dry years	334 (7.8)	83 (1.9)	0.25	22 (0.27)	140 (3.3)	85 (2)
	All years	1,149 (10.3)	200 (1.8)	0.17	53 (0.25)	298 (2.7)	183 (1.6)
North	Wet years	341 (11)	47 (1.5)	0.14	20 (0.47)	143 (4.6)	92 (3)
	Dry years	175 (6.5)	35 (1.3)	0.20	12 (0.35)	140 (5.2)	71 (2.6)
	All years	609 (8.6)	95 (1.3)	0.16	36 (0.39)	328 (4.6)	182 (2.6)

This was likely the case more often at southern sites, which are higher and colder and accumulate SWE most efficiently, thereby developing and maintaining conservative energy deficits.

2.3.4 Climate warming implications

We delineate SWE accumulation controls and their relationship to air temperature at an hourly timescale here in an effort to understand the implications of climate warming on winter snowpack processes across the Sierra Nevada. Our results demonstrate available moisture to regulate the dependence of snow accumulation on temperature and that the higher, southern Sierra Nevada conservatively accumulates snowpack with colder, drier air and undergoes little midwinter ablation compared to lower sites further north. Taken together with future climate projections of enhanced IVT (Lavers et al. 2015), a sharpened distribution of more frequent and intense atmospheric river-related extreme precipitation (Gershunov et al. 2019; Huang et al. 2020), and decreasing (increasing) SWE at low (very high) elevations (Sun et al. 2019), our results suggest that snowpack accumulations at high elevations will come from a less conservative (i.e., less efficient) precipitation regime in a warmer climate. Consequently, as the transient snow zone recedes to higher elevations, snowpacks may diminish as a storage buffer against warm winter storms, making midwinter ablation more commonplace.

This implication assumes that low-elevation snowpack behavior serves as an analog for future high-elevation behavior. However, it is nuanced by the regional gradient of precipitation across the Sierra Nevada, which is wetter in the northern part of the range (Bales et al. 2006). Higher, southern sites therefore may not entirely adopt lower, northern behavior due to the potential for climate warming to affect midlatitude storm tracks. Poleward shifts in the Subtropical High (Choi et al. 2016) and in the travel of extratropical storms (Tamarin-Brodsky

and Kaspi 2017) could relax this gradient in the Sierra Nevada and exacerbate snow drought conditions by limiting the number of potential snow accumulation events. Competing mechanisms such as an extension of the Aleutian Low (Polade et al. 2017) and an eastward extension of the Pacific jet stream (Neelin et al. 2013) could bolster the regional gradient, making northern basins increasingly flood prone and southern snowpacks shaped by fewer favorable storms. Though, it should be noted that projected warming effects on the storm tracks and synoptic-scale dynamics germane to California precipitation may be within the envelope of natural climate variability (Zappa 2019; Maher et al. 2020) and are often climate model-dependent (Langenbrunner et al. 2015; Chang et al. 2015), making this a feebler perceived consequence of anthropogenic warming.

2.3.5 Instrumental and analytical limitations

Several inherent uncertainties and limitations accompany the use of point-scale snow pillow measurements to characterize snow accumulation across a mountain range. We used hourly measurements to assess behavioral SWE accumulation at a finer, process-resolving timescale than previously researched, which required a rigorous and partly manual quality control procedure. A risk in failing to screen erroneous measurements may still be present despite its reduction by supervision. SWE accumulation events having spuriously accepted voltage-based noise, for instance, may falsely inflate negative ΔSWE increments' contribution to accumulation efficiency (Figures 2.4 and 2.5).

Our supervised quality control approach constrained our analyses to a relatively small subset of sites (28) and brief period of record (up to 10 years), enough to provide insight about the conditions in which snow accumulates or ablates. This constriction is not ideal for developing a climatological characterization, as a few particular seasons or events may dominate

our results at some sites. While we refrain from per-basin analyses to limit exacerbating this issue, narrow sampling can still push results in an uncharacteristic direction (e.g., wet- versus dry-year analyses may not be entirely representative, as they use ~ 40 percent of an already constrained sample). Furthermore, point observations naturally fail to represent their surroundings, which may challenge our interpretations of antecedent SWE (Molotch and Bales 2005, 2006) and snow depth (Meromy et al. 2013). This representativeness issue also presents uncertainties pertaining to SWE change events, as the spatial distribution of precipitation is ignored by accumulation events defined at a single point. During snowmelt, research has shown that flow paths within a snowpack can divert meltwater and result in a downslope increase in SWE (Webb et al. 2018a). This implies that an accumulation event defined at a snow pillow may be a result of undetected snowmelt nearby, or from lateral flow paths in deeper, neighboring snow (Webb et al. 2018b).

We also used upwind snow level radars to infer the likely phase of precipitation (Figure 2.6d; Appendix E), notwithstanding the tendency for the atmospheric melting layer to bend toward windward mountain slopes during orographic precipitation (Medina et al. 2005; Minder et al. 2011) and result in offsets on the order of hundreds of meters below the free-air measurements upwind (Lundquist et al. 2008; Minder and Kingsmill 2013; Brandt et al. 2020). Although, our analysis is generally consistent with other research demonstrating a regional gradient in the snowfall fraction along the Sierra Nevada (Knowles et al. 2006; Safeeq et al. 2016).

2.4 Conclusions

Using 10 years of hourly snow pillow measurements, we characterize snow water equivalent (SWE) accumulation controls and their relationship to air temperature across an

elevational and latitudinal gradient along the California Sierra Nevada. SWE accumulation varies with orographic signatures and is shown to have a temperature dependence that is moderated by atmospheric moisture supply. We show that temperature conditions balancing precipitable water and snow formation requirements produce the most seasonal SWE, which was observed in the (low-) northern and (middle-elevation) central Sierra Nevada. The higher southern Sierra Nevada conservatively accumulates SWE with colder, drier air, and undergoes relatively less midwinter ablation as a result. These differences serve to explain a tendency for some deep, low-density snowpacks to accumulate rather than ablate during warm storms. This is most likely to occur for storm events that are modest in their duration and transported moisture or are immediately followed by ablation. Our results suggest that, in a warmer climate characterized by sharpened precipitation extremes and less snowfall, any accumulated snowpack may cease to store warm winter rain, increasing midwinter ablation responses. Snowpack liquid storage deficits and cold content lie at the core of our findings; this future implication could therefore support predictions of ablation susceptibility. Explicit measurements of these quantities at the requisite timescale (hourly) and spatial extent (range-wide) are unfortunately intensive. However, the probabilistic characterization of snowpack responses to warm storms we performed may provide an inroad to predicting snowpack responses at such an extent and timescale using related, more accessible quantities.

Chapter 3 Snowmelt during rain-on-snow was not a major contributor to the Oroville Dam flood of February 2017

Kayden Haleakala, W. Tyler Brandt, Benjamin J. Hatchett, Dennis P. Lettenmaier, and Mekonnen Gebremichael

3.1 Data and methods

This study aims to identify the likely flood-driving mechanism(s) during two large rain-on-snow (ROS) events in the northern Sierra Nevada in the winter of 2017. Sub-daily measurements in the Feather, Yuba, and American River basins (hereafter "study basins", Figure 3.1a) focus on (1) the two events themselves – one beginning on 7 January and the other on 6 February – and (2) the context of the "shoulder" seasons in explaining the roles of snowpack and basin conditions in ROS flooding.

3.1.1 In situ snow, soil, and meteorological measurements

Point measurements for snow water equivalent (SWE), soil moisture, air temperature, wind speed, relatively humidity, and precipitation were obtained at an hourly timescale (or sub-hourly, if available) from multiple networks in the Northern Sierra Nevada (Figure 3.1a). All data were converted to UTC and metric units.

3.1.1.1 Snow water equivalent

The California Department of Water Resources (DWR) manages a network of ~130 automated monitoring stations across the Sierra Nevada that measure SWE from snow pillows. In the northern Sierra Nevada, some of these stations are run by the Natural Resources Conservation Service (NRCS) as part of the SNOTEL network—but regardless all data are

posted to the DWR California Data Exchange Center (CDEC, http://cdec.water.ca.gov/snow/current/snow/index.html). We obtained hourly SWE from 22 snow pillows in the Feather, Yuba, and American River basins from CDEC. SWE values were quality-controlled manually. Metadata for snow pillows used in this study are provided in Table F1.

3.1.1.2 Soil moisture

Soil volumetric water content (VWC) is measured at few NRCS and DWR stations in our study basins (n=1). To raise the number of samples, we obtained VWC measurements from networks independent from CDEC and NRCS. These include the Western Regional Climate Center (WRCC, https://wrcc.dri.edu/), the National Oceanic and Atmospheric Administration Physical Sciences Laboratory (NOAA PSL, https://psl.noaa.gov/data/obs/datadisplay/), and the American River Hydrologic Observatory (ARHO; Bales et al. 2020). The ARHO is a distributed sensor network with each station comprising a cluster of sensor nodes. We report the cluster median for ARHO stations. VWC values from NOAA PSL were converted from raw reflectometry measurements using the standard coefficients in the corresponding data logger manual (Table 4 in https://psl.noaa.gov/data/obs/instruments/SoilWaterContent.pdf). Our expanded sample (n=6) occupies an elevation range from ~1,600 to ~2,700 m, and is described in (Table F2). The depth and timestep of data vary by station and network. We aggregated sub-hourly measurements to hourly timesteps.

VWC served two purposes in this study. First, we used the shallowest available sensors with collocated SWE to infer “passive” snowpack behavior as SWE increasing simultaneously with VWC during rainfall. The shallowest nodes (5-10 cm) were used to represent the snow-soil interface, and minimize the effect of differences in hydraulic conductivity across different soils. Second, we use the elevation gradient in soil moisture to show a widespread increase in

antecedent conditions resulting from winter storm events. No quality control was carried out for soil moisture measurements, as they were used qualitatively, did not display spurious behavior, and soil temperatures remained at or above 0˚C.

3.1.1.3 Surface meteorology

Measurements of precipitation, air temperature, relative humidity, and wind speed were obtained from CDEC, WRCC, and MesoWest. Similar to our VWC collection, we obtained data from WRCC and MesoWest for stations/variables that were absent from CDEC. The MesoWest portal (https://mesowest.utah.edu/), provided data from the National Weather Service and other Remove Automatic Weather Stations. We screened available measurements for each variable and applied quality control prior to analysis (described in detail in Appendix G). We used a total of 31 precipitation gauges to bound the range of precipitation during each storm over the study basins (Table F3). We used a total of 41 stations reporting temperature, humidity, and wind speed, though not all measurements were suitable for both storms of interest (Table F3; Appendix G). Temperatures and winds were summarized for each storm at 4 elevation bands.

3.1.2 Streamflow

Stream discharge measurements were obtained from the U.S. Geological Survey (USGS) National Water Information System (https://waterdata.usgs.gov/nwis). We used a total of 9 gages in this study (Table F4), but only four report measurements at a 15-minute timescale. These higher-frequency measurements were used in analyses with other sub-daily data. Daily measurements were used to illustrate how streamflow evolved over the winter season. Spatial boundaries for the upstream tributary areas were obtained from the Geospatial Attributes for Gages for Evaluating Streamflow (GAGES-II) data set (https://water.usgs.gov/lookup/getspatial?gagesII_Sept2011). Baseflow separation was done

using the sepBaseflow function in the Hydrograph-py Python library (https://hydrograph-py.readthedocs.io/en/latest/functions.html).

3.1.3 Snow level radars

Several Frequency Modulated-Continuous Wave snow level radars managed by NOAA PSL occupy the Central Valley and foothills of the Sierra Nevada. The brightband height (BBH) from these upward-looking S-band (2.8 to 3.0 GHz) radars estimate the melting level aloft, derived from an algorithm that inspects range gates for the maximum reflectivity and increasing Doppler fall velocity associated with melting snowfall (White et al. 2002; Appendix E). We used 10-minute BBH measurements from the Oroville and Colfax radars in this study (Table F5) as a measure of the likely phase of precipitation. We note that because these sensors are located in the Central Valley, they may not always truly reflect mountain based melting levels (Minder et al. 2011).

3.1.4 Remote sensing

True-color images from NASA Worldview (https://worldview.earthdata.nasa.gov/) were used for qualitative assessment of cloud and snow coverage. We obtained estimates of snow-covered area (SCA) from the Moderate Resolution Imaging Spectroradiometer (MODIS) Snow-Covered Area and Grain Size (MODSCAG) algorithm (Painter et al. 2009), which retrieves these properties daily at 500 m. Scenes over the study basins were used for near-cloudless (below 20%) days that had no apparent cloud coverage in Worldview. We then used SCA to calculate the regional snow line elevation over the aggregated study basins (Krajčí et al. 2014).

3.1.5 Atmospheric reanalysis

The 5th generation of atmospheric reanalysis from the European Centre for Medium-Range Weather Forecasts (ERA5) provides hourly atmospheric variables on a 0.25˚ grid

(Hersbach et al. 2020). We obtained ERA5 geopotential, air temperature, specific humidity, and zonal and meridional winds at 27 pressure levels (from 1,000 to 100 hPa) from the Copernicus Climate Change Service's Climate Data Store (https://cds.climate.copernicus.eu/). We also obtained hourly 0.1˚ surface wind and 0˚C altitude variables from ERA5-Land (Muñoz Sabater 2019) to test the argument of precipitation undercatch affecting the amount of snowmelt contributing to runoff during ROS (Appendix I).

3.1.6 Synoptic analysis

To assess synoptic differences between the January and February storm events over the study basins, we calculated the moist static energy (MSE) at each pressure level and the integrated vapor and heat transports (IVT, IHT). Equations are presented in Appendix H. In essence, IVT and IHT are wind-weighted quantities of moisture and heat, respectively, which are the key ingredients to turbulent fluxes (latent and sensible heat fluxes, respectively) at the surface, depending on the moisture and heat contents of the snowpack surface. We took the difference in MSE between 500 and 850 hPa as a relative measure of static instability (Dettinger et al. 2004b), where smaller gradients indicate less static stability and thereby a greater uplift tendency and conductance for turbulent fluxes. Taken together, these metrics lend some insight to the relative strength of atmospheric river-related melt drivers (Marks et al. 1998) between the January and February events. We also report supporting air temperature and wind speed comparisons from available surface stations (Table F3; see sub-section 3.1.1.3 "Surface Meteorology" above).

We report the surface air temperature, wind speed, IVT, IHT, and MSE gradient from each storm during hours when BBH (at either Oroville or Colfax) exceeded 1,600 m. These high-BBH hours were isolated in an effort to capture the prevailing conditions during rainfall over the

study basins. The 1,600 m threshold was selected to nominally represent the lower regions of the snow pillow network (Table F1) to suggest that rainfall is likely occurring over low-lying snow cover, at the very least. Given that this value resided on average a few hundred meters above the regional snow line elevation, this threshold inherently accounts for the regional lowering of upwind melting levels (Minder et al. 2011) that can positively bias BBH values applied downwind for precipitation phase partitioning. Both IVT and IHT were expressed as accumulations (kg m^{-1} and J m^{-1}) over the high-BBH timesteps. Values for the MSE gradients were averaged over high-BBH timesteps.

3.1.7 Cumulative discharge and rainfall comparisons

To assess both runoff efficiency and the notion of snowmelt augmenting TWI above rainfall alone, we compared rainfall estimates to observed discharge at each subdaily USGS gage over 4 intervals in the snow season. We hypothesized that runoff efficiency would grow over the course of the winter as liquid inputs accumulated to raise antecedent soil moisture, and that the presence of snowmelt and rainfall together would bring discharge above rainfall totals.

We partitioned gridded (4-km), 6-hourly precipitation from the California Nevada River Forecast Center (CNRFC, https://www.cnrfc.noaa.gov/arc_search.php) over the drainage areas of each subdaily USGS gage using BBHs from the nearest snow level radar. We first aggregated the 10-minute BBHs to hourly values. We filled the remaining gaps in the hourly time series using ordinary least squares regression of hourly BBH against the 0˚C altitude from the nearest ERA5-Land pixel from November 2016 through early May 2017. Regression results at the Oroville (n=664) and Colfax radar (n=671) yielded R^2 values of 0.93 and 0.95, respectively, with a standard error of 0.01 m. This gap-filled time series was then aggregated to 6-hourly values to match CNRFC, then lowered by 200, 400, and 600 m to test different degrees of snow level

bending (Minder et al. 2011). Using this to partition rainfall from CNRFC precipitation, we compared these accumulated rainfall estimates and accumulated observed discharge separately for the following periods: (1) the early winter season, from 15 November (the first large rainfall event) through December (2) January, encompassing the first storm of interest, (3) February, encompassing the second storm, and (4) early spring, from 16 March (the first rainfall event) through early May. These time frames were chosen such that rainfall began early in the period and ceased before the end of the period, but allowing several days of concentration time before the next rainfall event.

3.2 Results and discussion

3.2.1 Winter 2017 and its rain-on-snow events

Beginning in 2011, the Sierra Nevada experienced one of the most severe (Hatchett et al. 2015) droughts in recorded history prior to water year (WY) 2017 — a record precipitation year that broke the meteorological drought. The northern Sierra Nevada accumulated over 2,200 mm of precipitation from 49 landfalling ARs between 1 October and 12 April (Vano et al. 2019). A water resource tradeoff ensued – some major reservoirs filled to quell the hydrological drought (Boxall 2017), while others flooded (Sterle et al. 2019; White et al. 2019). In January and February 2017, eight "families" of ARs made landfall in Northern California (Fish et al. 2019), bringing several distinct, prolonged spells of precipitation (Sterle et al. 2019; White et al. 2019) (Figure 3.1b). Two storm sequences in particular – one from 7-12 January (hereafter 7J) and the other from 6-12 February (Michaelis et al. 2022) (6F) – were accompanied by high snow levels (Figure 3.1b) and prominent peaks in river discharge (Figure 3.1c).

The 7J sequence accumulated 329 mm of precipitation (median across precipitation gauges in the three study basins), and 224 mm of coincident discharge (median across stream

gauges; Fig. 3.1d). Snow levels (and discharge) rose rapidly beginning 7 Jan 0730Z, peaking at 3,059 m (above the highest point in all three basins) at 8 Jan 1350Z, then fell. A colder pulse of precipitation brought snow levels up to 2,364 m (above 98% of the study area) on 11 Jan 0420Z before declining, accompanied by a secondary peak in streamflow. Baseflow at the 4 sub-daily stream gauges (Table F4) rose between 170-210% (Figure 3.1c shows the Northern Yuba River gauge, USGS station 11413000). The event was followed by a relatively cold and modest storm from 13-23 Jan, which brought 103 mm of median precipitation, with snow levels averaging 1,319 m (above 35% of the study area). This colder, smaller storm minimally impacted streamflow, but effectively lowered the regional snowline to 960 m (Figure 3.1c, 3.3e).

The 6F event began with a rapid rise in snow levels from 1,915 to 3,169 m between 7 Feb 0200Z-1400Z (Figure 3.1b), lowering gradually. Three waves of precipitation occurred in succession, each with snow levels persistently above 1,500 m and distinctive streamflow signatures (Figure 3.1b, 3.1c). In total, the 6F event accumulated 322 mm of median precipitation and 241 mm of median coincident discharge. Importantly, the stream responses (and concurrent soil moisture signatures; Figure 3.6b-g) for both the 7J and 6F sequences, taken together with snow levels above the regional snow line, suggest that ROS was prevalent.

Both ROS events have similar synoptic characteristics during rainfall (Table 3.1, Figure 3.2). We assessed these during periods when snow levels exceeded 1,600 m. 7J and 6F total integrated vapor and heat transport, and average moist static energy gradients between 500- and 850-hPa are within ±4% of each other (Table 3.1).

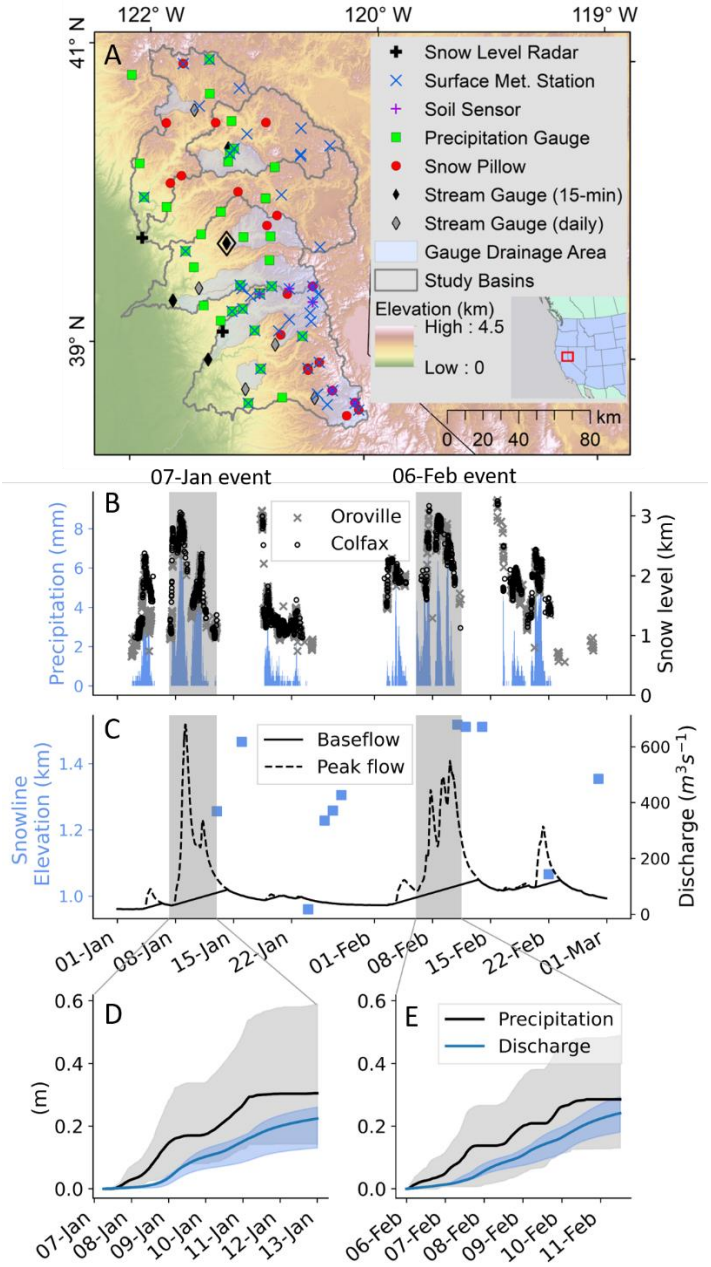

Figure 3.1 (A) Snow, river, and hydrometeorological monitoring stations in the Feather (North Fork, East Branch of North Fork, and Middle Fork), Yuba, and American River basins. Shaded areas drain to each USGS gage, which report either daily or 15-minute measurements. (B) Median hourly incremental rainfall from the gauge network in (A), and 10-minute brightband height from snow level radars in January through February 2017. The 7 January and 6 February storm sequences are shaded in grey. (C) Daily regional snow line elevation (calculated using MODIS fractional snow-covered area), and 15-minute stream discharge at USGS gauge 11413000 (North Yuba River Below Goodyears Bar; outlined in A), with baseflow separated. Cumulative discharge and precipitation medians and ranges are shown for the (D) 7J and (E) 6F storm events.

Table 3.1 Comparisons of synoptic and surface conditions over the study basins during the 7 January and 6 February storms when snow levels resided above 1,600 m.

Synoptic Metrics	**7 Jan AR**	**6 Feb AR**	**Δ% (Feb – Jan)**
High-BBH hours	58	62	+ 6.90%
Total Integrated Vapor Transport (10^6 kg m^{-1})	82.59	85.03	+ 2.95%
Total Integrated Heat Transport (10^{12} J m^{-1})	14,721	14,126	– 4.04%
Mean Moist Static Energy Gradient (kJ kg^{-1})	51.74	50.02	– 3.31%
Station Metrics	**7 Jan AR**	**6 Feb AR**	**Δ (Feb – Jan)**
Median Air Temperature (˚C)			
Z < 1,200 m	6.23 (n=8)	8.89 (n=8)	+ 2.66
1,200 m < Z < 1,600 m	3.89 (n=8)	5.56 (n=12)	+ 1.67
1,600 m < Z < 2,000 m	1.67 (n=10)	3.46 (n=11)	+ 1.79
Z > 2,000 m	– 0.35 (n=10)	1.13 (n=9)	+ 1.48
Median Wind Speed (m s^{-1})			
Z < 1,200 m	3.13 (n=6)	2.24 (n=6)	– 0.89
1,200 m < Z < 1,600 m	4.47 (n=6)	3.13 (n=9)	– 1.34
1,600 m < Z < 2,000 m	3.58 (n=4)	2.23 (n=7)	– 1.34
Z > 2,000 m	4.92 (n=2)	4.02 (n=1)	– 0.90

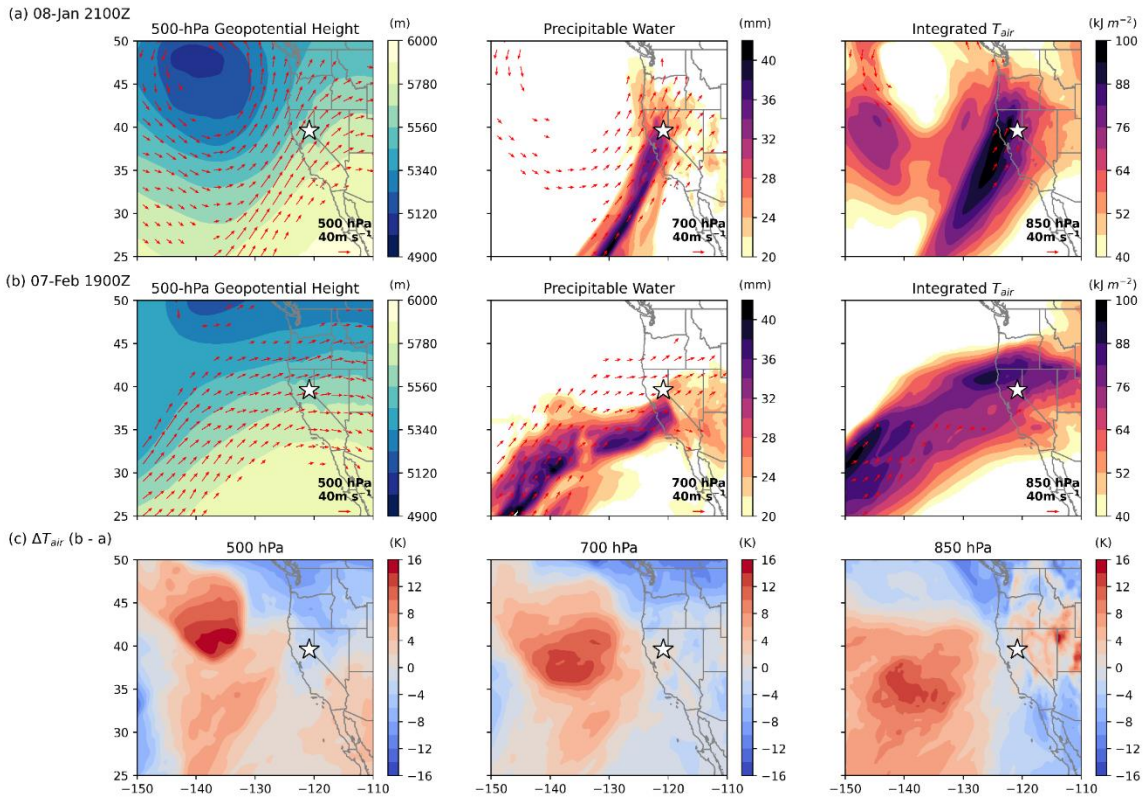

Figure 3.2 ERA5 500-hPa geopotential height, and column-integrated water vapor and heat at mid-storm timesteps in the (top row) January and (middle row) February storm events. Timesteps resemble moments in each storm when rain-on-snow elicited snow pillow responses. Wind vectors above 20 m s-1 are shown at 500, 700, and 850 hPa, which demonstrate stronger winds during the January event. In-storm air temperature differences at these pressure levels (bottom row) showcase the oncoming cold front at the end of the January event.

This suggests the atmospheric conditions in each ROS event sustained similar degrees of heat and moisture advection and static stability (Dettinger et al. 2004b) over the study basins. Surface stations indicate the 6F event, however, was generally warmer, particularly below 1,200 m, while the 7J event was relatively more wind-driven (Table 3.1; corroborated by reanalysis-derived wind fields in Figure 3.2). One notable difference was cold frontal passage during 7J that yielded a ~1,250 m decline in snow levels (Figure 3.2c, 3.1b). Conceivably, given a greater runoff-to-precipitation ratio and a slower decline in snow levels in the 6F event (Figure 3.1b,

3.1d, 3.1e), snowmelt may have augmented the 6F hydrograph which preceded the spillway incident at Lake Oroville (Henn et al. 2020; White et al. 2019).

3.2.2 Snow can be a passive conduit for rainfall

A previous case study of the 6F event noted that while precipitation ranked 9th-highest on record in the Feather River basin, runoff ranked 2nd (Henn et al. 2020), and reasoned that this extreme discharge was only possible with supplemental snowmelt. They estimated that snowmelt augmented TWI by approximately 37% relative to rainfall alone, which was supported by observations of daily snow water equivalent (SWE) decreases at snow pillows, an upslope migrating snow cover, and changes in a spatially-distributed SWE estimate between 24 January and 12 February (Henn et al. 2020). While high runoff ratios (Fig. 3.1d, 3.1e) and warm (above 0˚C) temperatures (Table 3.1) indeed suggest snowmelt amplified TWI, we provide two lines of evidence suggesting a different interpretation of the snowpack's role in these two events.

The first line of evidence considers ephemeral snow ablation unrelated to the 6F storm. SWE estimates derived from cloud-free satellite images of fractional snow-covered area (SCA) on 24 Jan and 12 Feb – bracketing the event – were used previously to calculate ROS snowmelt (Henn et al. 2020). We believe this was a reasonable approach, given cloud cover and/or large zenith angles (Dozier et al. 2008) on days closer to the event. However, a visual inspection of all available images reveals a substantial snowline withdrawal between 24 Jan and the 6F storm (Figure 3.3e-g). Neither soil moisture nor streamflow across study basins increased in response to this snow loss (Figure 3.6, 3.1c), which implies this ephemeral snowmelt volume and its contribution (McGuire et al. 2006) to antecedent conditions to the 6F flood event was small, or instead sublimation. The extensive SCA on 24 Jan therefore may have inflated snowmelt

contributions to the 6F ROS event (Henn et al. 2020), the size of which would depend on the difference between the true and SCA-derived SWE volumes in the watershed that day.

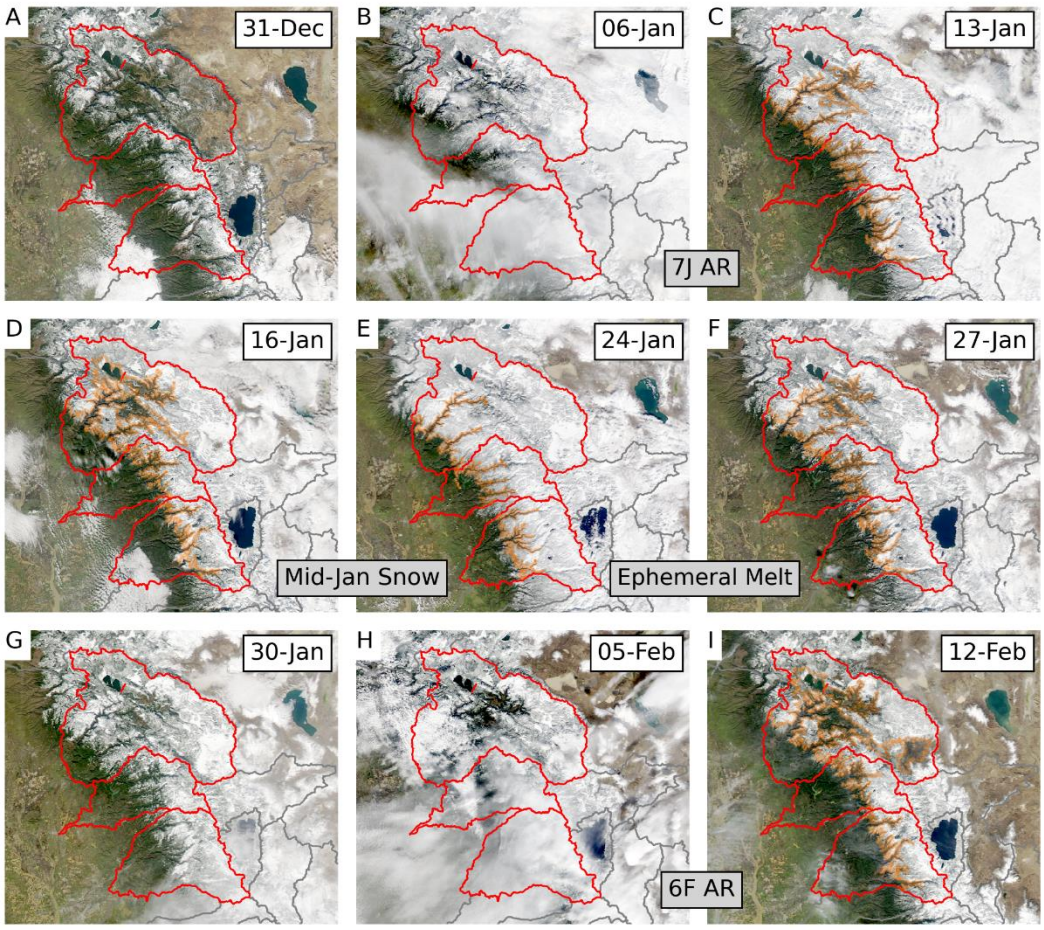

Figure 3.3 True-color evolution of the snow cover spans several noteworthy events in January and February 2017. Images bracket both ARs, the smaller storms directly preceding them, and the snowfall and snow withdrawal between AR events. Orange contours in (C), (D-F), and (I) show the regional snow line elevation over study basins as in Fig. 3.1C.

The second line of evidence involves subdaily variations in SWE during ROS that are commonly masked at a daily timestep or sometimes misclassified as measurement errors. "Standard" daily measurements (including temperature, snow depth, SWE, and precipitation) have been used previously to identify and interpret ROS events (McCabe et al. 2007; Wayand et al. 2015; Musselman et al. 2018; López-Moreno et al. 2021). While this avoids the instrument

error- and noise-related problems with subdaily measurements, daily timesteps mask or misrepresent the mechanism(s) generating runoff during ROS. For instance, the 6F event showed widespread declines in daily SWE from 7 Feb (Figure 3 in Henn et al. 2020). This measurement corresponds roughly to 1200Z that day, since daily values are obtained from a single hourly value around 0300-0400 local time (https://www.cnrfc.noaa.gov/awipsProducts/RNOFSTSWE.php; DWR, personal communication). However, heavy precipitation began as early as 6 Feb 0200Z, and snow levels began rising above the snow pillows 24 hours later (Figure 3.4b). This suggests that many of the snow pillows within the basin were likely experiencing rainfall. As a result, the "pulses" observed in the hourly SWE likely indicate rainfall saturating the snowpack (between 1300-2100Z) and then draining — rather than snowmelt. Similar SWE behavior occurred in the Yuba and American River basins in the 6F event (Figure 3.4e) and in the 7J event (Figure 3.4a, 3.4d).

This type of SWE pattern (rising-then-falling) has also been observed at an hourly timescale across the Sierra Nevada during warm storms (Haleakala et al. 2021), reported as ablation immediately following SWE accumulation events. However, shallow (10 cm or less) collocated soil moisture, where available, further supports the notion that "pulses" in SWE are due to liquid water movement through snow rather than ablation (insets in Figure 3.4c, 3.4f). Near-surface soil moisture co-varies with SWE oscillations, rather than inversely following the SWE loss during snowmelt (Harpold 2016). These behaviors strongly suggest a "passive" ROS response in which SWE pulses reflect transient rainfall storage then passage through snow. This runs contrary to conclusions drawn from daily observations that can misinterpret the SWE drainage post-saturation as snowmelt (Henn et al. 2020), potentially overestimating TWI.

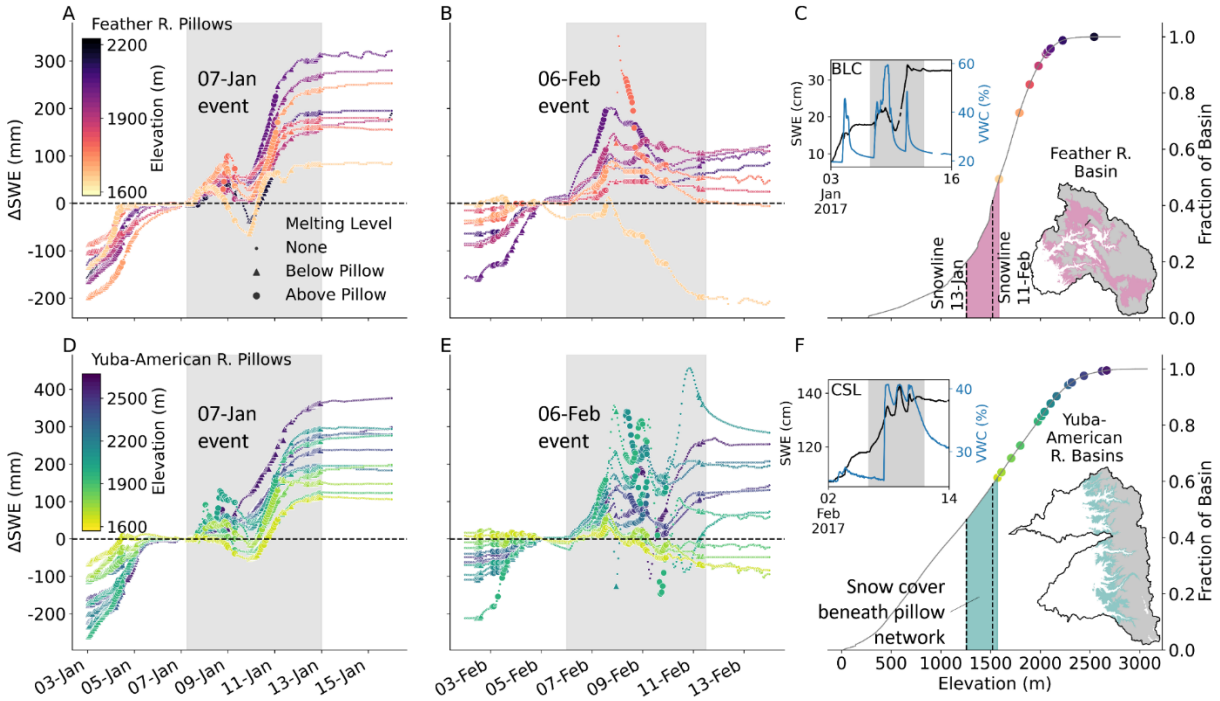

Figure 3.4 Hourly SWE in the Feather River basin for the (A) 7J and (B) 6F atmospheric river events, and in the Yuba and American River basins (D, E) for the same events show the snowpack filling and draining to or above pre-storm levels at high elevations while ablating at lower elevations. SWE values at snow pillows (described in Table F1) are expressed as departures from a date (vertical line) prior to event precipitation. Markers depict the position of upwind snowfall melting levels relative to each snow pillow, which can indicate the likely phase of precipitation. Hypsometric curves are plotted with corresponding snow pillow and post-AR snow line elevations for the (C) Feather and (F) Yuba and American. Corresponding maps show elevation ranges that bound the snow pillow networks (grey), and the "unmonitored" range between the lowest snow pillow elevation and the 13-January (post-7J storm) snowline elevation. Insets in (C) and (F) show collocated SWE and near-surface soil moisture time series during each storm at Blue Canyon (BLC, 1609 m) and the Central Sierra Snow Lab (CSL, 2103 m), respectively.

It is possible that rainfall underestimation makes up for inflated snowmelt contributions to ROS generating extreme runoff. Estimating mountain precipitation is a pervasive hydrometeorological challenge (Lundquist et al. 2019) tied directly to estimating relative snowmelt contributions to TWI. Applying a simple wind-correction factor (Masuda et al. 2019; Appendix I) from hourly reanalyses to gridded precipitation raises 7J and 6F precipitation by 6-12% (Figure 3.5). However, this assumes precision in the precipitation field and accuracy in the

wind field, which tends to be “dulled” over mountain environments (Minola et al. 2020). This, and unaccounted orographic enhancement of precipitation (White et al. 2019), appear to make this correction a lower bound (thereby “deflating” the melt contribution to TWI).

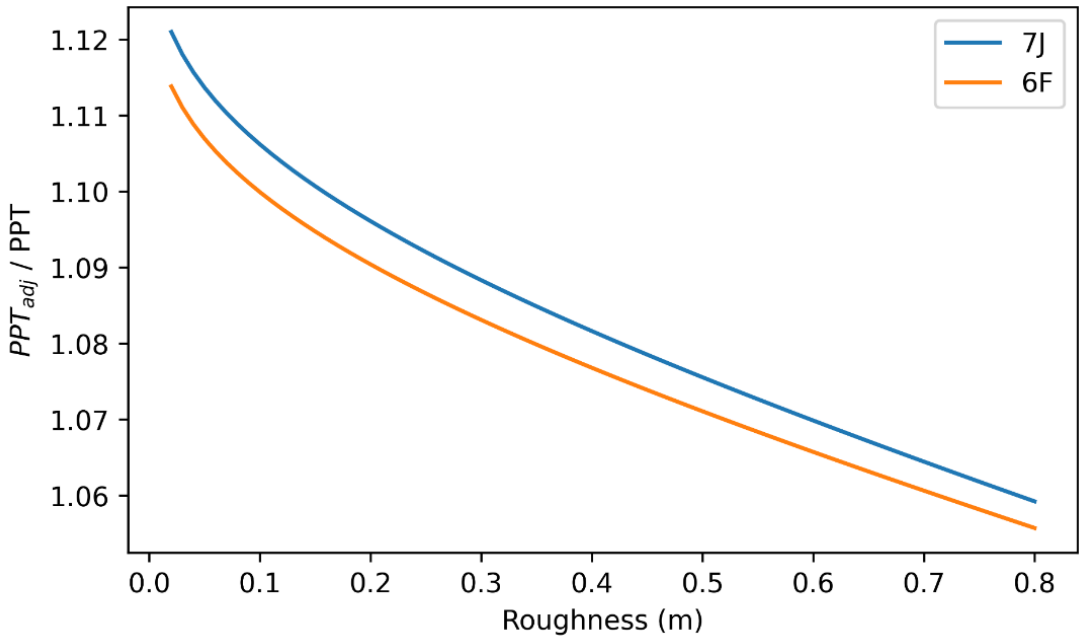

Figure 3.5 The ratio of wind-corrected to raw CNRFC precipitation over the Feather River basin during the 7 January and 6 February storm events at various roughness lengths. Wind correction raises event-total approximately 6 to 12 percent, depending on the land cover.

However, these lines of evidence are partial to exposed, flat terrain. Vegetation tends to collect less snowpack in-stand compared to exposed areas (Musselman et al. 2008), yet it shelters snow from wind-driven turbulent heat exchange, resulting in less-dramatic swings in TWI during ROS (Harr 1986; Marks et al. 1998). Beneath-canopy SWE and its in-storm changes are invisible to both satellite SCA retrievals and snow pillows (which are typically located in flat clearings). Therefore, in a heavily-forested watershed, these uncertainties can affect (1) the location of the regional snowline (as calculated using SCA here) and (2) ROS runoff generation inferred from snow pillows which have limited basin representation (Meromy et al. 2013).

3.2.3 Soils connect and amplify consecutive storms

If snowmelt did not drive extreme ROS runoff, what other process(es) may explain the runoff? A 1:1 ratio of runoff to rainfall requires a saturated basin without losses to deep groundwater stores. During WY 2017, winter precipitation events unfolded successively, such that streamflow across the study basins recessed less with the onset of each storm event (Figure 3.6a). This indicates an increasingly saturated landscape up until the 6F storm cycle, when log-transformed streamflow levels off. Soil moisture, even in snow-covered areas, echoed the streamflow trajectory. Each spell of TWI allowed less drainage to occur (Figure 3.6b-g), bringing soil moisture conditions closer to saturation as winter progressed.

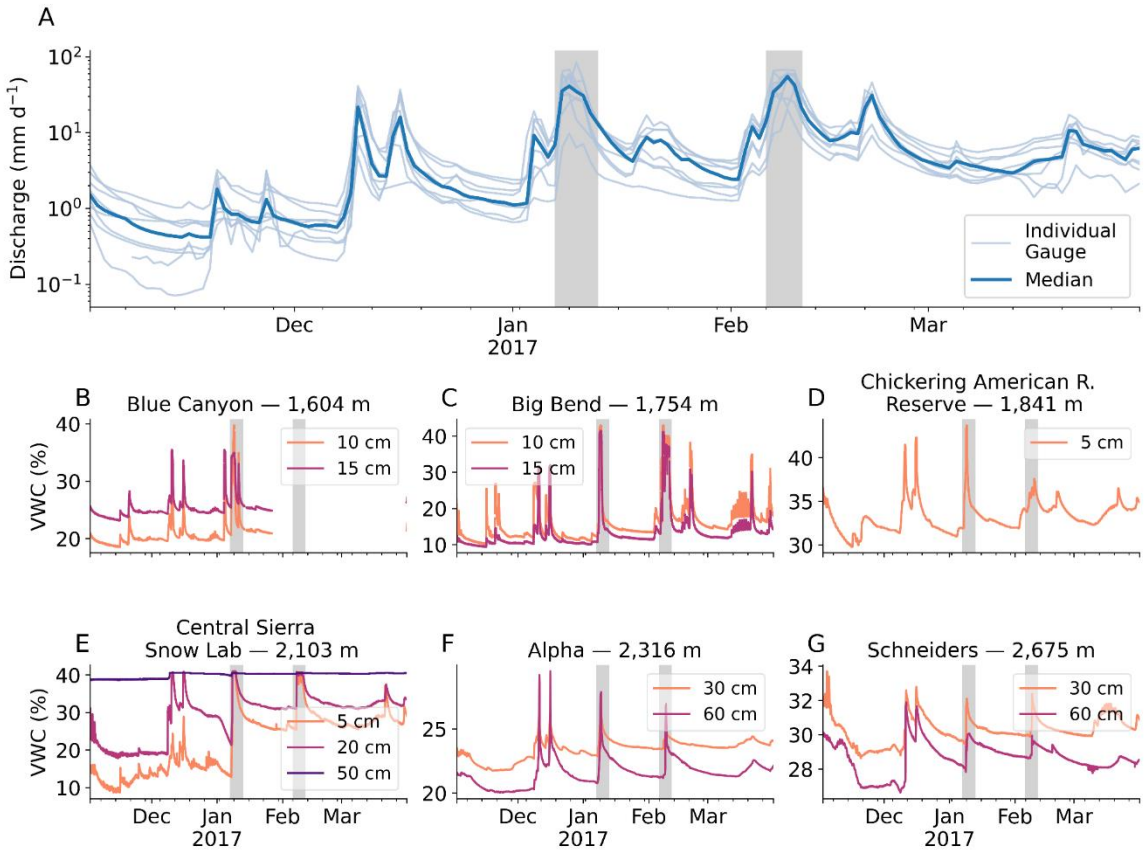

Figure 3.6 Winter (A) daily streamflow at nine gauges and (B-G) hourly soil moisture in the study basins show a growth in baseflow and antecedent soil moisture in response to large consecutive storms. Note that the distribution of soil probe depths varies by location.

These antecedent soil moisture conditions are corroborated by steady increases in groundwater levels, as observed from wells in the Yuba and Feather River basins (cf. Fig. 22 and 23 in Yuba Water Agency 2018). It seems plausible the degree of discharge achieved during the 6F storm sequence was facilitated by the 7J sequence, and in turn, earlier runoff-generating storm events starting as early as mid-October (Sterle et al. 2019).

Increases in runoff efficiency throughout the season underpin observed streamflow. We compared accumulations of discharge to rainfall to test the notion of snowmelt augmenting runoff over rainfall alone. Relative accumulations inherently provide a measure of runoff efficiency, where large snowmelt contributions would be expected to drive runoff in excess of rainfall. Early-season (November-December) rainfall registered relatively small amounts of discharge at each stream gauge (Figure 3.7ai-di; cf. Figure. 2d, 2f in Sterle et al. 2019). Discharge ranged from 32-35% of rainfall in the central Feather and south Yuba gauges (Figure 3.7ai, 3.7ci) to 59% in the Yuba headwaters (Figure 3.7bi). Differences between cumulative discharge and rainfall narrowed after the 7J event (Figure 3.7aii-dii) and narrowed further after the 6F event (Figure 3.7aiii-diii), exceeding rainfall by 8-9% by the end of February. While this exceedance indicates active melt contributions consistent with low-elevation (~1,600 m) snow pillow SWE losses (Fig 3.4), it is considerably weaker than what prior research has indicated (Henn et al. 2020). At the catchment scale, both the 7J and 6F events rather fall into a “passive” classification of ROS in which rainfall is augmented by less than 10% (Brandt et al. 2022).

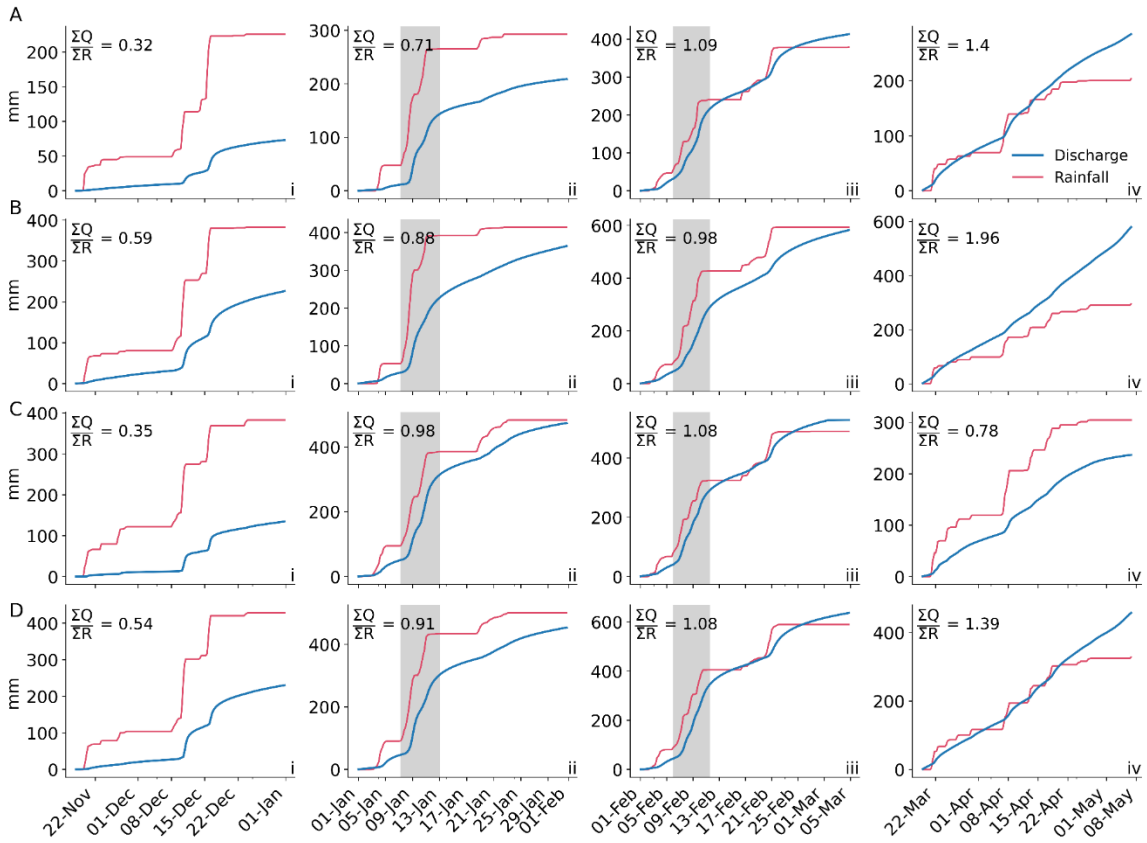

Figure 3.7 Discharge and estimated rainfall accumulations at subdaily USGS gauges during water year 2017 in the (A) central Feather, (B) Yuba headwaters, (C) southern Yuba, and (D) American. Accumulations are separated by (i) early-season, (ii) January – isolating the 7J event, (iii) February – isolating the 6F event, and (iv) spring periods. End-of-period ratios of total discharge to rainfall (ΣQ/ΣR) reflect rising runoff efficiencies through the snow season, highlighting instances of "active" snowmelt (or subsurface) contributions augmenting rainfall.

We also examined a period of spring rainfall as a control case for comparison of winter runoff efficiencies. Spring discharge amounts strongly exceeded rainfall totals (by 39-96%) across most basins at the start of May (Figure 3.7aiv, biv, div), indicating more "active" snowpack contributions to runoff (Brandt et al. 2022). This is unsurprising, as seasonal snowmelt began at most snow pillows by late-March through April (Figure 3.8). Importantly, the near-linear spring discharge accumulation (Figure 3.7aiv-div) is distinct from the relatively abrupt accumulations that followed rainfall in the winter months (Fig 3.7ai-diii).

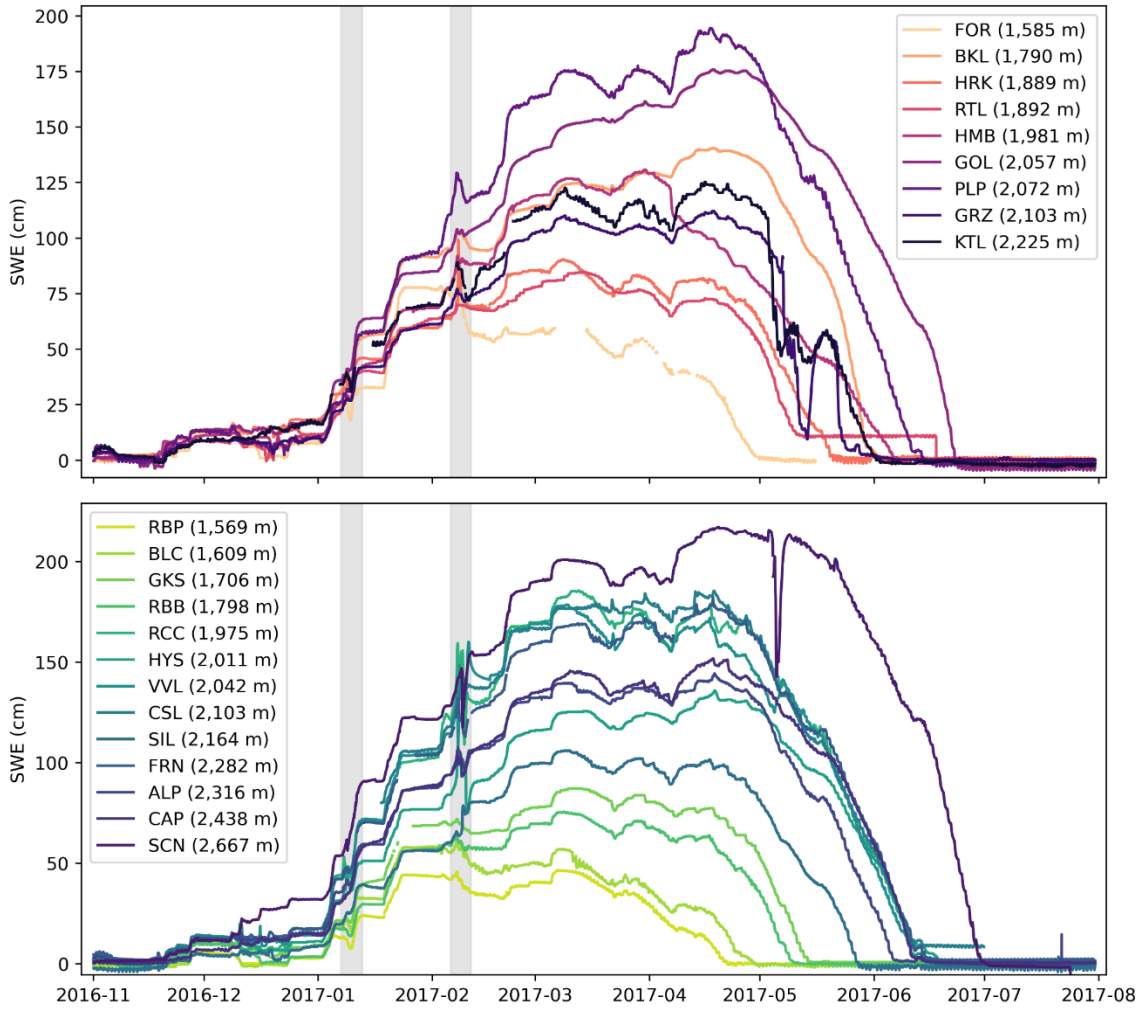

Figure 3.8 Hourly snow water equivalent for the 2017 snow season at snow pillows in the (top) Feather and (bottom) Yuba and American River basins, with January and February storms shaded in grey. Peak snowpack (signaling the start of the season's snowmelt) occurs in March-April at most snow pillows.

South Yuba River streamflow was most "active" in February (Fig 3.7ciii) and recessed in the spring (Fig 3.7civ) – an indication of earlier, modest snowmelt due to its narrow drainage area and minimal snow cover (Fig 3.1a; Fig 3.9). Its runoff efficiency nonetheless increased from the season start. We partitioned rainfall using upwind snow level radars in the Sierra Nevada foothills. While dynamical and thermodynamical processes cause snow levels to bend downwards with increasing elevation along the windward slopes (Minder et al. 2011) (biasing

the local rainfall fraction Lundquist et al. 2008), systematic lowering of the snow levels (Fig. 3.10) minimally affects our interpretation.

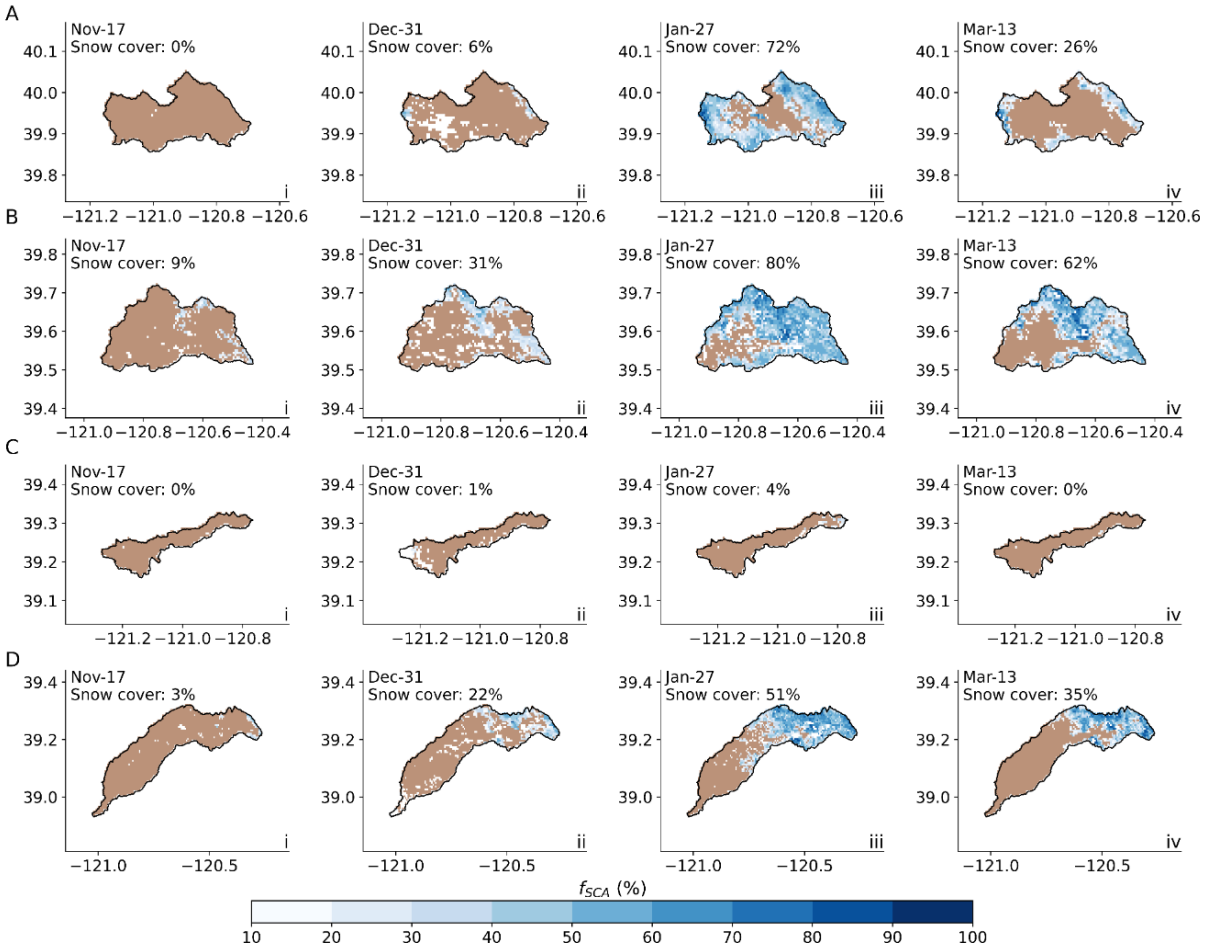

Figure 3.9 Antecedent snow cover of basin areas on clear days preceding the time periods shown in Fig 3.7 and Fig 3.10 below. Drainage areas pertain to USGS gauges in the (A) central Feather, (B) Yuba headwaters, (C) southern Yuba, and (D) American for (i) early-season, (ii) January – preceding the 7J event, (iii) February – preceding the 6F event, and (iv) spring periods. Maps show MODIS fractional snow-covered area (SCA, blue), masking snow-free regions (SCA < 10%, brown). Annotated snow cover percentages reflect the proportion of catchment area that is snow covered (SCA ≥ 10%).

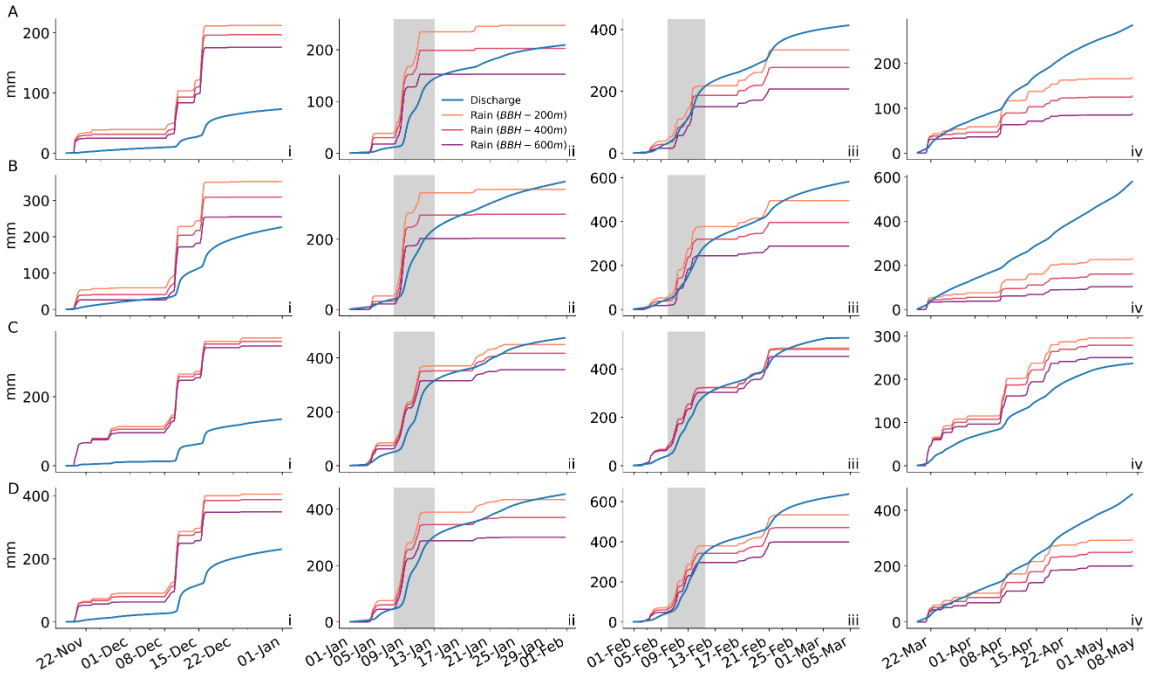

Figure 3.10 Discharge and estimated rainfall accumulations at subdaily USGS gauges in the (A) central Feather, (B) Yuba headwaters, (C) southern Yuba, and (D) American. Accumulations are separated by (i) early-season, (ii) January – isolating the 7J event, (iii) February – isolating the 6F event, and (iv) spring periods. Inset maps in each subplot show the drainage area on a clear day prior to the accumulation period to infer antecedent snow cover. Rainfall was partitioned using upwind snow levels, which are systematically lowered here to explore how snow level "bending" affects the rainfall-discharge relationship.

These results suggest that amplifying discharge beyond rainfall totals requires both saturated soils and additional mass inputs (from either subsurface or snowmelt contributions). We show increasingly efficient winter runoff volumes that modestly exceed rainfall totals despite several large, warm ARs. We suspect this was due to "passive" snowpack conditions, as there is a clear distinction from spring, snowmelt-dominated runoff strongly exceeding rainfall totals. Cases of large, high-efficiency streamflow have been observed in other small, snow-dominated basins in the Western United States – caused by wet soils and winter rainfall occurring during periods of low potential evapotranspiration (Hammond and Kampf 2020; Harrison et al. 2021; Robles et al. 2021). However, disentangling snowmelt and subsurface contributions from rainfall

inputs in driving streamflow generation (Hammond and Kampf 2020), and closing the water balance around these terms remains extraordinarily challenging in snow-dominated headwaters (Safeeq et al. 2021), requiring fully coupled atmosphere-through-bedrock observation and modeling frameworks (Mejia et al. 2012; Siirila-Woodburn et al. 2021). Nonetheless, we found evidence the streamflow associated with ROS can be linked to the subsurface as well as to the role of snowmelt, which we argue was smaller than prior research indicated. This link is crucial because it compels us to acknowledge that the record-setting "Oroville event," hydrologically, was born from a chain of consecutive events that increasingly "primed" the system (McNamara et al. 2005) to respond to a single, high-impact event. Indeed, had a more widespread, "active" snowmelt response transpired during the 6F storm sequence, the risk of dam failure and catastrophic flooding would have arguably been much greater.

3.3 Conclusions

Winter 2017 in California's Sierra Nevada brought numerous landfalling warm ARs and multiple widespread flooding events. Two major storm sequences – beginning on 7 January and 6 February – had high snow levels and yielded extreme streamflow volumes in the Feather, Yuba, and American River basins (Fig 3.1). Both storms shared several synoptic characteristics (Table 3.1), with the February event yielding less rainfall but more runoff than the January event. To explain this difference, we present evidence that snowmelt was not necessarily a primary flood driver, at least to the extent previously suspected. We showed that (1) much of the snow cover on 24 January underlying previous melt contribution estimates (Henn et al. 2020) had vanished prior to the event itself (Fig. 3.3, 3.1c), and that (2) hourly snow pillow responses to ROS revealed a potential for daily data to misinterpret liquid water drainage for snowmelt (Fig. 3.4). As a "passive" response to ROS, snow liquid water content rose to saturation before

draining to pre-storm levels, resulting in snow pillows recording SWE gains and losses as rainfall passed through snow. We posit that snowmelt during ROS was a relatively small part of a broader cause of the extreme runoff in the February event. Rather, the cascade of prior storm inputs gradually increased baseflow and antecedent soil moisture (Fig. 3.6) and, in turn, led to increasingly efficient runoff (Fig. 3.7). This subsurface response links successive storm events together and leads to a hypersensitive response to a single, high-impact storm.

To be clear, the "active" role snowmelt plays in mid-winter ROS flooding ought not to be dismissed. Understanding whether a snowpack will be "active" or "passive" during an event, and landscape saturation levels are critical to physically-grounded assessments of flood risk. Society naturally remembers past "extreme" events – our perceptions of which affect how we prepare and respond to future events (Haasnoot et al. 2011). Thus, an accurate, transferrable understanding and representation of the physical mechanisms of ROS will enable past events to better guide management responses in the future. Our alternative explanation of the chain of events leading up to the February 2017 "Oroville incident" reveals an important ambiguity in the perception of a past event. This demands elevated observational and modeling capacities to identify the correct physical processes and their coupling to interpret such events. We therefore recommend future efforts focus on the following fronts:

(1) Precipitation phase and intensity. This is a foundational yet elusive forcing in mountain environments, and a first-order control on deciphering the relative importance of precipitation versus snowmelt during ROS. Despite improvements in humidity-aware proxies (Marks et al. 2013) and the utility in upward-looking radars (as used here), the optimal approach in estimating precipitation phase is direct observation (Harpold et al. 2017a; Arienzo et al. 2021). This may be partial to daylight hours and ambiguous during mixed-phase precipitation.

However, combining such citizen science with denser, robust observation networks will bolster on-the-ground representation, and may help to better constrain weather model physics (Lundquist et al. 2019) and satellite retrievals of mountain precipitation.

(2) Snowpack structure and energy balance. This largely dictates the volume and timing of the flood response to ROS. Snow pit observations provide snowpack stratigraphy, cold content and liquid water content, helping to identify likely flow regimes and melt response to meteorological inputs. However, bracketing snow pit observations around ROS events requires intensive (and potentially hazardous) field campaigns and an element of luck. Dye tracer experiments carry a similar benefit, but the post hoc nature of these approaches is impractical for hazard risk and water supply monitoring. We recommend cost-effective automated or semiautomated efforts to map (Bonnell et al. 2021; Donahue et al. 2022) and to continuously and noninvasively monitor (Koch et al. 2019; Priestley et al. 2021) these quantities across a range of elevations (Capelli et al. 2022) and land cover types. Process-scale monitoring of "basic" snow properties – which must be coupled with accurate surface and boundary layer characteristics – can be exploited to develop more representative modeling frameworks. Such measurements, for instance, can improve process-aware constraints on the simplifying parameterizations that accompany models. They may also support developing more effective discretization schemes that respect the physical differences between matrix and preferential flow (Wever et al. 2016; Würzer et al. 2017).

(3) Graduation to scale. How the above-mentioned processes translate from the point and hillslope to basin scale is crucial to guide management decisions. Our analyses rely on snow pillow observations located in flat clearings (and satellite estimates of SCA, which are partial to clearings and sparse vegetation). The network extends down to approximately 1,600 m in the

Sierra Nevada yet is above the regional snow line prior to each storm event we investigated (Fig. 3.4c, 3.4f). Lower-elevation ephemeral snow cover, while unmonitored, is likely a more "active" contributor to snowmelt during ROS. While thinner, the areal extent and low cold content of such snowpacks become arguably important in favorable storm sequences (e.g., warm, intense precipitation immediately following snowfall). In-storm shifts in this boundary and its SWE affect the tributary area and volume of ROS response (Kattelmann 1997a) and therefore should be tracked to understand its relationship to basin flood response. Moreover, being able to monitor exchanges between ground and surface water stores would help to evaluate the interrelationship between ROS, ephemeral snow cover, and runoff response as an integrated system. This may benefit from synthesized critical zone observations (Kirchner et al. 2020; Wlostowski et al. 2021) and isotopic analyses (Rücker et al. 2019) across landscapes.

Facing a climate more prone to high-impact ROS (Li et al. 2019; Musselman et al. 2018), even as ROS events themselves become less frequent with snowpack declines (Huang et al. 2022; Li et al. 2019; Musselman et al. 2018), transdisciplinary efforts aimed toward understanding hydrologic connectivity across scales are paramount to overcoming these barriers. In addition to better understanding the governing processes of snowpack flow routing and snowmelt, we emphasize it is also worth looking up, down, and backward – "up" to understand in-storm changes to precipitation phase and boundary layer dynamics; "down" to understand the subsurface role in surface-groundwater exchange and basin-scale runoff generation; and "backward" to consider how soil and snow's "memory" of preceding hydrometeorological events may affect subsequent ones. Such efforts will improve managing water availability and hazard risks posed by ROS in a society dependent on warming winter season precipitation.

Chapter 4 High-impact versus benign watershed responses to rain-on-snow

Kayden Haleakala, W. Tyler Brandt, Benjamin J. Hatchett, and Mekonnen Gebremichael

4.1 Data and methods

This study extends Chapter 3 to (1) illustrate observational limitations during rain-on-snow (ROS) and (2) determine the mechanism(s) that separate benign from extreme ROS events. We use sub-daily measurements in six watersheds spanning an elevation gradient in the Sierra Nevada. All sub-daily values were converted to metric units and UTC.

4.1.1 Extension of in situ measurements

4.1.1.1 Streamflow

Instantaneous (15-minute) stream discharge measurements for WYs 2017 through 2019 at six gauges across the northern and central Sierra Nevada (Figure 4.1a) were obtained from the USGS National Water Information System (https://waterdata.usgs.gov/nwis). Gauges were selected to span an elevation gradient across the Sierra in which the drainage area (obtained from the GAGES-II data set, https://water.usgs.gov/lookup/getspatial?gagesII_Sept2011) either contained or was nearby (within 10 km) snow pillows and/or soil probes (Figure 4.1a). Only six gauges reporting instantaneous measurements were available that satisfied this criteria. Stream gauge and drainage area attributes are listed in Table J1, along with nearby snow pillow assignments. Baseflow was separated from discharge per WY using the Python library Hydrograph-py (https://hydrograph-py.readthedocs.io/en/latest/functions.html).

4.1.1.2 Snow and soil moisture

Hourly snow water equivalent (SWE) from snow pillows were obtained from DWR at stations within ~10 km of the areas draining to the selected stream gauges for WYs 2017 through 2019 (Figure 4.1a). Several DWR stations, including those part of the NRCS snowpack telemetry (SNOTEL) network, monitor soil moisture (i.e., volumetric water content, VWC) and soil temperature. Soil measurements were obtained from their respective network, as not all NRCS soil measurements are available from DWR. We also obtained soil moisture measurements from NOAA PSL and WRCC. VWC values from NOAA PSL were converted from raw reflectometry measurements using the standard coefficients in the corresponding data logger manual (Table 4 in https://psl.noaa.gov/data/obs/instruments/SoilWaterContent.pdf). The probe depth and timestep for soil measurements vary by network (Table J2); all values were aggregated to hourly timesteps. VWC values were screened from analysis if soil temperatures (if available) at the corresponding probe depth dropped below 0˚C. We use a total of 37 stations – 12 of which measure VWC and 9 of which are co-located with snow pillows (Table J2). These data were used (1) qualitatively as corroborating evidence of ROS at a given point in or near the stations' assigned watershed (section 4.1.4) and (2) quantitatively to consider differences between ROS event characteristics (section 4.1.5).

4.1.2 Remote sensing

4.1.2.1 Snow level radars

Brightband heights (BBH) from three upward-looking S-band radars were obtained from NOAA PSL (Figure 4.1a) for WYs 2017-2019. These report the melting level aloft at 10-miute intervals through an algorithm that exploits the reflectivity and Doppler fall velocity associated with melting snowfall (White et al. 2002). Each watershed was assigned to a snow level radar (of the larger network of NOAA PSL radars) by locating the radar nearest to the watershed centroid.

We use the Oroville, Colfax, and New Exchequer Dam radars (Table J3) in this study to partition precipitation into rain and snow (section 4.1.3) and to aid identifying ROS events (section 4.1.4).

4.1.2.2 Snow cover and the regional snowline

Daily 500-m arrays of fractional snow-covered area (SCA) were obtained from the Moderate Resolution Imaging Spectroradiometer (MODIS) Snow-Covered Area and Grain Size (MODSCAG) algorithm (Painter et al. 2009) for WYs 2017-2019. We used SCA scenes over each basin for near-cloudless (below 10%) days. We also manually scanned true-color images from NASA Worldview (https://worldview.earthdata.nasa.gov/) to qualitatively screen cloud cover, as several days yielded erroneously high SCA. Images were additionally screened if sensor zenith angles exceeded 40˚ to minimize the effect of off-nadir pixels stretching near satellite swath edges – potentially obscuring SCA estimates (Dozier et al. 2008). The 40˚ threshold was chosen to compromise the need to minimize the zenith angle with the need for an appreciable sample size. SCA arrays were used to calculate the regional snowline elevation (hereafter "snowline") each day. The snowline is calculated through a search for the elevation value that simultaneously minimizes the number of snow-free pixels above and the number of snow-covered (10% SCA) pixels below a given elevation within a watershed (Krajčí et al. 2014).

4.1.3 Precipitation phase partitioning

Gridded (4-km) 6-hourly precipitation estimates were obtained from the National Centers for Environmental Prediction Stage IV analysis (Du 2011), which mosaics and cleans the quantitative precipitation estimates from each River Forecast Center in the United States. Over each stream gauge's drainage area, precipitation was partitioned into snowfall and rainfall for each WY using the nearest snow level radar. For each WY, we first aggregated the 10-minute BBHs to hourly values and gap-filled the hourly time series using ordinary least squares

regression of hourly BBH against the 0˚C altitude from the nearest hourly ERA5 (Hersbach et al., 2020) pixel. Regression results range from R^2 and standard error values of 0.75-0.94 and 15-23 mm, respectively. Sample sizes range from 292 to 484 (Table K1). Gap-filled BBH time series were then aggregated to 6-hourly values to match the Stage IV precipitation.

Precipitation occurring below (above) the gap-filled BBH was classified as rainfall (snowfall). The tendency for the upwind BBH to bend downward toward windward slopes is a climatological feature in large storm events that averages approximately 170 m in the Sierra Nevada (Minder and Kingsmill 2013). While this presents an uncertainty in discriminating precipitation phase using BBHs (Lundquist et al. 2008), applying a conservative 200-m lowering of BBH minimally affects this study's cataloguing of ROS events (section 4.1.4) and conclusions (Appendix N; Table N1; Figures N1-N5).

4.1.4 Watershed-scale rain-on-snow events

ROS events are often "observed" at monitoring stations that can verify existing snow cover and infer the presence of liquid precipitation (e.g., McCabe et al. 2007; Würzer et al. 2016), which is most reliably done in-person (Harpold et al. 2017a). However, snowpacks can accumulate beneath monitoring networks, making an appeal for using distributed estimates of snow cover and rainfall to detect ROS. While this has been previously done with hydrological model output (Musselman et al. 2018; Li et al. 2019; Huang et al. 2022), such cataloguing of ROS is predicated on the accuracy of (1) partitioning between rain and snow (historically done with an air temperature threshold) and (2) simulating low-lying snow cover dynamics. Both factors may confound ROS detection, as measuring mountain precipitation and simulating ephemeral snow cover remain challenging (Petersky and Harpold 2018; Lundquist et al. 2019).

To avoid these issues, we compare observed BBH with the snowline prior to a given rainfall event to aid in identifying ROS. Rainfall events were first identified per basin if more than 5 mm of partitioned rainfall fell within 30 hours (5 Stage IV timesteps). Additional rainfall occurring within a 30-hour window after previous rainfall was incorporated into the same event. This 30-hour threshold was informed by the NRCS National Engineering Handbook watershed lag method for determining a watershed's time of concentration (NRCS 2004; Appendix L). We chose a conservative value of 30 hours, given the tendency for montane forest environments to have longer concentration times than what may be reliably calculated by this method (Loukas and Quick 1996).

ROS events were identified from rainfall events in two ways. Primarily, events in which BBHs strongly exceeded the pre-event snowline elevation at any point during rainfall were classified as ROS. However, clear-sky SCA scenes are often unavailable immediately before rainfall, and the snowline will recede upslope if there is sufficient energy available to melt snow cover at the edges. This recession occurred frequently between storm events (not during precipitation), when meteorological conditions typically do not favor the development or maintenance of snowpack cold content (Jennings et al. 2018). We account for this snowline withdrawal by extrapolating pre-event snowline estimates with the average withdrawal rate for a given basin, if the pre-event snowline estimate leads the storm event by 7 days or less. Withdrawal rates were calculated by considering the changes in clear-sky snowline changes between storm events in water years 2017-2019 when (1) snowline estimates were less than 4 days apart and (2) when the snowline was at least beneath the 90^{th} percentile of the watershed's elevation. The distributions of withdrawal rates vary by watershed between averages of 33-56 m d^{-1} (Figure 4.2d). Events in which BBHs exceeded this extrapolated pre-event snowline estimate

by ~500 m were classified as ROS. These measures (the BBH offset and the snowline withdrawal estimate) are intended to conservatively infer the presence of ROS within a watershed by mitigating the potential for either (1) the downward bending of snow levels (Minder et al. 2011) to cause one to mis-classify downwind precipitation phase, and/or (2) the uphill withdrawal of snow cover before a storm causing one to mis-interpret rainfall on snow-free areas for ROS. As a secondary measure for inferring the presence of ROS, or in lieu of absent snowline estimates, we inspected hourly SWE during rainfall for "pulse" signatures akin to ROS at snow pillows. We also inspected co-located, shallow (≤ 10 cm) hourly soil moisture for coincident increases, if available (i.e., Figure 3.4). For WYs 2017-2019 across six watersheds, this supervised routine identified a total of 138 ROS events from 310 rainfall events (Table 4.1).

Table 4.1 Rainfall and ROS events identified in each basin and WY.

USGS ID	**Station Name Abbr**	**# Rain (ROS) events**		
		WY 2017	**WY 2018**	**WY 2019**
11381500	Mill C	24 (15)	20 (9)	23 (8)
11402000	Spanish C	19 (8)	15 (5)	25 (9)
11413000	N Yuba	24 (9)	16 (6)	24 (9)
11427000	NF American	24 (13)	18 (6)	26 (17)
11274790	Tuolumne	13 (6)	5 (2)	6 (1)
11266500	Merced	16 (8)	7 (4)	5 (1)

4.1.5 Distinguishing controls on rain-on-snow severity

This chapter aims to identify the mechanism(s) that separate benign from extreme ROS flood events. Conceptually, flood-generating drivers of rainfall intensity and antecedent soil conditions

are well-established (Berghuijs et al. 2016), as is the importance of initial snowpack conditions in generating ROS runoff (Colbeck 1975b; Würzer et al. 2016). Qualitative analyses revealed (1) a potential importance of storm sequencing in driving large ROS floods (section 4.2.2) and (2) that the watershed responses to ROS in which streamflow exceeded rainfall were not necessarily synonymous with large ROS floods (section 4.2.3). To this end, we considered several related covariates in addition to storm, snow, and soil properties in separating large from minor ROS events in terms of their flood volume. Covariates are described in sections 4.1.5.1 and 4.1.5.2 below. For each covariate, we separated the distribution of values for the highest 30% of all ROS events ("large") from those for the remaining 70% of ROS events ("minor"). This partitioning aimed to isolate extreme events without diminishing sample size, but we also tested separating events by 20-80%, and 10-90% (Appendix M). We compared these distributions using an unpaired Mann-Whitney U test.

4.1.5.1 Antecedent conditions

We consider pre-ROS event SWE, soil moisture, and snowline elevations. Since availability of snow pillows vary across watersheds (i.e., Figure 4.1a shows the northern-most watershed to contain 1 snow pillow near its peak), antecedent SWE was taken from the highest-elevation snow pillow associated with a given basin (Table J1). Antecedent SWE for a given event was discarded from analysis if no SWE values were reported within 12 hours of the event. Otherwise, the SWE value most-immediately preceding the event was used. We consider antecedent soil moisture from shallow (the shallowest of all available probe depths) and deep (the deepest of all available probe depths; Table J2) soil layers in watersheds that contain soil measurements (i.e., the southern 4 basins in Figure 4.1a). Antecedent soil moisture values in a basin were calculated as the average quantile of all station quantiles associated with a given basin. Quantiles were

determined from a station's distribution of soil moisture values across WYs 2017-2019. Pre-event snowline elevations were considered if the clear-sky snowline estimate preceded a given event by less than 5 days. Snowlines were considered here as percentiles of watershed elevation.

We also consider the WY accumulated rainfall to date before a given event, and the number days since a prior rainfall event of at least 10, 50, and 100 mm. These variables represent the degree to which a watershed is "primed" from prior TWI that may not be readily evident from in situ soil measurements.

4.1.5.2 Storm event conditions

We consider several ROS event characteristics pertaining to the defined rainfall event time frame (section 4.1.4). These include the intensity, duration, and total accumulated depth of rainfall, as well as the BBH gradient. Rainfall intensity was taken as the quotient of total event rainfall and duration. Event gradients in BBH were calculated as the ordinary least squares regression slope of the hourly BBH. We hypothesize that increasing BBHs are significant drivers of large ROS floods, as these in-storm variations in the rain-snow transition can create an ephemeral snow cover that receives immediate rainfall.

Lastly, as a measure of runoff efficiency and an indirect measure of additional snowmelt or subsurface contributions to runoff during ROS, we consider the ratio of event-total streamflow (Q) to event-total rainfall (R). Streamflow totals include the 30-hour concentration time in this ratio (hereafter referred to as QR). Conceivably, strongly "active" snowmelt or subsurface contributions to ROS, coupled with a saturated landscape and minimal losses to groundwater stores, will drive QR values to exceed 1.0. It is possible, however, for actively melting snowpacks during ROS to produce QR values less than 1.0 if transmission losses are considerable. While it is difficult to partition snowmelt from subsurface contributions to

streamflow at the basin scale (Safeeq et al. 2021), their joint effect is nonetheless crucial in producing greater peak flows than what rainfall may produce alone. We consider basin responses to ROS with QR ≥ 1.0 as "hyperactive," and hypothesize that they significantly separate extreme from benign ROS events.

4.2 Results and discussion

Results here begin with two examples that illustrate observational "hazards" when interpreting ROS and the potential importance of storm sequencing on ROS flood severity. This is followed by a formal analysis of all ROS events across study basins and WYs across the metrics described in section 4.1.5.

4.2.1 Ambiguity in available observations

Independent of issues in discriminating rainfall from snowfall (Harpold et al. 2017a; Lundquist et al. 2019), the definition of ROS depend on the measurements available and a given study's purpose (Brandt et al. 2022). Some definitions impose requirements of minimum snow depth or SWE, their negative change (indicating snowmelt), a seasonal window of occurrence, or an upper limit on the snowpack's cold content if utilizing output from a hydrological model (McCabe et al. 2007; Wayand et al. 2015; Musselman et al. 2018; Li et al. 2019; Huang et al. 2022). However, ROS can technically occur and produce TWI without considerable snowmelt or in unsaturated snow (Singh et al. 1997; Wayand et al. 2015; Würzer et al. 2016; Heggli et al. 2022). Daily timesteps are commonly used, conceivably because they are typically quality-controlled (e.g., daily NRCS SNOTEL measurements are checked manually) and are communicated effectively for most purposes. Finer-timescale measurements on the other hand can often be noisy and require rigorous cleaning and/or smoothing before use (Lundquist et al. 2008; Avanzi et al. 2014). However, daily timesteps and particular snowpack requirements can

affect both (1) the cataloguing of ROS events themselves and (2) how the process-level impact of those events are assessed.

Here we show an example that contrasts daily and hourly SWE changes during ROS events near/along the North Fork American River basin in WY 2018. Three separate rainfall events, each yielding streamflow responses (Figure 4.1b), span the snow accumulation and ablation periods in early spring (Figure 4.1c). The first event was snowfall-dominated – hourly and daily SWE both rose unanimously (Figure 4.1di, 4.1ei) – but began with rainfall, as indicated by early, modest increases in shallow soil moisture (Figure 4.1fi). The second event led to the season's peak flow and generated "pulse"-like snowpack responses in which hourly SWE quickly rose and fell (Figure 4.1eii). While some oscillations are more dramatic than others, most are in sync with co-located soil moisture responses (Figure 4.1fii) indicating TWI. Higher-elevation locations (~2,000 m), with SWE either oscillating mildly or accumulating, still generated TWI. This response to rainfall strongly suggests a "passive" routing of rainfall through snow in which snowpack saturates and drains with the transmission of rainfall, rather than active snowmelt. Even after the ablation period began, hourly SWE and soil moisture traced a similar relationship in response to rainfall (Figure 4.1eiii, 4.1fiii).

Daily SWE measurements of the same events tell a different story. While the overall trends in daily and hourly SWE are in agreement across events, snowpack responses to ROS go broadly undetected at a daily timestep (Figure 4.1d). Taking the second event, for instance (Figure 4.1dii), at face value may falsely suggest that ROS was not prevalent at elevations above 1,600 m. This runs contrary to evidence of snow levels nearly peaking above the watershed (Figure 4.2a) to produce widespread TWI (Figure 4.1fiii) and the annual peak flow (Figure 4.1b). The early April event in this case may be correctly identified as ROS by daily changes in SWE, as

snowpack declines coincide with event rainfall (Figure 4.1diii). However, hourly SWE oscillations suggest that the passage of water through snow are again smoothed over.

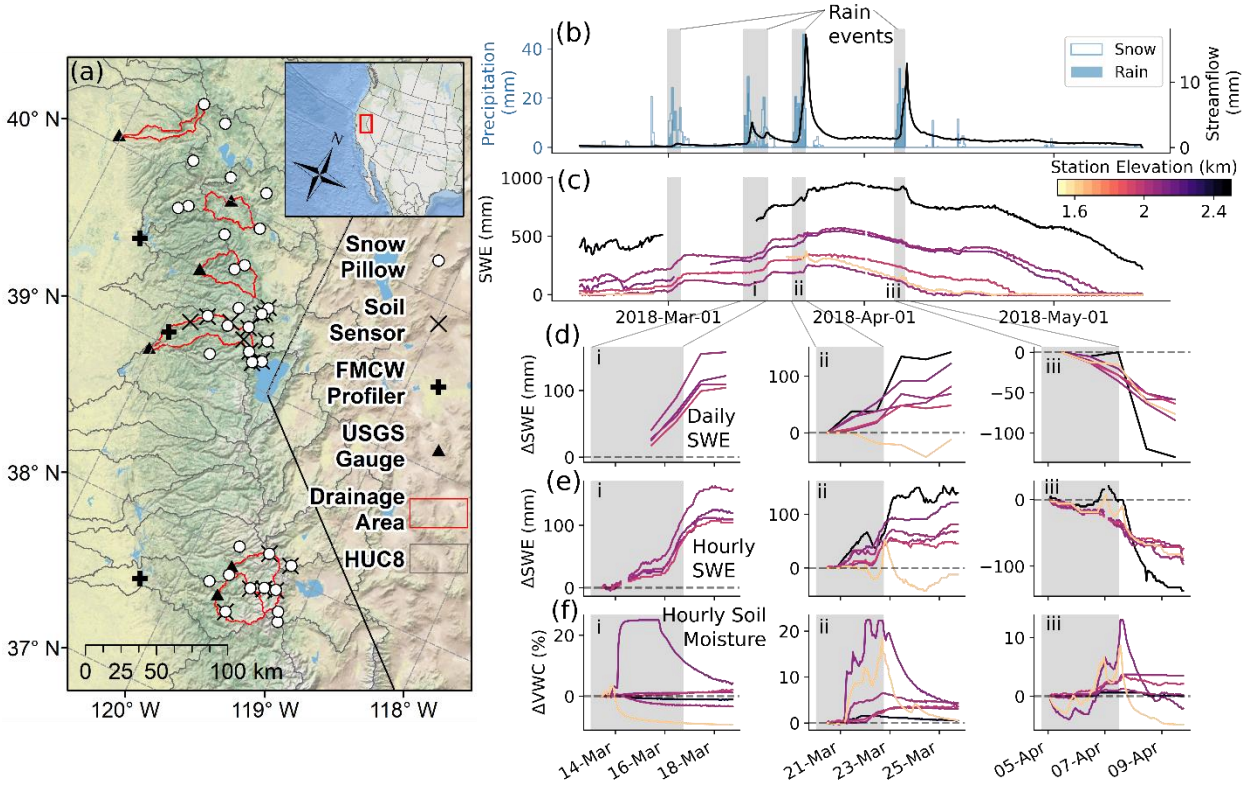

Figure 4.1 (a) Six watersheds spanning California's northern and central Sierra Nevada contain or neighbor hourly or sub-hourly snowpack and soil measurements, with downstream/upwind snow level radars. A series of rainfall events occurred in the spring of 2018 over the North Fork American River Basin, with corresponding streamflow responses (b) and SWE from in-basin or neighboring snow pillows (c). For three events with the largest streamflow response (i, ii, and iii), daily changes in SWE (d) leads one to detect and interpret ROS differently than from hourly SWE (e) and hourly shallow (≤ 10 cm) soil moisture (f).

Daily SWE values from the DWR network of snow pillows are sampled from a single hourly timestep ~ 0300-0400 local time (~1100-1200Z). Conceivably, sampling snapshots at various snowpack saturation stages 24 hours apart make the snowpack water balance of ROS ambiguous. For instance, increases may appear as the retention and/or re-freezing of rainfall within the snowpack as opposed to its temporary saturation, while decreases may appear as snowmelt as opposed to the drainage from temporary saturation. This very feature of increased SWE followed

by immediate decreased SWE during warm storms was a main conclusion of Chapter 2 in this dissertation (Haleakala et al. 2021). Importantly, this ambiguity can affect the interpretation of ROS at a daily timestep (via the contribution of snowmelt to TWI), as TWI may be dulled or double-counted, depending on the stages of snowpack saturation that are sampled. Therefore, sub-daily snow measurements should be supported with other variables (to the extent available) (Hatchett et al. 2020) to appropriately classify and interpret ROS.

4.2.2 Uncertainty in unavailable observations

Diverse and detailed measurements, however, are sparse and must be placed strategically – they must consider jointly snowpack representativeness, line power, and accessibility (Molotch and Bales 2005; Bales et al. 2006). Little to no long-standing snowpack measurements exist below 1,500 m in the Sierra Nevada, as the original intention of snow pillow measurements were to characterize the mountain water supply. As a result, this perspective of the "passive" snowpack response to ROS is likely relatively "cold" because it applies to deeper snowpacks than what may be present beneath the extent of the observation network. SCA, however, can temporarily reach beneath 1,000 m in the Sierra, where snowpacks are arguably more readily "active" contributors to TWI. While lower-elevation, ephemeral snowpacks can accumulate and store less SWE (Hatchett 2021), they can still elevate ROS flood risk (Kattelmann 1997b; Brandt et al. 2022). Depending on the hypsometry and vegetation distribution in a watershed (White et al. 2002; Wayand et al. 2015), rainfall alone over a tributary area can elicit a large flood response. This makes the coincident timing of warm storms potentially important after anomalously-low snowfall.

Extending the example case in the North Fork American, the peak flood events for both WYs 2018 and 2019 coincided with a low snowline elevation just prior to intense rainfall inducing

widespread ROS (Figure 4.2a, 4.2b). Each peak event deposited low-lying snow cover at the storm conclusion and was followed by more rainfall events approximately 1.5 to 2 weeks later. Between these rainfall events, the snowline receded uphill by 248 m in 9 days in late March 2018 (Figure 4.2a), and 247 m in 4 days in February 2019 (Figure 4.2b). These are lower-bounded estimates of snowline withdrawal given that cloud cover obscured SCA images on days closer to the later storm events.

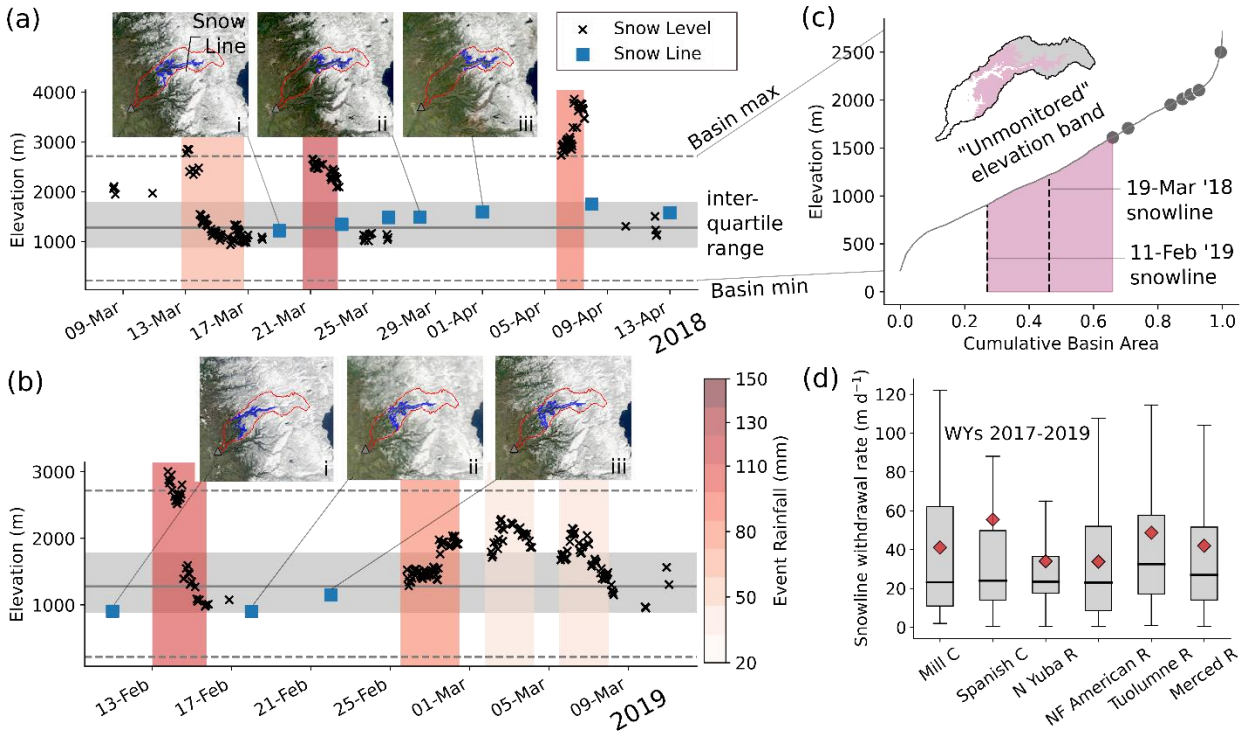

Figure 4.2 Atmospheric snow level and terrestrial snow line elevations in the North Fork American River Basin during storm sequences in (a) spring 2018 and (b) winter 2019. Inset maps illustrate the antecedent snow cover and the snow cover withdrawal before and after heavy ROS events. (c) The snow lines extend far below the distribution of monitoring stations over an expansive "unmonitored" area along the basin hypsometry. (d) The distribution of rates at which the snow line recedes uphill after storms during the snow season (with red markers showing averages in each basin) is generally slow and right-skewed, presenting an elevated ROS flood risk in consecutive storm events.

The ephemeral snow loss associated with these snowline withdrawals do not yield a streamflow response or a considerable response from a lower-elevation (1,048 m) soil sensor as

much as rainfall inputs do (Figure 4.3), suggesting a likely negligible snowmelt volume. A similar sequence of events was observed surrounding the Oroville ROS event in the Feather River basin in mid-late January 2017 (Figures 3.1 and 3.6). Provided these events occur in late winter when potential evapotranspiration is characteristically low (Hammond and Kampf 2020), it is plausible that this ephemeral snow is lost to the antecedent conditions of oncoming storm events. However, the extent to which this snow loss contributes to landscape wetting is unclear, as this temporary "unmonitored" region can account for up to 39% of basin area (Figure 4.2c). Moreover, the information content in SCA images is limited in heavily-forested areas. Beneath-canopy SWE – which is commonly shallower but protected from turbulent heat exchange compared to clearings (Musselman et al. 2008) – is invisible to satellite SCA retrievals, which can conceivably lead to underestimating ground-SCA in dense forest regions.

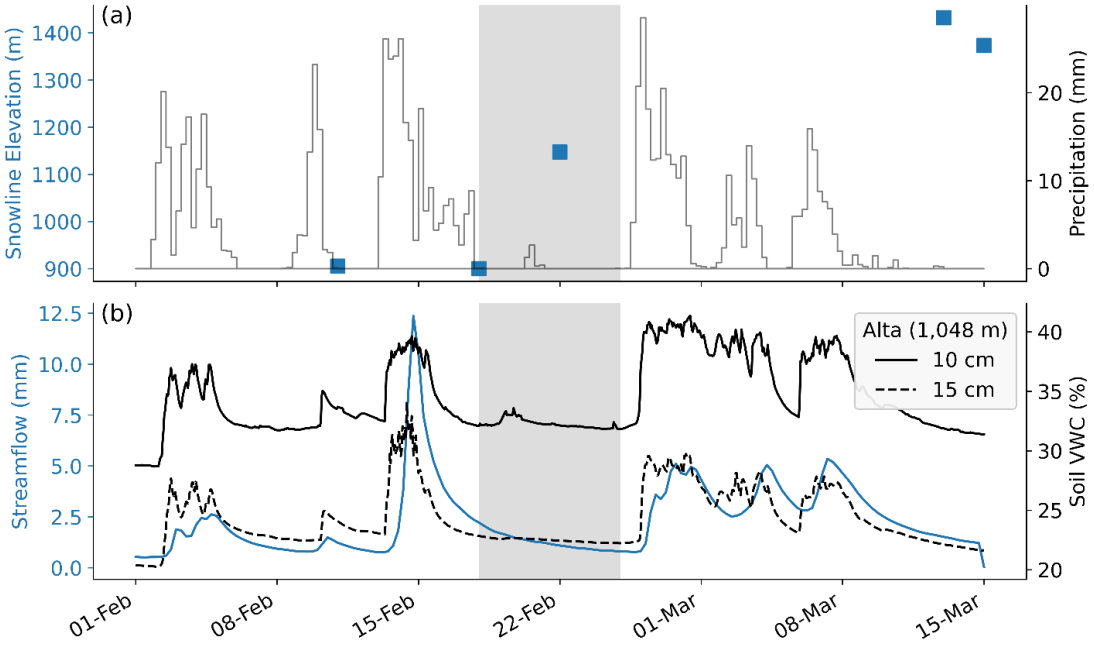

Figure 4.3 (a) Snowline elevations and 6-hourly precipitation, and (b) streamflow and in situ soil moisture (at Alta) in the North Fork American River basin in February 2019. The shaded region shows a period between large storm events in which the snowline recedes uphill from 900 m, but does not yield a strong streamflow response at the watershed outlet or a strong soil moisture response at a 1,048 m sensor.

The uphill withdrawal of the snowline nonetheless has strong implications for ROS flood risk. The distribution of withdrawal rates after storm events in the snow season is strongly right-skewed and generally slow. In the North Fork American, rates average approximately 34 m d^{-1} (Figure 4.2d). Depending on the union of the area between isothermal snowpack and rainfall along a watershed's hypsometry, "active" ROS responses may occur in favorable circumstances that go undetected by the current real-time observation network. A warm storm immediately following a cold event may generate high-impact ROS flooding (Kattelmann 1997b), as the risk of coupling ephemeral low-lying snowmelt with imminent rainfall requires time to subside. Several documented ROS events shared, to some extent, a withdrawn snow cover before rainfall occurred (Hatchett 2018; White et al. 2019; Henn et al. 2020; Brandt et al. 2022). Arguably, the peak flows from such events would have been greater had the sequence of prior storm events been grouped more closely.

4.2.3 Hydrologic connectivity across storm events

The above examples set a precedent for considering the importance of storm sequencing in ROS flooding at the watershed scale. This notion also extends to storm events that generate TWI that are not necessarily associated with ROS but nonetheless induce flooding. The effect of consecutive storm sequencing on flooding is readily evident in streamflow trajectories (Figure 4.4a). Particularly for the wet WYs 2017 and 2019, the local minima of streamflow increase log-linearly over the winter and spring seasons. On the other hand, WY 2018 (a relatively dry year), does not see the same gradual increase over the winter, but does so in the spring as a result of several storm events and snowmelt. This suggests that there is an extent to which runoff volume (and runoff efficiency) is "built" by prior storm events (producing TWI) that are large enough to irreducibly raise landscape saturation levels within a year. The sustained, "stepwise" increases in

streamflow and soil moisture after large storms (e.g., Figure 3.6, Figure 4.5, and Figure 2 in Sterle et al. 2019) point to a well-connected watershed, where imminent inputs stand on top of its memory of the season's prior inputs.

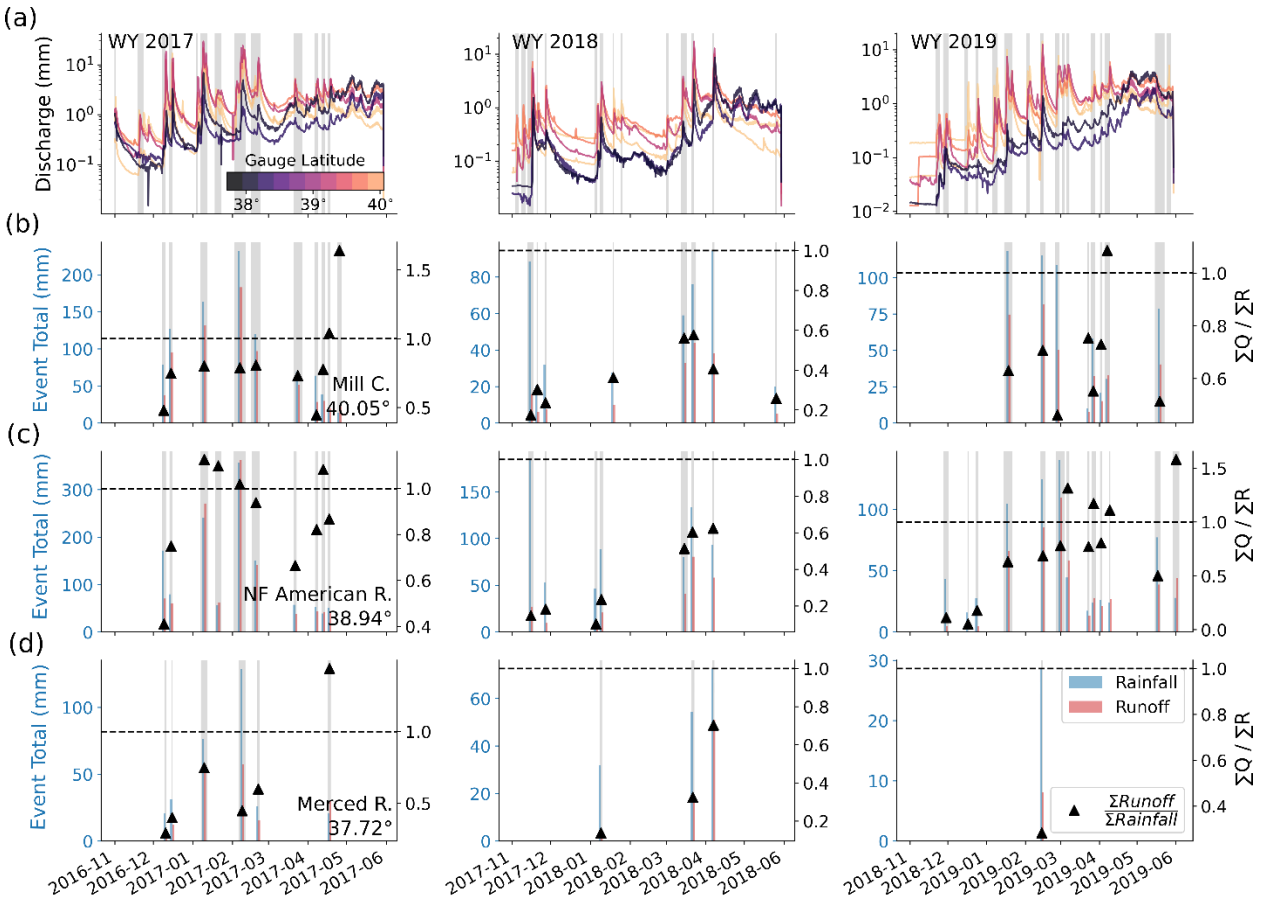

Figure 4.4 (a) Natural log of 6-hourly streamflow for WYs 2017-2019 at each stream gauge in Figure 4.1a. For select gauges in the (b) northernmost (Mill Creek), (c) central (North Fork American River), and (d) southernmost (Merced River) regions in this study, ratios of total event streamflow to rainfall are plotted for each ROS event.

Streamflow and soil moisture behaviors indicate that this concept also applies to shorter timescales. When rainfall events are clustered within days of each other, peak flows generate that are unable to completely recess before a following event occurs. These sequences produce responses to rainfall in which QR ratios increase progressively (Figure 4.4b-d). In WYs 2017 and 2019, QR values in some large ROS sequences exceed 1.0 in the latter event(s) of a given group

of storms. Such “hyperactive” watershed responses to rainfall are most commonly observed after April, as seasonal snowmelt begins to predominate streamflow volumes.

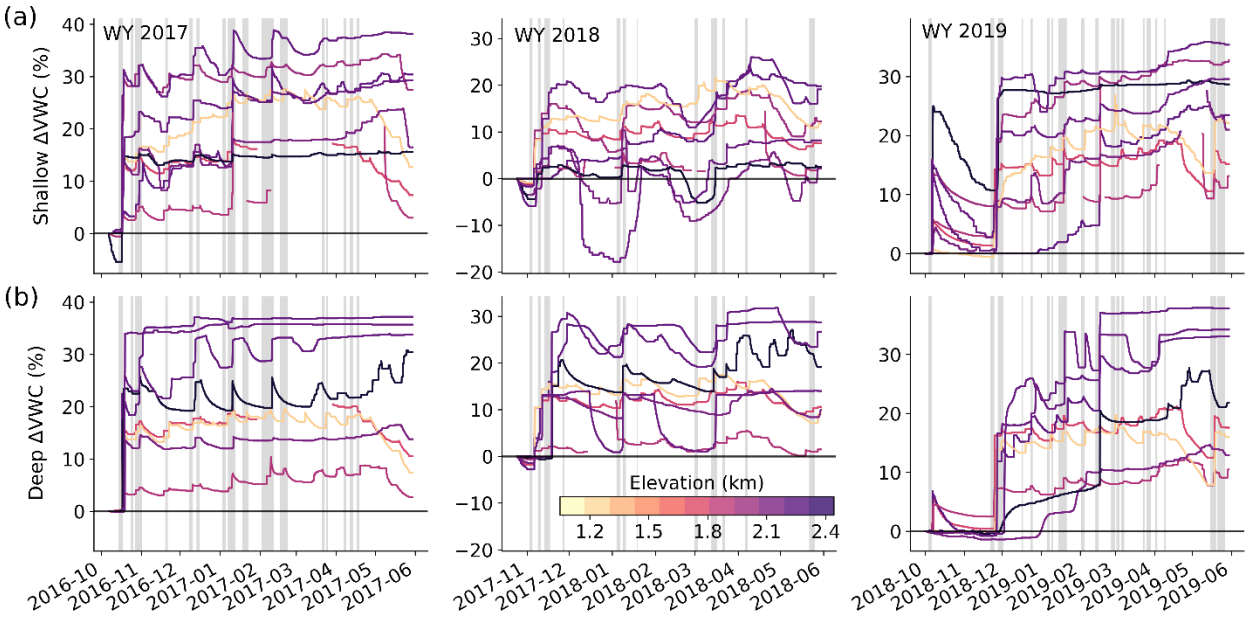

Figure 4.5 (a) Shallow (≤ 10 cm) and (b) deep (≥ 10 cm) changes in soil moisture since the start of the WY at sensors within or near the North Fork American River basin in WYs 2017-2019. Start dates were chosen to precede the WY’s first storm event. Hourly values are expressed as a 5-day rolling minimum to illustrate increases in landscape wetting over the season.

However, particularly large winter ROS events can elicit a hyperactive watershed response (e.g., in January 2017; Figure 4.4c). It is also important to note that not all ROS event clusters that produce a hyperactive basin response yield extreme runoff (e.g., in late March 2019 in the North Fork American; Figure 4.4c). Conversely, not all ROS cases where QR values are less than 1.0 yield benign runoff volumes (e.g., in December 2016 and in March-April 2018; Figure 4.4b-d). Nonetheless, the increase in runoff efficiency (whether through snowmelt, increases in baseflow, or both) resulting from immediately prior events supports the notion that smaller, but timely storm groups are an important flood forecasting consideration (Fish et al. 2019).

4.2.4 Key differences of high-impact rain-on-snow

What drives large ROS floods if they are not always synonymous with "active" snowpacks or "hyperactive" watershed responses? The role of rainfall in ROS flooding, at least in the Sierra Nevada, is well-known (Kattelmann 1997b; Wayand et al. 2015; Li et al. 2019; Brandt et al. 2022). It is therefore unsurprising that the intensity, duration, and volume of rainfall in large ROS events are significantly greater than those in minor ROS events (Figure 4.6a-c), irrespective of the threshold separating large from minor events (Figure M1a-c, M2a-c).

Differences in SWE prior to large versus minor ROS events are limited (Figure 4.6d). This is likely an artifact of selecting the highest elevation snow pillow in each watershed such that all basin "peaks" are represented, since the northernmost watershed contains one snow pillow at its peak (Figure 4.1a). It is uncommon for storm melting altitudes to exceed peaks of 3,000-4,000 m in the Sierra Nevada (Hatchett et al. 2017). High-elevation SWE may therefore not drive a large difference in ROS flood severity, even if rainfall is widespread across majority of a watershed.

The extent of the snow cover, on the other hand, yields a larger difference across large versus minor ROS events (Figure 4.6e), with larger events having lower pre-event snowlines. This illustrates the importance of low-lying snow in contributing to large ROS flooding. While there are many minor ROS events associated with a nearly completely snow-covered landscape, majority of those events take place in the southernmost Tuolumne and Merced River basins where stream gauges reside at elevations that may exceed the snowline in some cases (gauge elevations are ~1,170 m). Pre-event snowlines are arguably important if considering regions beneath these gauges. Indeed, excluding these two basins from this analysis results in a greater (and statistically significant) difference in the pre-event snowline distributions between large and minor ROS events (Figure M3a, e, h).

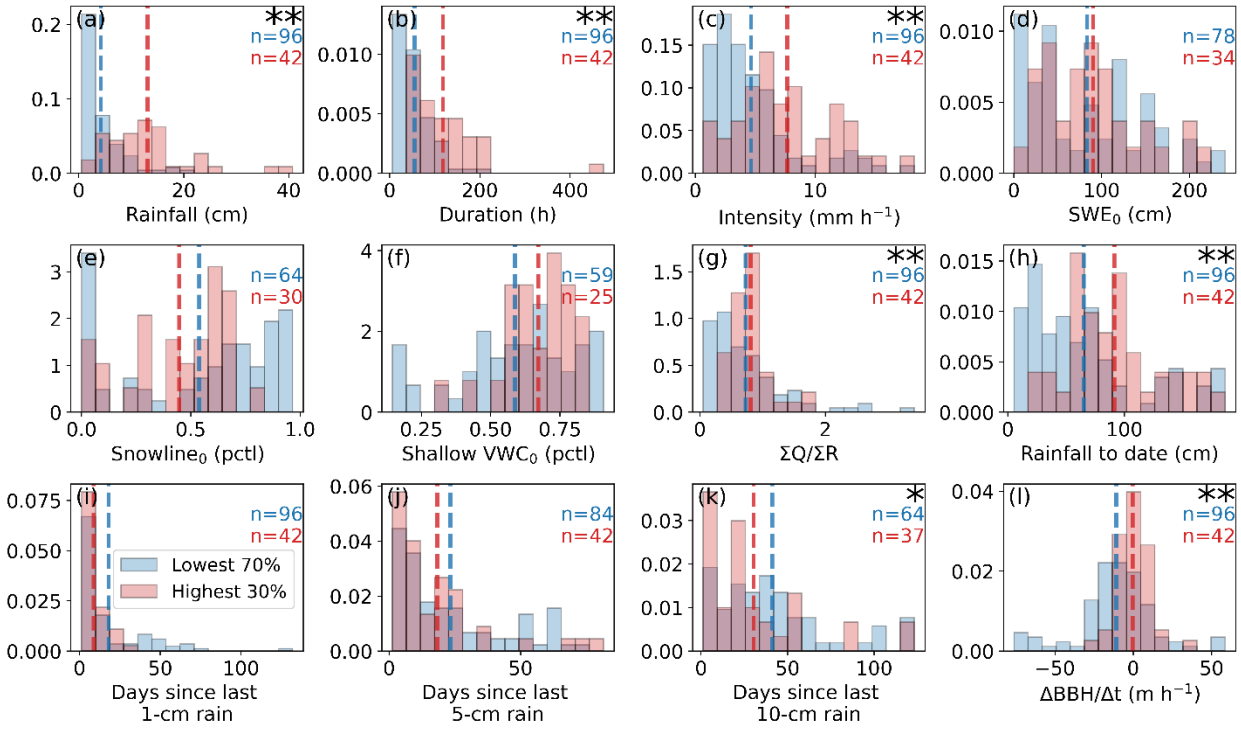

Figure 4.6 Density histograms comparing attributes of ROS events that generate the 30% highest and 70% lowest runoff volumes of all ROS events in all six study basins in WYs 2017-2019. Vertical dashed lines indicate distribution averages. Sample sizes are annotated beneath indicators of statistically significant differences between distributions using the Mann-Whitney U test ("" and "**" indicate significance at α=0.05 and α=0.01 levels, respectively). ROS event attributes are (a) total event rainfall, (b) event duration, (c) rainfall intensity, (d) initial SWE at the highest-elevation snow pillow within the watershed, (e) initial snowline elevation as a quantile of basin elevation, (f) average initial shallow soil moisture as a quantile of WY 2017-2019 soil moisture, (g) the ratio of event runoff to rainfall, (h) the WY rainfall accumulation prior to the given ROS event, (i, k, k) the number of days since a rainfall event accumulating at least 10, 50, and 100 mm of rainfall, and (l) the regression slope of the in-storm BBH.*

As expected, relatively drier soils (particularly at depths shallower than 10 cm; Figure 4.6f) precede minor ROS events compared to large ROS events, which follow wetter soil conditions. However, several minor ROS events were preceded by saturated soil conditions, indicating it is not the only salient ingredient in generating large ROS responses. Similarly, deep antecedent soil moisture indicates little difference across large versus minor ROS events (Figure M3b, f, i).

Event ratios of streamflow to rainfall confirm the hypothesis that large ROS floods have watershed QR values significantly greater than in minor ROS events (Figure 4.6g, M1g, M2g). However, neither large nor minor events' QR values are exclusively below or above 1.0. The distribution of large-event QRs tend to group more closely to 1.0, and its mean straddles 1.0, indicating the importance of runoff efficiency in generating a large ROS response.

The rainfall to date (Figure 4.6h) and the time since a prior rainfall event of differing magnitudes (Figure 4.6i-k) clearly illustrate the notion that large ROS events are somewhat "built" by prior events. Large ROS responses follow wetter periods (Figure 4.6h) compared to minor ROS responses. On a similar note, while the average number of days since prior rainfall is lower for large ROS events (indicating the importance of storm sequencing), they differ insignificantly from minor ROS events if the prior rainfall event is small (≤ 50 mm total; Figure 4.6i-j). The difference between large versus minor ROS events is significant, however, when considering the days since large (100 mm) rainfall events (Figure 4.6k). This result is robust across definitions separating large from minor ROS events (Figure M1i-k, M2i-k), and demonstrates the ability for watersheds to become "primed" from prior inputs (McNamara et al. 2005) to produce high-impact responses to ROS. Similar observations of montane watershed memory affecting runoff responses to heavy rainfall have been made in the southern Appalachian mountains (Nippgen et al. 2016; Miller et al. 2021) and the Swiss Alps (Khanal et al. 2019).

Lastly, in-storm variations in BBH mark a significant difference between large and minor ROS events (Figure 4.6l). Generally, large ROS events tend toward an increasing BBH. However, the distribution is clustered around a BBH gradient of zero, while many of the minor ROS events occupy both tails. Considering only cases in which the BBH increases during the

event yields a mostly insignificant difference across large versus minor ROS events in which the BBH slope is suppressed in larger events (Figure M3c, g, j). While the hypothesis regarding the importance of in-storm increases in BBH is not supported in this case, it is crucial to note that the mechanism underlying its importance can span across multiple events. The concept of an "upside-down storm" (Hatchett et al. 2016) involves the deposition of snow immediately before rainfall occurs. While an in-storm increase in BBH creates this situation in one continuous motion, this circumstance may take place across different storm events (i.e., beyond a brief threshold used to separate storm events, as done here). This again underscores the importance of considering storm sequencing in high-impact ROS, particularly when a prior event deposits a low-lying ephemeral snowpack (Figure 4.6e, M3a).

4.3 Conclusions

Mountain ROS can generate historic flooding and may become more severe in a warmer future, following more volatile precipitation regimes (Gershunov et al. 2019; Rhoades et al. 2020). Delineating what separates the benign from the most hazardous ROS events, however, is difficult to parse at the watershed scale due to limited observational capacity. This study (1) illustrates several examples of such observational limitations in identifying and interpreting ROS, and (2) describes likely mechanisms that distinguish large from minor watershed ROS responses during WYs 2017-2019 in California's northern and central Sierra Nevada.

Snow pillow measurements of SWE take snapshots of the above-ground snowpack mass. At an hourly timescale, rainfall may infiltrate, saturate, and drain from the snowpack, creating a "pulse"-like SWE signal in accordance with increases in soil moisture. We show that this can be the case in both the accumulation and melt season (Figure 4.1e, f), and can go undetected at a daily timescale (Figure 4.1d), whose sampling can occur haphazardly at various snowpack

saturation stages. Cataloguing and interpreting ROS should therefore be done with care, utilizing fine-scale ancillary measurements to the extent available. However, SCA (and by extension the risk of ROS) extends beyond the reach of observational networks. Snowfall in the Sierra can drive snowlines as low as 900 m (Figure 4.2b, 4.3a), which withdraws at rates between approximately 33-56 m d^{-1} in the snow season. This suggests that the sequencing of storm events plays a crucial role in enhancing ROS flood risk, which is supported by a SCA-aware assessment of 138 ROS events.

Results show a tendency for clusters of ROS events to produce "hyperactive" watershed responses in which runoff volumes exceed rainfall (Figure 4.4). Low-lying snow cover, wet soils, and prolonged, high-intensity rainfall are all significant contributors to high-runoff ROS (Figure 4.6). Importantly, the largest watershed responses to ROS often connect to prior water inputs. The most dangerous scenarios occur when prior storms produce large volumes of TWI with "stepwise" increases in streamflow and soil moisture (Figure 4.4a, 4.5), priming the landscape for a highly-efficient response (Fish et al. 2019; Miller et al. 2021). This mechanism makes a significant difference between large and minor ROS runoff responses, where high-impact responses occur soon after large (100 mm) storm events rather than relatively smaller (≤ 50 mm) events (Figure 4.6i-k). These results begin to show constraints on catchment memory in response to high-impact events, which may offer predictive power in future flood forecasting efforts in the face of more frequent extreme precipitation events.

APPENDICES

Appendix A – Snow pillow selection process (Chapter 2)

We obtained hourly SWE, temperature, and snow depth from the California Data Exchange Center for the full network of 122 sites above 1500 m claiming to have hourly measurements for WY 2010 through 2019. Individual seasons for SWE and temperature were visually screened for obvious errors (e.g., extensive gaps or "flatlined" time series). Seasons with below-7.5 cm peak SWE were then discarded, followed by sites having less than 5 seasons of jointly available SWE and temperature measurements.

We reduced this sample (due to extensive quality control requirements, Appendix B) to represent a latitudinal and elevational transect across the Sierra Nevada while keeping at least one site per basin. Sites having a greater number of seasons with simultaneous SWE, temperature and depth measurements were given preference over other sites in the same basin. Twenty-eight sites remained after this step (Table A1).

Table A1 DWR snow pillow metadata for accumulation seasons (water years) 2010 to 2019. Columns '10 to '19 indicate which site-years are considered in this study. A value of 1 indicates use of SWE and temperature data. Asterisks indicate coincident use of snow depth.

ID	Name	Basin	Operator	Z (m)	Lon.	Lat.	Region	'10	'11	'12	'13	'14	'15	'16	'17	'18	'19
HIG	Highland Lakes	Trinity	USBR	1838	-122.48	41.09	North	1*	1*	1*	1*	1	1	0	1*	1*	1
MUM	Mumbo Basin	Trinity	USBR	1722	-122.52	41.2	North	1*	1*	1*	1*	1*	0	0	1*	0	1
BLA	Blacks Mountain	Sacramento	CADWR	2149	-121.2	40.77	North	1*	1*	1*	1*	1*	0	0	0	1*	1*
STM	Stouts Meadow	Sacramento	USBR	1646	-121.94	41.17	North	1*	1*	1*	1*	1*	1*	0	1	1	1
GRZ	Grizzly Ridge	Feather	CADWR	2103	-120.64	39.92	North	1	1	1	1	1	1	1	1	1	1
HRK	Harkness Flat	Feather	CADWR	1890	-121.28	40.42	North	1*	0	1*	1*	1	1*	1*	1*	1*	1
SQV	Squaw Valley Gold Coast	Truckee	NRCS	2442	-120.28	39.19	North	1*	1*	1*	1*	1	1*	1*	1*	1*	1*
INN	Independence Creek	Truckee	NRCS	1962	-120.29	39.49	North	1*	1*	1*	1*	0	1*	1*	1*	0	1*
CXS	Carson Pass	American	NRCS	2548	-120	38.69	Central	1*	1*	1*	1*	1*	1*	1*	1*	1*	1
SIL	Silver Lake	American	USBR	2164	-120.12	38.68	Central	1*	1*	1*	1*	1*	1*	1	1	0	1
CSL	Central Sierra Snow Lab	Yuba	NRCS	2101	-120.37	39.33	Central	1	1	1	1	1	1	1	1	1	1
BLK	Blue Lakes	Mokelumne	NRCS	2459	-119.93	38.61	Central	1*	1*	1*	1*	1*	1*	1*	1*	1*	1
GNL	Gianelli Meadow	Stanislaus	USBR	2560	-119.893	38.2	Central	1*	1*	1*	1*	1*	1*	1*	1	1	1
STR	Ostrander Lake	Merced	CADWR	2499	-119.55	37.64	Central	1*	1*	1*	0	1	1	1	1	1*	1*
TUM	Tuolumne Meadows	Tuolumne	CADWR	2621	-119.35	37.88	Central	1*	1*	0	1*	1*	1*	0	1	1*	1*
EBB	Ebbetts Pass	Carson	NRCS	2640	-119.8	38.55	Central	1*	1*	1*	1*	1*	1*	1*	1*	0	1*
EP5	Echo Peak 5	Tahoe	NRCS	2377	-120.08	38.85	Central	1*	1*	1*	1*	1*	1*	1*	1*	1*	1*
TCC	Tahoe City Cross	Tahoe	NRCS	2072	-120.15	39.17	Central	1*	1*	1*	0	0	0	1	1*	1*	1*
LVT	Leavitt Lake	Walker	NRCS	2927	-119.62	38.28	Central	1*	1*	1*	1*	1*	1*	1*	1*	1*	1*
VRG	Virginia Lakes Ridge	Walker	NRCS	2865	-119.23	38.08	Central	1*	1*	1*	1*	1*	1*	1*	1*	1*	1*
GEM	Gem Pass	Mono	CADWR	3277	-119.17	37.78	South	1	1	1	1*	1*	1*	1*	0	0	0
SLK	South Lake	Owens	CADWR	2926	-118.56	37.18	South	1*	0	1*	1	1*	1*	1*	1	1*	1*
MHP	Mammoth Pass	Owens	USBR	2835	-119.03	37.61	South	1*	1*	1*	1	1*	1	1*	1	1*	1
KSP	Kaiser Point	San Joaquin	USBR	2804	-119.1	37.29	South	1*	1*	1*	1*	1*	1*	1*	1*	1*	1*
MTM	Mitchell Meadow	Kings	USACE	3018	-118.71	36.74	South	1	1	1	1	1	1	1	0	1	1
GNF	Giant Foreset	Kaweah	USACE	2027	-118.77	36.56	South	1	1	1	1	0	0	0	1	1	1
QUA	Quaking Aspen	Tule	CADWR	2195	-118.54	36.12	South	1*	1*	1*	1*	1*	1*	1	1	1	1
CHP	Chagoopa Plateau	Kern	CADWR	3139	-118.45	36.5	South	1*	1*	0	1*	1*	1*	1	1	1*	1

Appendix B – Snow pillow data quality control measures (Chapter 2)

Remaining sites were cleaned to remove erroneous measurements, which can be unique to each instrument and result in physically unrealistic states/changes. After converting the raw data for each variable to metric units (˚C for temperature and cm for SWE and snow depth), we supervised the following routine to flag observation errors, followed by manual corrections of remaining errors.

Air temperature:

- Flag (and treat as missing) raw temperatures with absolute values exceeding 40˚C.
- Flag hourly changes exceeding 20˚C.
- Flag consecutive repeated observations lasting over 3 hours.

Snow Water Equivalent:

- Flag raw SWE below (above) 0 (380) cm.
- Set summer (July-September) values to zero. This step helped to automate identifying the accumulation season, as particular site-years contained out-of-season measurements above the true peak SWE and below the 380-cm threshold.
- Flag "spiked" SWE, i.e., instances where the absolute value of an hourly increment matched that of a preceding of succeeding increment of opposite sign. We set a 0.2-cm detection threshold for these occurrences and replaced flagged values with those bounding them.
- Flag hourly changes exceeding 60 cm.

Snow Depth:

- Flag raw depths below (above) 0 (750) cm.

- Similar to SWE, set summer depths to zero and flag spikes and hourly changes exceeding 60 cm.
- Smooth depths using a robust discretized spline (Garcia 2010).
- Flag gaps exceeding 12 h to avoid the spline misrepresenting the data.

This routine removed most obvious errors, which enabled automatically defining the accumulation season. We define the accumulation season as beginning on the later date between 1 November and when SWE first exceeds 2.5 cm, and ending at peak SWE. Subtle errors and outliers remained despite the above-mentioned routine, particularly in SWE and snow depth. For example, "spikes" can interrupt trending and stationary observations. They can also occur over periods longer than 1 hour, reflected by measurements "jumping" to consecutive values before returning to the previous neighborhood. This can occur over trending or stationary periods as well, leaving undetected outliers in the automatically processed data. We manually flagged these sorts of post-routine occurrences during the accumulation season.

During snowfall, a bridging effect may result from a frozen snow layer preventing added snow to be recorded by the pillow until the bridge breaks. This is characterized by stationary SWE accompanied by increasing depth, following by an abrupt increase in SWE. While the 60-cm change filter can flag the bridge breaking, the above-described routine does not detect its development. We visually inspected each site-year with available SWE and depth for these instances.

Lastly, we only considered relatively complete site-years of SWE and temperature. We disregarded a site-year if its union of SWE and temperature for the accumulation season was less than 75 percent complete. Similarly, we retained snow depth observations at least 75 percent

complete during the accumulation season. The resulting data set includes a total of 252 site-years of SWE and temperature for 28 sites (Table A1). 175 include depth measurements.

Appendix C – Snow pillow voltage coherence (Chapter 2)

Hourly SWE measurements can be problematic due to battery voltage dependence on air temperature which can be manifested as oscillating SWE measurements. Figure C1 demonstrates one case of a strong correspondence between SWE and voltage. We applied a multi-taper spectrum estimate (Thomson 1982; Riedel and Sidorenko 1995) to the hourly time series of SWE, temperature, and voltage for one winter (December through March). The concurrent peaks in the spectra at several of the same frequencies denote a coherence between SWE and voltage, shown by the large variations in the SWE time series. Figure C2 shows another case without this spectral coherence, which has consequently smoother SWE measurements. Of the sites used in our study with available voltage measurements, the majority of the instances of strong coherence between SWE and voltage occurred during periods insignificant to the analyses (i.e., outside of defined accumulation or ablation events) and did not considerably impact our results.

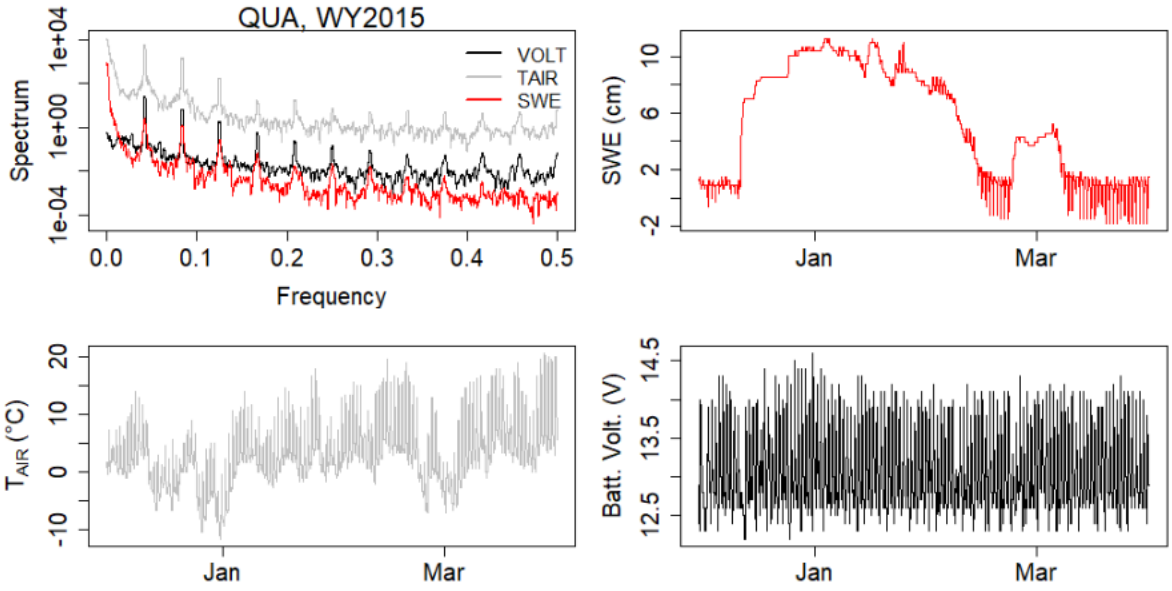

Figure C1 Strong coherence between SWE, voltage and air temperature. The upper left panel shows multi-taper spectral estimates for SWE, temperature, and voltage peaking at similar frequencies. Other panels show the winter (December through March) hourly time series of each variable used in the spectral estimate.

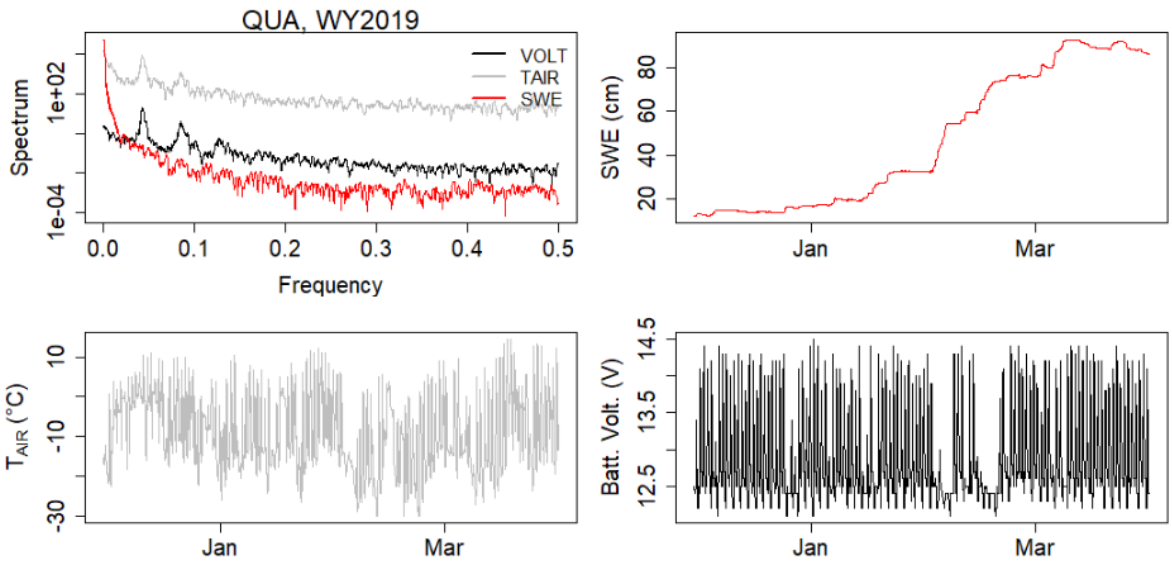

Figure C2 Same as Figure C1, but for weak coherence.

Appendix D – Temperature sensor examination (Chapter 2)

Artificial warming trends were observed due to snowpack telemetry temperature sensor upgrades (Oyler et al. 2015; Rangwala et al. 2015), which present a risk of compromising any temperature-derived indices. To be conservative, using DWR sites with available daily maximum and minimum temperature measurements, we compare monthly temperatures (Nov-Apr) with the nearest grid of the extended Hamlet and Lettenmaier (2005) (HL05) data set (Figures D1 and D2). The double-mass curves (in cumulative K) demonstrate no significant breaks for the water year 2010-2014 overlapping time period.

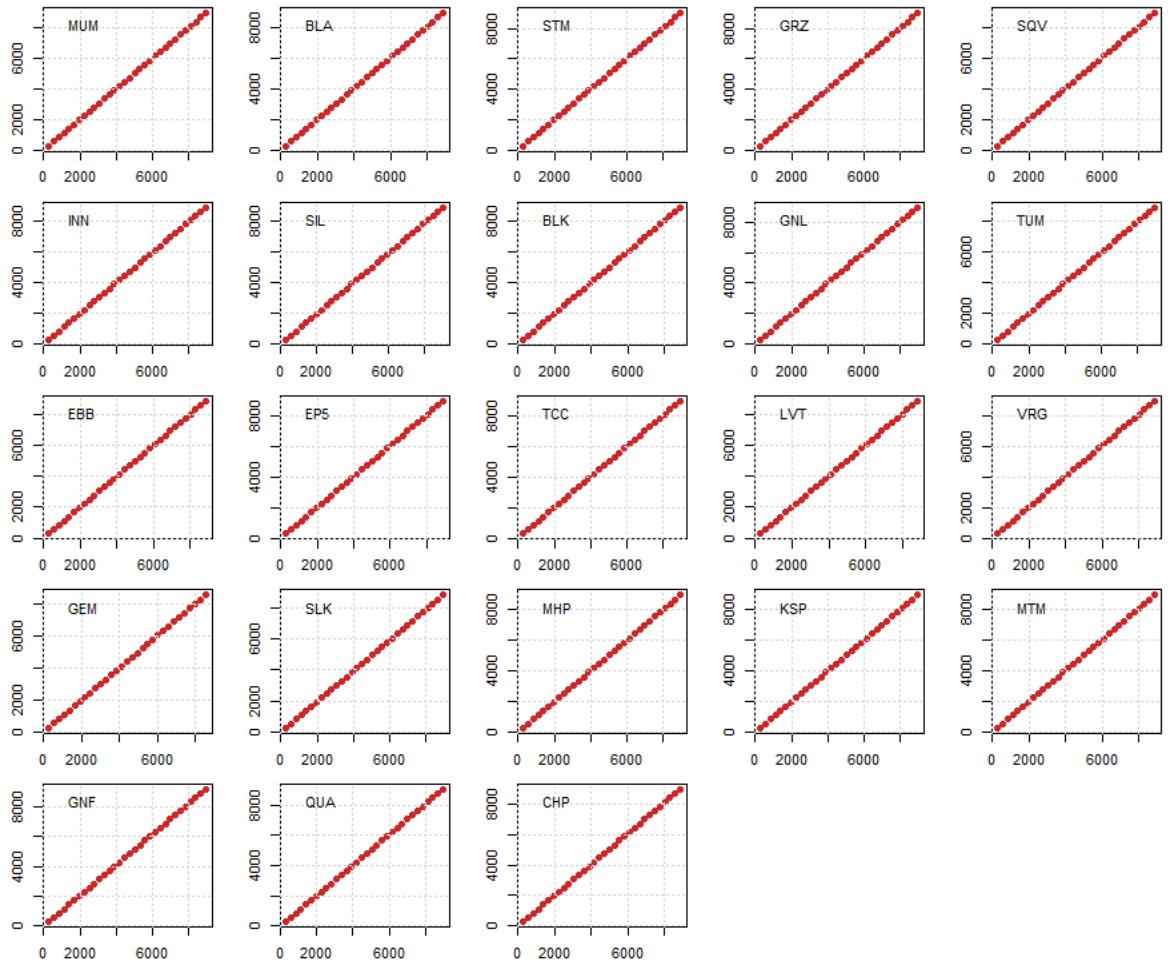

Figure D1 Double-mass curves of monthly mean maximum temperature comparing each snow pillow (x-axis) to the nearest grid in (HL05). Units are in cumulative K.

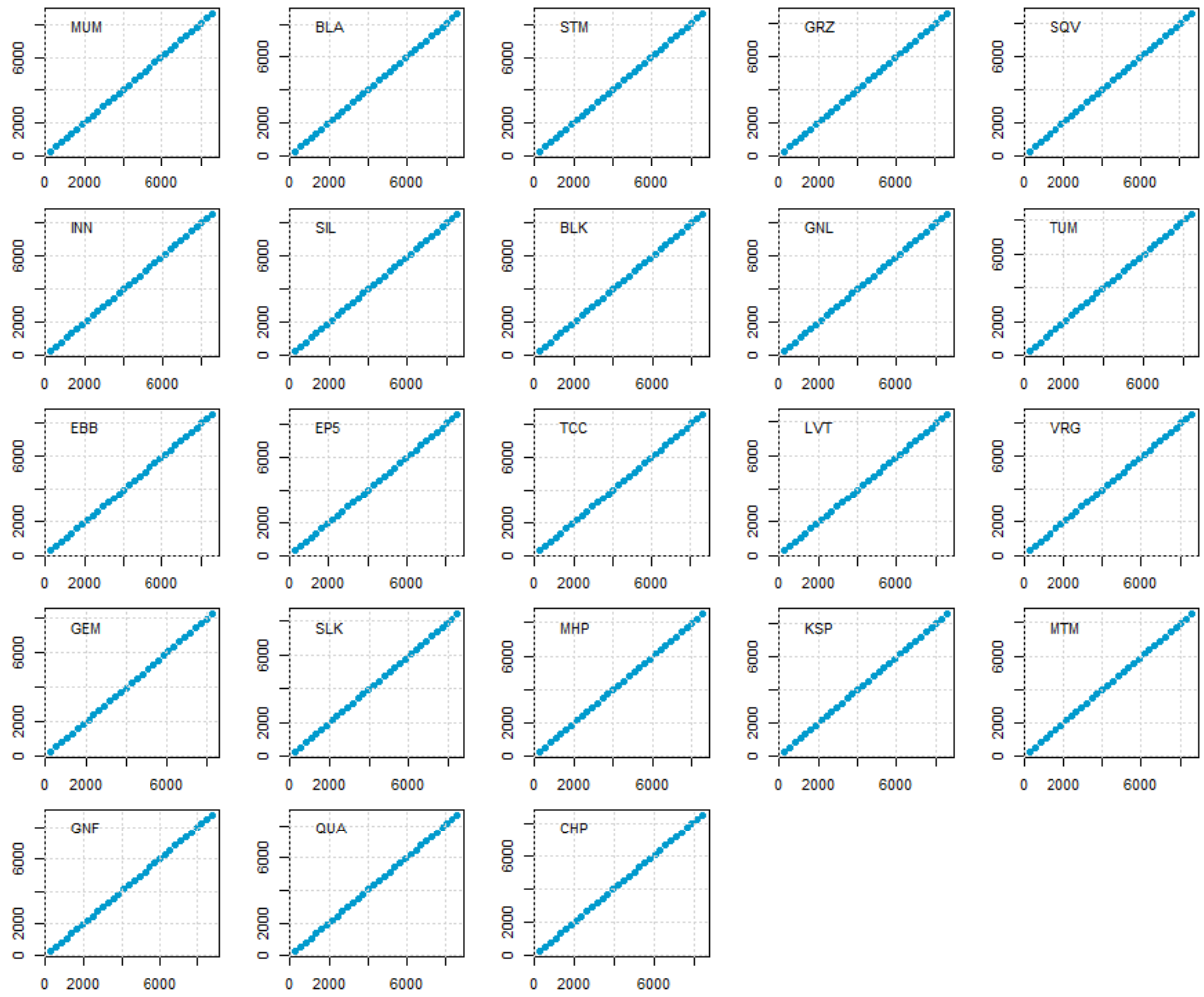

Figure D2 Same as Figure D1, but for monthly mean minimum temperature.

Appendix E – Snow level radars (Chapter 2)

The NOAA Hydrometeorology Testbed (HMT) provides a comprehensive set of radar and surface meteorological measurements in the Western U.S., including wind and precipitation profiles, atmospheric snow levels, and surface water vapor metrics. Several fixed, vertically pointing S-band (2.8 to 3.0 GHz) HMT radars began operation along the western slopes of the Sierra Nevada in the late 2000s and early 2010s. They are designed to observe a minimum effective reflectivity of 10 dBZ at 5 km above the ground. These snow level radars (SLRs) operate at a vertical resolution (i.e., range gate spacing) of 40 m and a nominal temporal resolution of 36 s. While subject to ground clutter contamination at the lowest gates, their upward view prevents contamination from complex terrain, and their operating frequency enables sensitive detection of melting levels during intense storms (Johnston et al. 2017; Ecklund et al. 1999). The height at which falling snow melts is estimated by the radar brightband height (BBH), which is derived from an automated algorithm that inspects range gates for the maximum reflectivity and increasing Doppler fall velocity associated with melting snowfall (White et al. 2002). The BBH, estimated at 10-min intervals, approximates the height at which half the hydrometeor mass in the atmospheric column has melted, though it should be noted that the melting and brightband layers themselves can be up to hundreds of meters thick (Stewart et al. 1984; Braun and Houze 1995).

BBH measurements from SLRs provide precipitation phase inferences at a high temporal resolution, as orographic precipitation events having a low BBH relative to the ground surface likely indicate snowfall rather than rain. However, applying measurements directly to downwind terrain is complicated by a tendency of the melting layer to bend toward the windward slopes (Medina et al. 2005; Minder et al. 2011). This effect results in melting layer offsets on the order

of hundreds of meters lower than the free-air measurements upwind (Minder et al. 2011; Minder and Kingsmill 2013; Medina et al. 2005; Lundquist et al. 2008; Brandt et al. 2020). Lundquist et al. (2008) observed errors between 325 to 450 m when BBHs were used directly as melting level quantities over the North Fork of the American River basin, and Mizukami et al. (2013) demonstrated a marginal (but not universal) improvement over temperature-based precipitation phase classification when SLR-based BBH was used to simulate streamflow. Similar simulation results were reported by Maurer and Mass (2006).

We reduced this SLR-related uncertainty to the extent possible by using the SLR nearest to each snow pillow site. As indicated in Table E1, we assigned each pillow to an SLR based on its location along the primary storm track perpendicular to the Sierra Nevada crest (Figure 2.1a). Sub-hourly BBHs were aggregated to an hourly time step to match the surface snow and meteorological observations. We compared snow pillow elevations to BBHs during periods of SWE change. Accounting for downward bending of the BBH near the mountain range, BBHs higher than the snow pillow elevation indicated possible rain, whereas lower BBHs indicated highly probable snow.

Table E1 HMT snow level radars and accompanying snow pillows. Snow pillow IDs correspond to the 3-character DWR code (mapping to snow pillows in Figure 2.1a).

Profiler (ID)	**LON**	**LAT**	**Z (m)**	**Assigned DWR Sites**
Shasta Dam (std)	-122.429	40.716	202	HIG, MUM, BLA, STM
Oroville (ovl)	-121.488	39.532	114	GRZ, HRK
Colfax (cff)	-120.938	39.080	644	SQV, INN, CXS, SIL, CSL, BLK, EP5, TCC
New Exchequer Dam (ner)	-120.278	37.597	259	GNL, STR, TUM, EBB, LVT, VRG, GEM
Pine Flat Dam (pfd)	-119.332	36.830	184	SLK, MHP, KSP, MTM, GNF, QUA, CHP

Appendix F – Station metadata (Chapter 3)

Table F1 Snow pillows used in Chapter 3 obtained from the California Department of Water Resources' California Data Exchange Center. Stations are organized by river basin group and elevation (as in Figure 3.4).

Station Name	ID	River Basin	Longitude	Latitude	Elevation (m)	Operator
Four Trees	FOR	Feather	-121.32	39.81	1,586	CA DWR
Bucks Lake	BKL	Feather	-121.25	39.85	1,790	CA DWR
Harkness Flat	HRK	Feather	-121.28	40.42	1,890	CA DWR
Rattlesnake	RTL	Feather	-121.04	40.13	1,893	CA DWR
Humbug	HMB	Feather	-121.37	40.12	1,981	CA DWR
Gold Lake	GOL	Feather	-120.62	39.67	2,057	CA DWR
Pilot Peak	PLP	Feather	-120.88	39.79	2,073	CA DWR
Grizzle Ridge	GRZ	Feather	-120.65	39.92	2,103	CA DWR
Kettle Rock	KTL	Feather	-120.72	40.14	2,225	CA DWR
Robbs Powerhouse	RBP	American	-120.38	38.90	1,570	SMUD
Blue Canyon	BLC	American	-120.71	39.28	1,609	USBR
Greek Store	GKS	American	-120.56	39.07	1,707	USBR
Robbs Saddle	RBB	American	-120.38	38.91	1,798	SMUD
Robinson Cow Camp	RCC	Yuba	-120.68	39.62	1,975	CA DWR
Huysink	HYS	American	-120.53	39.28	2,012	USBR
Van Vleck	VVL	American	-120.31	38.94	2,042	SMUD
Central Sierra Snow Lab	CSL	Yuba	-120.37	39.33	2,103	NRCS
Silver Lake	SIL	American	-120.12	38.68	2,164	USBR
Forni Ridge	FRN	American	-120.22	38.80	2,282	USBR
Alpha	ALP	American	-120.22	38.80	2,316	SMUD
Caples Lake	CAP	American	-120.04	38.71	2,438	USBR

Schneiders	SCN	American	-120.07	38.75	2,667	SMUD

Table F2 Soil moisture measurements were obtained from a variety of sources, which place sensors at different depths beneath the ground surface.

Station Name	ID	River Basin	Longitude	Latitude	Elevation (m)	Source	Sensor Depths (cm)
Blue Canyon	blu	American	-120.71	39.28	1,604	NOAA	10
Big Bend	bbd	Yuba	-120.52	39.31	1,754	NOAA	10
Chickering American River Reserve	UCCA	American	-120.36	39.25	1,841	WRCC	5
Central Sierra Snow Lab	CSL	Yuba	-120.37	39.33	2,103	NRCS	5, 20, 50
Alpha	ALP	American	-120.22	38.80	2,316	ARHO	30, 60
Schneiders	SCN	American	-120.07	38.75	2,675	ARHO	30, 60

Table F3 Surface meteorological stations, organized by river basin and elevation. Note that while some stations are identical to those in Tables F1 and/or F2, the data sources and native timestep (T, minutes) may differ. Binary flags indicate whether PPT (precipitation), TAIR (air temperature), QAIR (humidity), and WV (wind speed) were used in Chapter 3. Flags marked with "" and "**" indicate a variable was screened from analysis during the 7 January and 6 February storms, respectively.*

Station Name	ID	River Basin	Longitude	Latitude	Elevation (m)	Source	PPT	TAIR	QAIR	WV	T
Mineral	MIN	Sacramento	-121.61	40.35	1511	CDEC	1	0	0	0	30
Rice Canyon	RNYC1	Feather	-120.33	39.53	2,116	RAWS	0	1**	1**	1**	60
Grizzle Ridge	GRZ	Feather	-120.65	39.92	2,103	CDEC	1	0	0	0	60
Jordan Peak	JDP	Feather	-120.29	40.04	2,076	CDEC	0	1	1	1*	60

Harkness Flat	HRK	Feather	-121.28	40.42	1,890	CDEC	0	1	1	0	60
Swain Mountain	SWNC1	Feather	-121.10	40.45	1,859	RAW S	1	1	1	1	60
Lake David	DAV	Feather	-120.47	39.88	1,758	CDEC	0	0	0	0	60
Doyle Crossing	DOY	Feather	-120.48	40.12	1,728	CDEC	0	1	0	1	60
Coyote	CYVC1	Feather	-120.48	39.99	1,698	RAW S	0	1	1	1	60
Thompson Valley	TVL	Feather	-120.48	39.98	1,647	CDEC	0	1	1	1*	60
Westwood	WWD	Feather	-120.90	40.31	1,570	CDEC	0	1	1	1	60
Mohawk / Denten Creek	MWKC 1	Feather	-120.59	39.78	1,561	RAW S	0	1*	1*	1*	60
Plumas Eureka St Park Weather Station	EWS	Feather	-120.70	39.76	1,557	CDEC	1	0	0	0	60
La Porte	LAP	Feather	-120.98	39.68	1,518	CDEC	1	0	0	0	60
Sierraville	SVL	Feather	-120.37	39.58	1,516	CDEC	0	0	0	0	60
Hamilton Branch	HAM	Feather	-121.09	40.27	1,390	CDEC	1	0	0	0	15
Cashman	CSH	Feather	-120.92	40.00	1,378	CDEC	1	1	1	1	60
Pratville (PG&E)	PVL	Feather	-121.16	40.21	1,378	CDEC	0	1*	1*	0	60
Strawberry Valley	SBY	Feather	-121.11	39.56	1,161	CDEC	1	0	0	0	30
Greenville	GRE	Feather	-120.94	40.14	1,085	CDEC	1	0	0	0	15

Brush Creek	BRS	Feather	-121.34	39.69	1,085	CDEC	1	0	0	0	60
Tay Nelson St											
Taylorsville	TAY	Feather	-120.84	40.08	1,079	CDEC	0	1	1	1	60
Stirling City	SRL	Feather	-121.53	39.90	1,073	CDEC	1	0	0	0	30
Quincy Ranger											
District	QYR	Feather	-120.94	39.98	1,067	CDEC	1	1	1	1	60
Quincy	QCY	Feather	-120.95	39.94	1,039	CDEC	1	0	0	0	60
Jarbo Gap	JAR	Feather	-121.49	39.74	823	CDEC	1	1	1	1	60
Central Sierra Snow Lab	CSL	Yuba	-120.37	39.33	2,103	WRCC	0	1	1	0	10
Big Bend	bbd	Yuba	-120.52	39.31	1,754	NOAA	0	1	1	1*	2
Bowman Lake	BOL	Yuba	-120.65	39.45	1,643	CDEC	1	0	0	0	15
Lake Spaulding (PG&E)	LSP	Yuba	-120.63	39.32	1,571	CDEC	1	1*	1*	0	15
Sierra City	SRC	Yuba	-120.65	39.57	1,432	CDEC	1	0	0	0	15
Deer Creek Forebay	DRC	Yuba	-120.83	39.30	1,358	CDEC	0	1	1	0	15
White Cloud	WTC	Yuba	-120.84	39.32	1,317	CDEC	1	1	1	1	60
Pike County	PKC	Yuba	-121.20	39.48	1,132	CDEC	1	1	1	1	60
Downieville	DNV	Yuba	-120.83	39.56	890	CDEC	1	0	0	0	15
Grass Valley	GVY	Yuba	-121.07	39.21	731	CDEC	1	0	0	0	15
Bullards Bar	BUD	Yuba	-121.14	39.40	640	CDEC	1	0	0	0	15

Schneiders	SCN	American	-120.07	38.75	2,675	ARHO	0	1	1	0	15
Mt Lincoln	MTL	American	-120.33	39.29	2,544	ARHO	0	1	1	0	15
Caples Lake	CAP	American	-120.04	38.71	2,439	ARHO	0	1	1	1**	60
Alpha	ALP	American	-120.22	38.80	2,316	ARHO	0	1	1	0	15
Duncan Peak	DPK	American	-120.51	39.15	2,126	ARHO	0	1	1	0	15
Van Vleck	VVL	American	-120.31	38.94	2,042	ARHO	0	1	1	0	15
Dolly Rice	DOR	American	-120.37	39.15	2,006	ARHO	0	1	1	0	15
Chickering American River Reserve	UCCA	American	-120.36	39.25	1,841	WRC C	0	1	1	1*	10
Robbs Saddle	RBB	American	-120.38	38.91	1,816	ARHO	0	1	1	0	15
Talbot Camp	TLC	American	-120.38	39.19	1,741	ARHO	0	1	1	0	15
Sugarloaf	SKBC1	American	-120.31	38.78	1,723	RAW S	0	1*	1*	0	60
Blue Canyon	blu	American	-120.71	39.28	1,604	NOA A	1	1	1	1	2
Bear Trap	BTP	American	-120.58	39.09	1,590	CDEC	0	1	1	1*	60
Bald Mountain	BMT	American	-120.68	38.90	1,426	CDEC	1	1	1	1	60
Hell Hole	HLH	American	-120.42	39.07	1,396	CDEC	1	1	1	1	60
Owens Camp Seed Orchard	OWC	American	-120.25	38.73	1,372	CDEC	0	1*	1*	1*	60
RAWS Near	SOM	American	-120.73	39.09	1,311	CDEC	1	1	1	1	60

Michigan Bluff											
Fresh Pond	FPD	American	-120.54	38.76	1,149	CDEC	1	0	0	0	15
Alta	ata	American	-120.82	39.20	1,048	NOAA	1	1	1	0	2
Placerville Airport	KPVF	American	-120.75	38.72	788	NWS	1	1	1	1	20
Drum Power House	DPH	Bear	-120.77	39.26	1,036	CDEC	0	1	1	0	15
Secret Town	SRT	Bear	-120.88	39.18	829	CDEC	1	1	1	1	60
Bear River at Rollins Reservoir	BRE	Bear	-120.95	39.13	593	CDEC	1	0	0	0	15

Table F4 USGS streamflow gauges used in Chapter 3. "" indicates available 15-minute data.*

Station Name	**USGS ID**	**River Basin**	**Longitude**	**Latitude**	**Drainage Area (km^2)**
Spanish Creek above Blackhawk Creek at Keddie	11402000*	Feather	-120.95	40.00	475
Butt Creek below Almanor-Butt Creek Tunnel near Pratville	11400500	Feather	-121.19	40.19	168
Deer Creek near Smartville	11418500*	Yuba	-121.27	39.22	219
North Yuba River below Goodyears Bar	11413000*	Yuba	-120.94	39.52	648
South Yuba River at Jones Bar near Grass Valley	11417500	Yuba	-121.10	39.29	820

North Fork American River at North Fork Dam	11427000*	American	-121.02	38.94	883
Middle Fork American River above Middle Fork Powerhouse near Foresthill	11427760	American	-120.60	39.03	227
South Fork American River near Kyburz (river only)	11439500	American	-120.33	38.76	500
Rock Creek near Placerville	11444201	American	-120.78	38.79	189

Table F5 NOAA FMCW snow level radars used in Chapter 3. Data are recorded at 10-minute intervals.

Station Name	ID	Longitude	Latitude	Elevation (m)
Oroville	ovl	-121.49	39.53	114
Colfax	cff	-120.94	39.08	644

Appendix G – Meteorological data collection and quality control (Chapter 3)

Hourly (or sub-hourly, if available) measurements of precipitation, air temperature, relative humidity, and wind speed were obtained from a variety of observation networks. These include the California Data Exchange Center (CDEC, http://cdec.water.ca.gov/snow/current/snow/index.html), the Western Regional Climate Center (WRCC, https://wrcc.dri.edu/), MesoWest (https://mesowest.utah.edu/), and the American River Hydrologic Observatory (Bales et al. 2020). We employed the following screening and quality control routine for each variable.

Accumulated precipitation data were collected at native sampling intervals (ranging from 2 minutes to 1 hour). Missing values were imputed for 1-hour gaps or shorter by interpolating across bounding values. Longer gaps were ignored. Incremental precipitation was then calculated via first difference. High-elevation (above ~2,000 m) stations were commonly removed from analysis after visual inspection showed obvious wind effects and/or sticking (i.e., sparse precipitation increments during periods of heavy continuous precipitation at neighboring stations). Negative increments were set to zero, and increments above 25 mm were flagged as missing. Stations missing more than 10% of values during the storms of interest were removed from analysis. The remaining stations were compared to the nearest snow pillow and screened from analysis if total accumulation season (November through March) precipitation fell below 1 April 2017 snow water equivalent. This resulted in a total of 31 suitable gauges (Table F3).

Wind speed, air temperature, and relative humidity data were collected in a similar manner as described above. At temperatures near 0˚C, propeller anemometers can melt and re-freeze the snow that falls on them, stopping the sensor's motion and resulting in an artificially "calm" period. We used a threshold of 6 hours beyond which winds speeds of 0 m s^{-1} winds were

flagged as missing. Wind speeds above 20 m s^{-1} were flagged as missing. Air temperature measurements above 40˚C in absolute value were flagged as missing, while relative humidity values below (above) 0% (100%) were flagged. We interpolated across single-timestep gaps for both variables. We used the cluster medians for ARHO temperature and humidity measurements. Variables with more than 10% values missing during the storms of interest were excluded from analyses on the respective storm, resulting in a total of 41 stations (Table F3).

Appendix H – Synoptic analysis supporting calculations (Chapter 3)

We obtained hourly, 0.25˚ geopotential (Φ, $m^2\ s^{-2}$ or $J\ kg^{-1}$), air temperature (T_{air}, K), specific humidity (q_{air}, $kg\ kg^{-1}$), and zonal (u, $m\ s^{-1}$) and meridional (v, $m\ s^{-1}$) winds at 27 pressure levels (from P_1=1,000 to P_2=100 hPa) from the 5th generation of atmospheric reanalysis from the European Centre for Medium-Range Weather Forecasts (ERA5) (Hersbach et al. 2020). Geopotential heights were obtained by dividing Φ by gravitation acceleration, g ($9.81\ m\ s^{-2}$). We used metrics derived from ERA5 variables to assess synoptic differences between the January and February storm events of interest. Over the study basins, we consider the following metrics:

First, the integrated vapor transport (IVT, $kg\ m^{-1}\ s^{-1}$) was calculated as:

$$IVT = \sqrt{\left(\frac{1}{g}\int_{P_1}^{P_2} q_{air} u\, dP\right)^2 + \left(\frac{1}{g}\int_{P_1}^{P_2} q_{air} v\, dP\right)^2}, \quad Eq\ (H1)$$

Second, integrated heat transport (IHT, $J\ m^{-1}\ s^{-1}$) was calculated as:

$$IHT = \sqrt{\left(\frac{c_P}{g}\int_{P_1}^{P_2} T_{air} u\, dP\right)^2 + \left(\frac{c_P}{g}\int_{P_1}^{P_2} T_{air} v\, dP\right)^2}, \quad Eq\ (H2),$$

where c_P is the specific heat of dry air at constant pressure ($1{,}005\ J\ kg^{-1}\ K^{-1}$).

Lastly, moist static energy (MSE, $J\ kg^{-1}$) was calculated at discrete pressure levels,

$$MSE = c_P\theta + L_v q_{air} + \Phi, \quad Eq\ (H3),$$

where L_v is the latent heat of vaporization (assumed to be constant at $2.5x106\ J\ kg^{-1}$). The potential temperature, θ (K), was calculated as:

$$\theta = T_{air}\left(\frac{P}{P_0}\right)^{-\frac{R_d}{c_P}}, \quad Eq\ (H4),$$

where P_0 is 1,000 hPa and R_d is the dry air gas constant ($287\ J\ kg^{-1}\ K^{-1}$).

Appendix I – Wind correction to test precipitation undercatch (Chapter 3)

We argue that the degree of snowmelt contributing to the exceptional runoff from the February storm event was lower than previously reported. A prior study quantified the relative increase in terrestrial water input (TWI) during rain-on-snow from snowmelt as the ratio of snowmelt to rainfall (Henn et al. 2020). They used 4-km, 6-hourly precipitation from the California Nevada River Forecast Center (CNRFC), which is a topographically-corrected mosaic of gauge observations. While gauge undercatch can occur in exposed, windy areas, the CNRFC product does not apply a wind correction. Any wind-induced biases in the product would be baked into this estimate of snowmelt augmenting TWI and can conceivably inflate it. We considered this possibility as part of our argument by using hourly ERA5-Land (Muñoz Sabater 2019) wind vectors to correct CNRFC precipitation. We resampled CNRFC to hourly values with uniform scaling and mapped the 0.1˚ ERA5-Land wind vectors to the CNRFC grid via nearest neighbor. We applied a simple correction scheme from Masuda et al. (2019) assuming a gauge height of 2 m, anemometer height of 10 m, and the correction coefficient for a heated tipping bucket gauge experiencing rainfall (their Table 2 and Equations 1 and 2). For both the January and February events over the Feather River basin, we report the ratio of corrected- to accumulated precipitation totals for various roughness lengths. It should be noted that increases to wind-corrected precipitation is likely low because (1) reanalyzed winds can underestimate true wind patterns in mountainous areas from smoothing over complex terrain, and (2) the highest elevations in the basins may have experienced snowfall, which would require a more aggressive correction (Masuda et al. 2019).

Appendix J – Station metadata (Chapter 4)

Table J1 USGS stream gauges used in Chapter 4. Snow pillows were assigned by proximity to the drainage boundary (within ~10 km).

USGS ID	Station Name	HUC 8	Latitude	Longitude	Drainage Area (km2)	Nearby snow pillows
11381500	Mill Creek near Los Molinos	18020156	40.05	-122.02	338	LLP, HRK, HMB
11402000	Spanish Creek near Blackhawk Creek At Keddie	18020122	40.00	-120.95	475	GRZ, PLP, BKL, FOR, KTL, RTL
11413000	North Yuba R below Goodyears Bar	18020125	39.52	-120.94	648	RCC, GOL, MDW, INN, IDP, IDC
11427000	North Fork American R at North Fork Dam	18020128	38.94	-121.02	883	BLC/blu, HYS, CSL, SQV, GKS, TK2, TCC, WC3
11274790	Tuolumne R at Grand Canyon of Tuolumne above Hetch Hetchy	18040009	37.92	-119.66	776	SLI, TUM, DAN, WHW, PDS, VRG
11266500	Merced Creek near Pohono Bridge near Yosemite	18040008	37.72	-119.67	833	STR, TNY, GIN, GEM, AGP

Table J2 Snow pillows and co-located soil sensors used in Chapter 4. Note that station ID varies by source, and some locations have multiple. Multiple IDs signify the source of soil moisture measurements, if available. Snow variables were all obtained from CDEC. Also note that soil sensor depths vary by station.

Name	ID (CDEC / NRCS / NOAA / WRCC)	Longitude	Latitude	Elevation (m)	Soil Probe Depth(s) (cm)
Alta	- / - /ata / -	-120.82	39.20	1,048	10, 15
Agnew Pass	AGP/ - / - / -	-119.14	37.72	2,880	
Big Bend	- / - /bbd/ -	-120.52	39.31	1,754	10, 15
Blue Canyon	BLC/ - / blu / -	-120.71	39.28	1,609	10, 15
Bucks Lake	BKL/ - / - / -	-121.25	39.85	1,753	
Central Sierra Snow Lab	CSL/428/ - / -	-120.37	39.33	2,103	5, 20, 50
Chickering American R. Reserve	- / - / - /UCCA	-120.36	39.25	1,841	5
Dana Meadows	DAN/ - / - / -	-119.26	37.90	2,987	
Four Trees	FOR/ - / - / -	-121.32	39.81	1,570	

Gem Pass	GEM/ - / - / -	-119.17	37.78	3,276	
Gin Flat	GIN/ - / - / -	-119.77	37.77	2,149	
Gold Lake	GOL/ - / - / -	-120.62	39.67	2,057	
Greek Store	GKS/ - / - / -	-120.56	39.07	1,707	
Grizzly Ridge	GRZ/ - / - / -	-120.64	39.92	2,103	
Harkness Flat	HRK/ - / - / -	-121.28	40.42	1,890	
Humbug	HMB/ - / - / -	-121.38	40.12	1,981	
Huysink	HYS/ - / - / -	-120.53	39.28	2,012	
Independence Camp	IDC/539/ - / -	-120.30	39.45	2,133	5, 20, 50
Independence Creek	INN/540/ - / -	-120.29	39.49	1,981	5, 20, 50
Independence Lake	IDP/541/ - / -	-120.32	39.44	2,575	5, 20, 50
Kettle Rock	KTL/ - / - / -	-120.72	40.14	2,225	

Lower Lassen Peak	LLP/ - / - / -	-121.51	40.47	2,514	
Meadow Lake	MDW/ - / - / -	-120.51	39.41	2,194	
Ostrander Lake	STR/ - / - / -	-119.55	37.64	2,499	
Paradise Meadow	PDS/ - / - / -	-119.67	38.05	2,332	
Pilot Peak	PLP/ - / - / -	-120.88	39.79	2,073	
Rattlesnake	RTL/ - / - / -	-121.04	40.13	1,859	
Robinson Cow Camp	RCC/ - / - / -	-120.68	39.62	1,975	
Slide Canyon	SLI/ - / - / -	-119.43	38.09	2,804	
Palisades Tahoe	SQV/784/ - / -	-120.28	39.19	2,499	5, 20, 50
Tahoe City Cross	TCC/809/ - / -	-120.15	39.17	2,057	5, 20, 50
Tenaya Lake	TNY/ - / - / -	-119.45	37.84	2,484	5, 10, 25
Truckee #2	TK2/834/ - / -	-120.18	39.30	1,951	5, 20, 50

Tuolumne Meadows	TUM/ - / - / -	-119.35	37.88	2,621	5, 10, 25
Virginia Lakes Ridge	VRG/846/ - / -	-119.23	38.08	2,835	5, 20, 50
Ward Creek #3	WC3/848/ - / -	-120.22	39.14	2,057	5, 20, 50
White Wolf	WHW/ - / - / -	-119.65	37.86	2,408	

Table J3 NOAA FMCW snow level radars used in Chapter 4. Data are recorded at 10-minute intervals.

Station Name	**ID**	**Longitude**	**Latitude**	**Elevation (m)**
Oroville	ovl	-121.49	39.53	114
Colfax	cff	-120.94	39.08	644
New Exchequer Dam	ner	-120.28	37.60	25

Appendix K – Regression results for brightband and melt altitude (Chapter 4)

Table K1 Ordinary least squares regression results for gap-filling hourly brightband heights with ERA5-Land 0˚C altitude for water years 2017-2019. Listed are sample size (n), adjusted R^2, and standard error (SE) in meters.

Radar	**WY 2017**	**WY 2018**	**WY 2019**
Oroville	n=388 R^2=0.87 SE=0.017	n=372 R^2=0.84 SE=0.019	n=460 R^2=0.88 SE=0.015
Colfax	n=417 R^2=0.90 SE=0.016	n=390 R^2=0.91 SE=0.016	n=484 R^2=0.87 SE=0.017
New Exchequer Dam	n=303 R^2=0.94 SE=0.014	n=292 R^2=0.91 0.016	n=297 R^2=0.75 SE=0.023

Appendix L – Time of concentration calculation (Chapter 4)

To inform a timescale on which to consider rainfall events as separate, we use the NRCS National Engineering Handbook's watershed lag method to estimate watershed concentration times (NRCS 2004). We use equations 15-4b and 15-5 to estimate concentration time as a function of watershed average slope and area at various potential retention values (i.e., curve number). Concentration times for high-retention (low curve number) landscapes are on the order of one day (Figure L1). This informed our value of 30 hours (5 Stage IV timesteps) to consider the tendency for montane forest environments to have longer concentration times than what may be reliably calculated by this method (Loukas and Quick 1996).

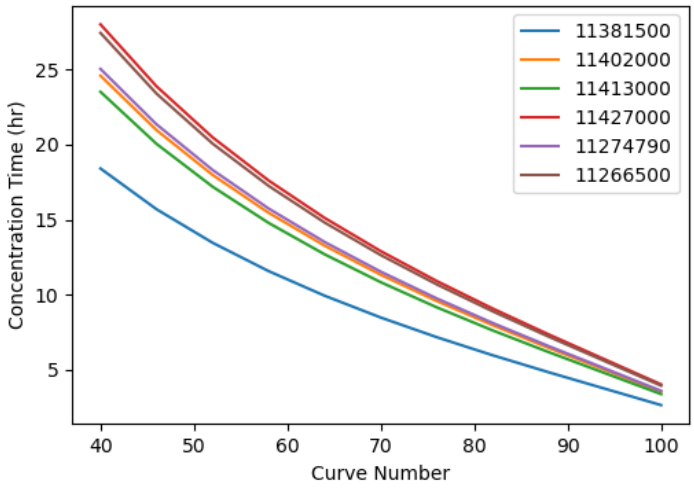

Figure L1 Watershed concentration time estimates for study basins in Figure 4.1a, calculated using the NRCS National Engineering Handbook watershed lag method.

Appendix M – Sensitivity in defining large versus minor rain-on-snow (Chapter 4)

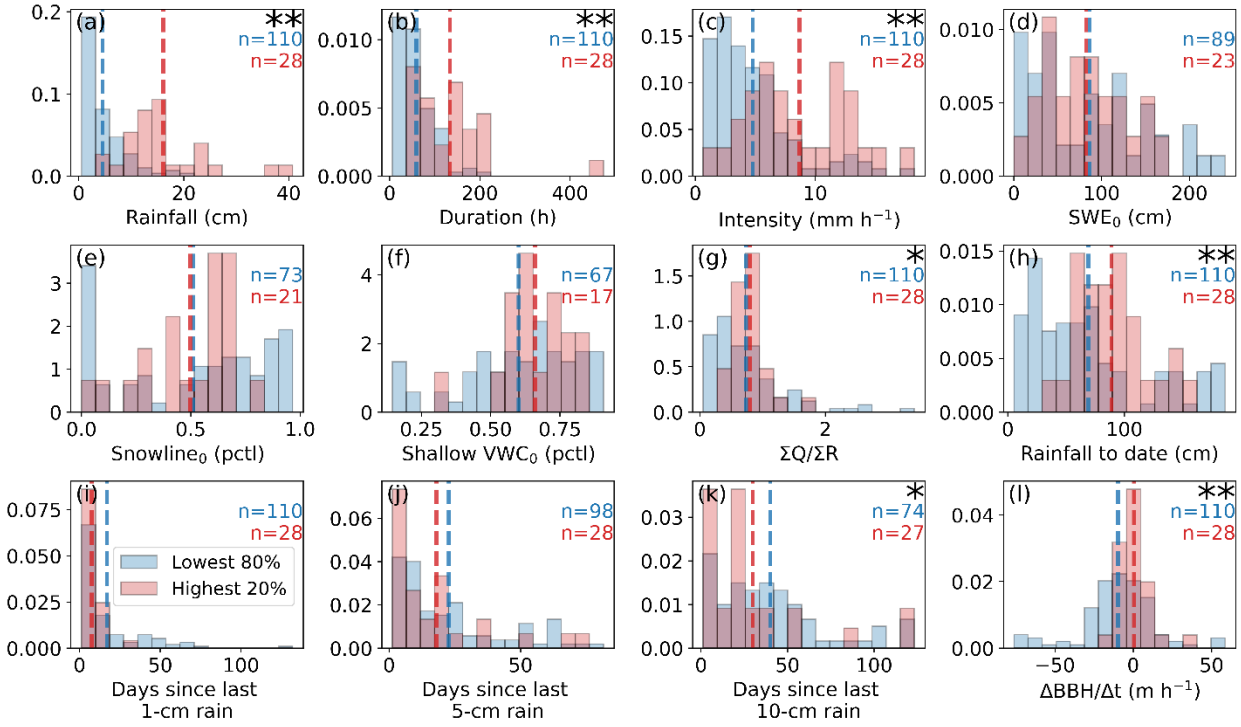

Figure M1 Same as Figure 4.6, but for ROS events that generate the 20% highest and 80% lowest runoff volumes.

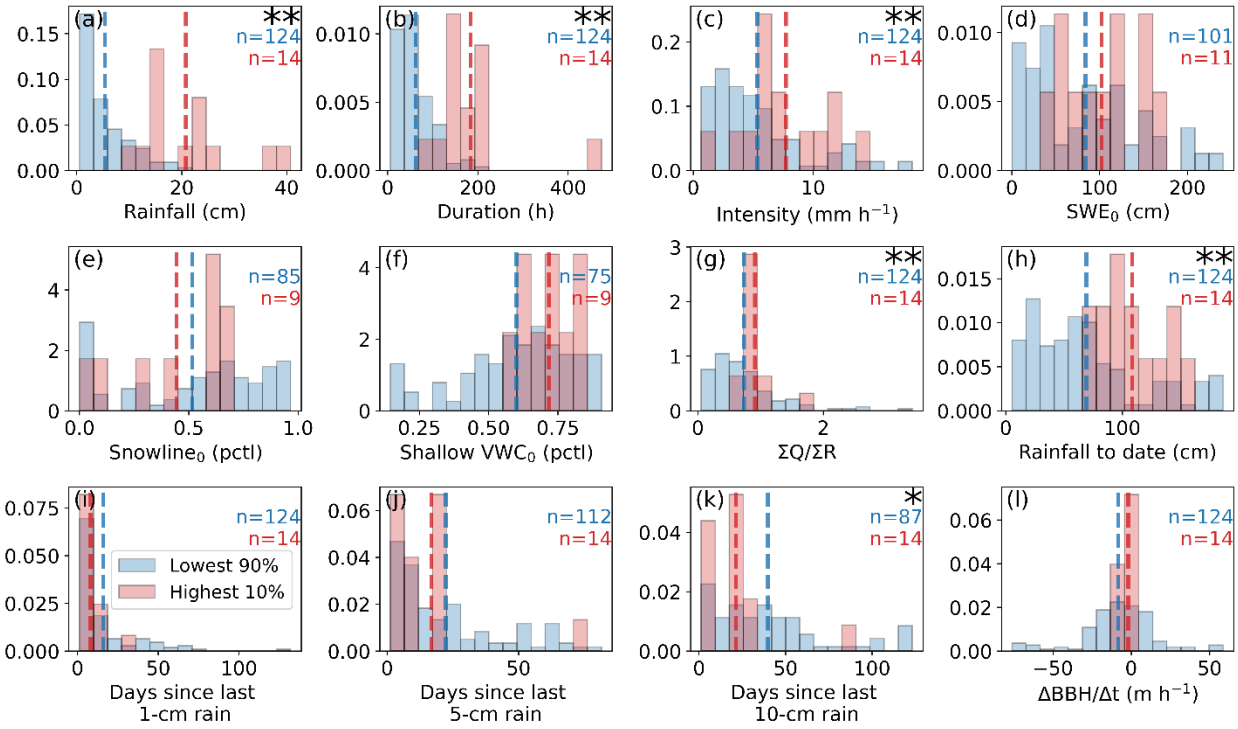

Figure M2 Same as Figure 4.6, but for ROS events that generate the 10% highest and 90% lowest runoff volumes.

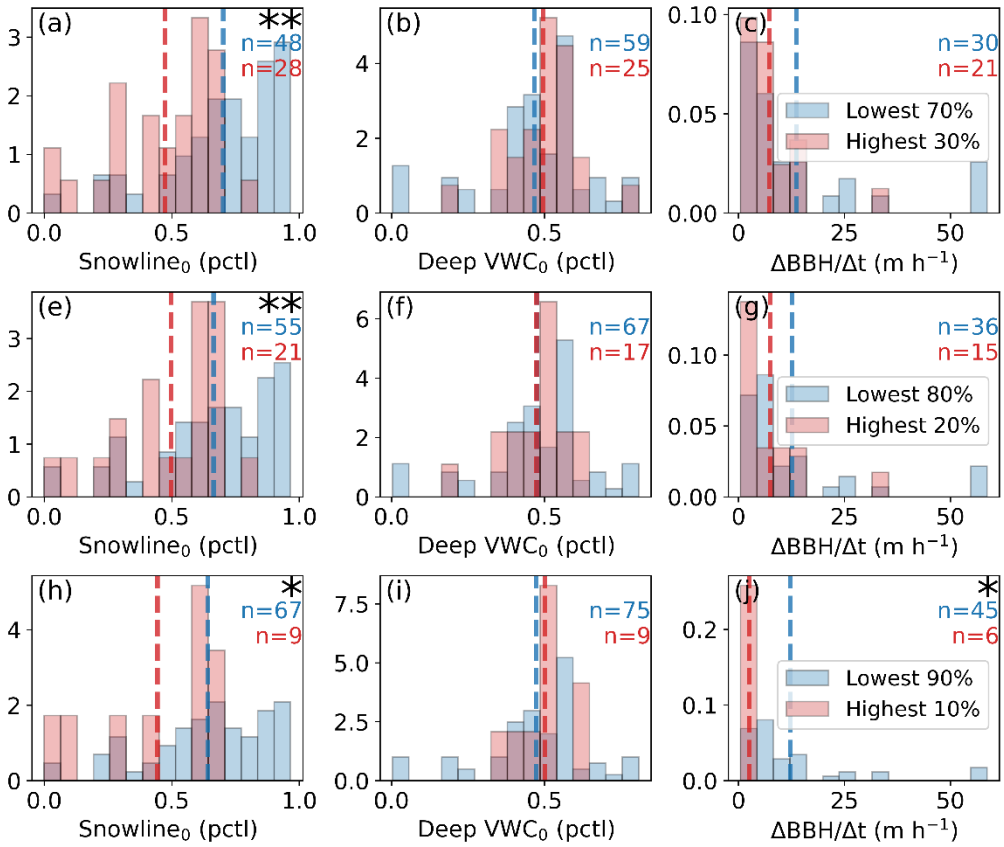

Figure M3 Density histograms comparing attributes of large versus minor ROS events in terms of generated runoff in WYs 2017-2019. Sample sizes are annotated beneath indicators of statistically significant differences between distributions using the Mann-Whitney U test ("" and "**" indicate significance at α=0.05 and α=0.01 levels, respectively). Rows represent different thresholds separating distributions: (top row) highest 30% of runoff from ROS events versus the lowest 70%; (center row) 20%-80%; and (bottom row) 10%-90%. Pre-event snowline elevations (a, e, h; expressed as quantiles of watershed elevation) are shown for the four northernmost watersheds in Figure 4.1a to remove the effect of complete snow cover in the Tuolumne and Merced River headwater basins on the distributions of pre-event snowlines. Initial deep (below 10 cm) soil moisture (b, f, i; expressed as quantiles of WY 2017-2019 deep soil moisture) show insignificant differences across large and minor events. Non-negative regression slopes of in-storm BBH (c, g, j) are mostly insignificant.*

Appendix N – Sensitivity in snow level bending in partitioning precipitation (Chapter 4)

A sensitivity analysis of Chapter 4 is presented here. The tendency of upwind snow levels to bend downward toward the mountain side is a climatological feature (Minder and Kingsmill 2013) and presents an uncertainty in our approach to partitioning precipitation into rain and snow using BBHs (Lundquist et al. 2008). Results presented here pertain to Chapter 4 Table 1, Figure 4.4, Figure 4.6, and Figures M1-M3, but for a systematic BBH lowering of 200 m (based conservatively on the 170-m average of Minder and Kingsmill 2013) when cataloguing rainfall and ROS events and their resulting statistics.

The number of rainfall and ROS events are reduced by 37 and 7, respectively (Table N1), yielding 273 and 131 ROS events for a 200-m lower BBH.

Table N1 Number of rainfall and ROS events (as in Table 4.1) when partitioning precipitation based on BBH lowering of 200 m.

USGS ID	**Station Name Abbr**	**# rain (ROS) events**		
		WY 2017	**WY 2018**	**WY 2019**
11381500	Mill C	23 (13)	20 (9)	21 (7)
11402000	Spanish C	17 (8)	13 (5)	23 (7)
11413000	N Yuba	21 (11)	13 (5)	24 (10)
11427000	NF American	22 (13)	15 (8)	26 (16)
11274790	Tuolumne	9 (6)	5 (2)	3 (1)
11266500	Merced	11 (6)	4 (3)	3 (1)

This lowering by construct resulted in inflated ratios of streamflow to rainfall (QR), creating more “hyperactive” watershed responses to ROS (Figure N1 versus Chapter 4 Figure 4.4). This does not change the notion that storm event clusters augment runoff efficiency.

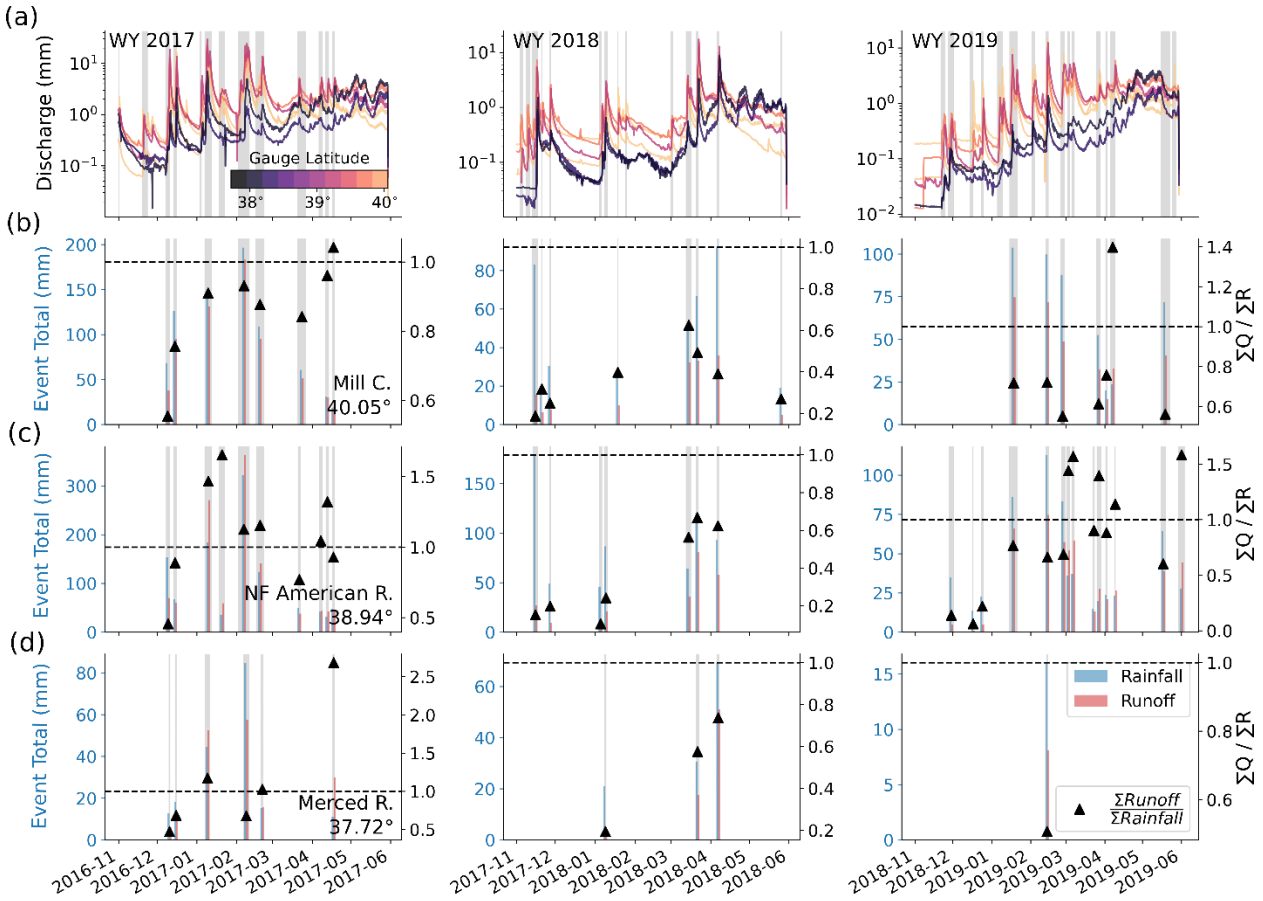

Figure N1 (a) Natural log of 6-hourly streamflow for WYs 2017-2019 at each stream gauge in Figure 4.1a. For select gauges in the (b) northernmost (Mill Creek), (c) central (North Fork American River), and (d) southernmost (Merced River) regions in this study, ratios of total event streamflow to rainfall are plotted for each ROS event. Events are shown based on a BBH lowering of 200 m.

The distribution of large versus small ROS events and tests for statistical significance between them remain largely unchanged with systematic BBH lowering. The volume, duration, and intensity of rainfall, QR, BBH slope, rainfall to date, and the number of days since a large (100 mm) rainfall event all produce a significant difference between large versus minor ROS events (Figure N2 versus Figure 4.6). These are mostly robust against the threshold separating large from minor ROS events (Figures N3, N4). Similarly, initial SWE, shallow soil moisture, and snowline elevations show minor differences across large versus minor ROS events, as does the number of days since small ($\leq$ 50 mm) rainfall events (Figure N2-N4). Removing the initial snowlines from the Tuolumne and Merced River basins produces the same

result for a lowered BBH (Figure N5 versus Figure M3). Conclusions do not change for deep initial soil moisture and for non-negative BBH slopes (Figure N5).

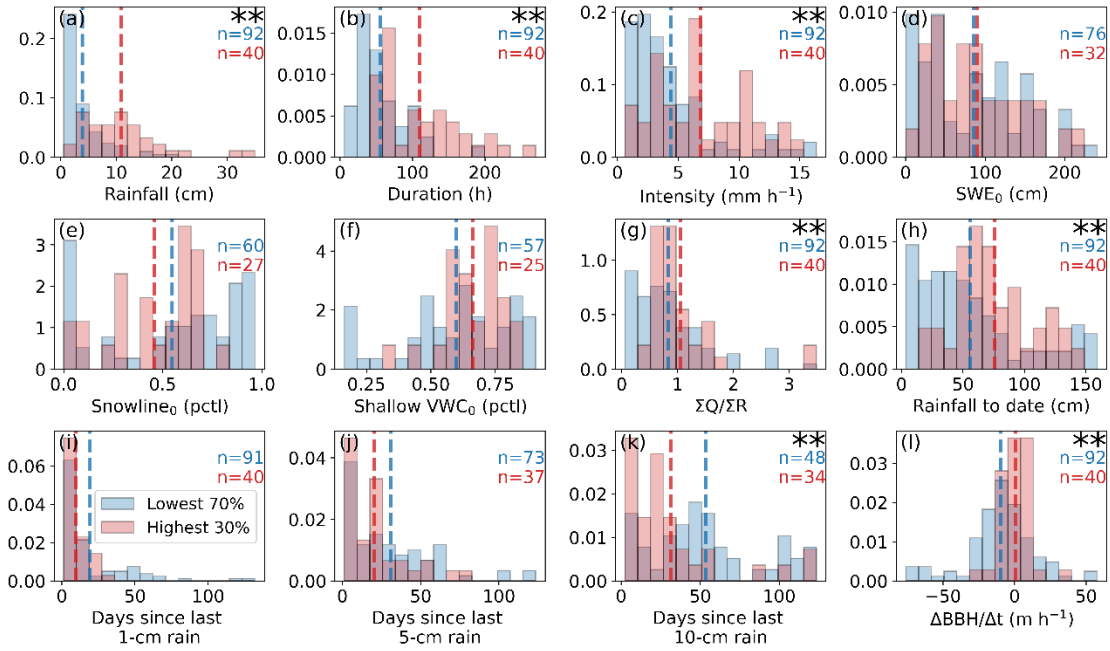

Figure N2 Same as Figure 4.6, but for a systematic 200-m lowering of BBH to partition precipitation.

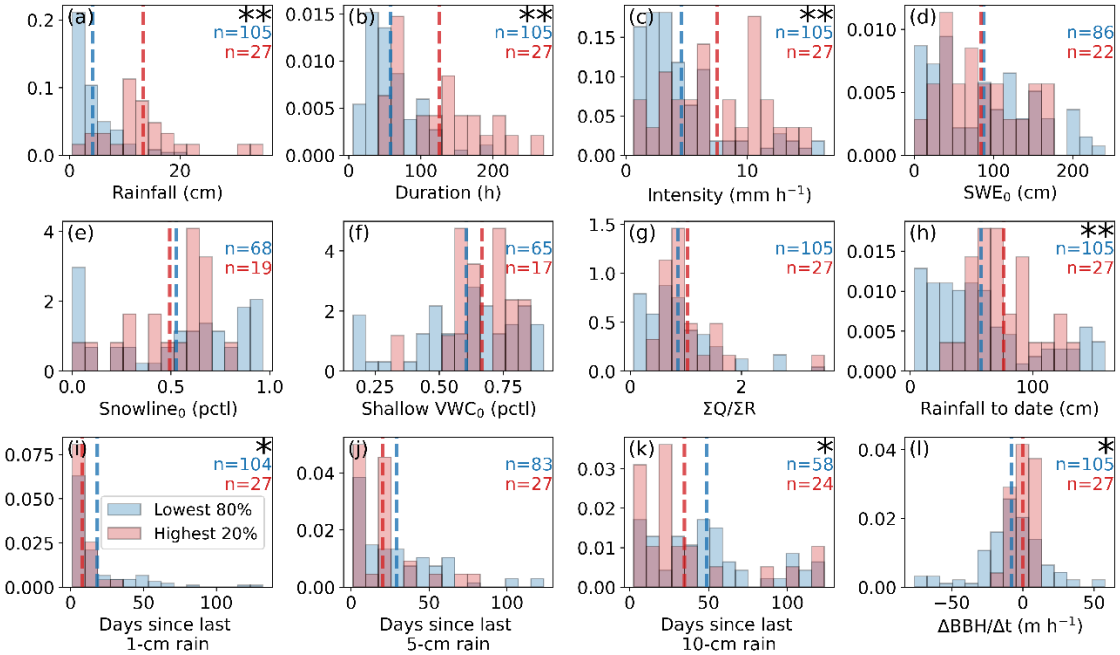

Figure N3 Same as Figure N2, but for ROS events that generate the 20% highest and 80% lowest runoff volumes.

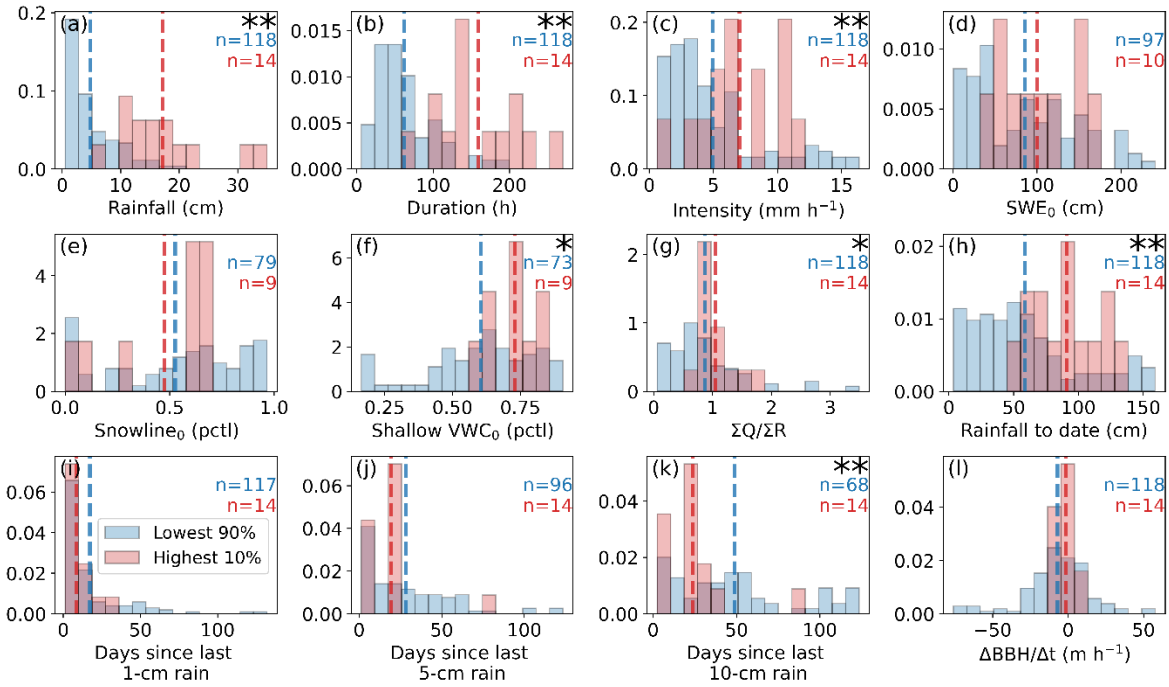

Figure N4 Same as Figure N2, but for ROS events that generate the 10% highest and 90% lowest runoff volumes.

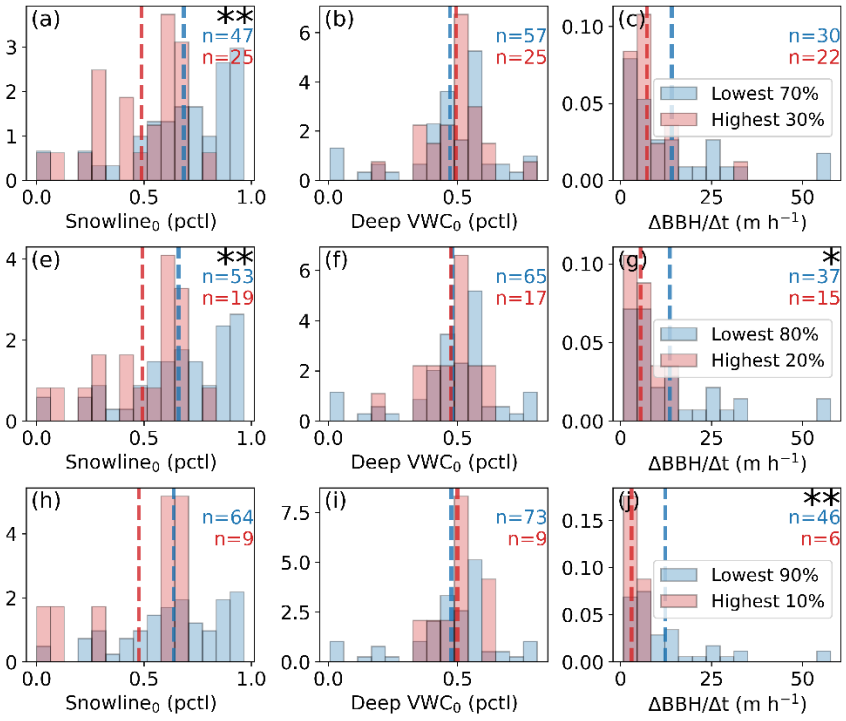

Figure N5 Same as Figure M3, but for a systematic 200-m lowering of BBH to partition precipitation.

References

Albano, C. M., M. D. Dettinger, and A. A. Harpold, 2020: Patterns and Drivers of Atmospheric River Precipitation and Hydrologic Impacts across the Western United States. *Journal of Hydrometeorology*, **21**, 143–159, https://doi.org/10.1175/JHM-D-19-0119.1.

Andreadis, K. M., P. Storck, and D. P. Lettenmaier, 2009: Modeling snow accumulation and ablation processes in forested environments. *Water Resources Research*, **45**, 1–13, https://doi.org/10.1029/2008WR007042.

Arienzo, M. M., M. Collins, and K. S. Jennings, 2021: Enhancing Engagement of Citizen Scientists to Monitor Precipitation Phase. *Frontiers in Earth Science*, **9**, 68, https://doi.org/10.3389/feart.2021.617594.

Avanzi, F., C. De Michele, A. Ghezzi, C. Jommi, and M. Pepe, 2014: A processing-modeling routine to use SNOTEL hourly data in snowpack dynamic models. *Advances in Water Resources*, **73**, 16–29, https://doi.org/10.1016/j.advwatres.2014.06.011.

Bair, E. H., R. E. Davis, and J. Dozier, 2018: Hourly mass and snow energy balance measurements from Mammoth Mountain, CA USA, 2011 – 2017. *Earth System Science Data*, **10**, 549–563, https://doi.org/10.5194/essd-10-549-2018.

Bales, R. C., N. P. Molotch, T. H. Painter, M. D. Dettinger, R. Rice, and J. Dozier, 2006: Mountain hydrology of the western United States. *Water Resources Research*, **42**, W08432, https://doi.org/10.1029/2005WR004387.

——, R. Rice, and S. B. Roy, 2015: Estimated loss of snowpack storage in the Eastern Sierra Nevada with climate warming. *Journal of Water Resources Planning and Management*, **141**, 04014055, https://doi.org/10.1061/(ASCE)WR.1943-5452.0000453.

——, G. Cui, R. Rice, X. Meng, Z. Zhang, P. Hartsough, S. D. Glaser, and M. H. Conklin, 2020:

Snow depth, air temperature, humidity, soil moisture and temperature, and solar radiation data from the basin-scale wireless-sensor network in American River Hydrologic Observatory (ARHO) (Accessed on 10-Apr-2021). https://doi.org/10.6071/M39Q2V.

Barros, A. P., and P. Lettenmaier, 1994: Dynamic Modeling of Orographically Induced Precipitation. *Reviews of Geophysics*, **32**, 265–284, https://doi.org/10.1029/94RG00625.

Bartelt, P., and M. Lehning, 2002: A physical SNOWPACK model for the Swiss avalanche warning Part I : numerical model. *Cold Regions Science and Technology*, **35**, 123–145, https://doi.org/10.1016/S0165-232X(02)00074-5.

Bartos, M. D., and M. V Chester, 2015: Impacts of climate change on electric power supply in the Western United States. *Nature Climate Change*, **5**, 748–752, https://doi.org/10.1038/NCLIMATE2648.

Berghuijs, W. R., R. A. Woods, C. J. Hutton, and M. Sivapalan, 2016: Dominant flood generating mechanisms across the United States. *Geophysical Research Letters*, **43**, 4382–4390, https://doi.org/10.1002/2016GL068070.

Bergman, J. A., 1983: Hydrologic Response of Central Sierra Nevada Snowpacks to Rainfall. *Western Snow Conference 1983*, 141–144.

Berris, S. N., and R. D. Harr, 1987: Comparative snow accumulation and melt during rainfall in forested and clear-cut plots in the Western Cascades of Oregon. *Water Resources Research*, **23**, 135–142, https://doi.org/10.1029/WR023i001p00135.

Bonnell, R., D. Mcgrath, K. Williams, R. Webb, S. R. Fassnacht, and H. Marshall, 2021: Spatiotemporal Variations in Liquid Water Content in a Seasonal Snowpack: Implications for Radar Remote Sensing. *Remote Sensing*, **13**, 4223, https://doi.org/10.3390/rs13214223.

Boxall, B., 2017: Gov. Brown declares California drought emergency is over. *Los Angeles*

Times, April 7.

Brandt, W. T., K. J. Bormann, F. Cannon, J. S. Deems, T. H. Painter, D. F. Steinhoff, and J. Dozier, 2020: Quantifying the Spatial Variability of a Snowstorm Using Differential Airborne Lidar. *Water Resources Research*, **56**, e2019WR025331, https://doi.org/10.1029/2019WR025331.

——, K. Haleakala, B. J. Hatchett, and M. Pan, 2022: A Review of the Hydrologic Response Mechanisms During Mountain Rain-on-Snow. *Frontiers in Earth Science*, **10**, 791760, https://doi.org/10.3389/feart.2022.791760.

Braun, S. A., and R. A. Houze, 1995: Melting and freezing in a mesoscale convective system. *Quarterly Journal of the Royal Meteorological Society*, **121**, 55–77, https://doi.org/10.1002/qj.49712152104.

Capelli, A., F. Koch, P. Henkel, M. Lamm, F. Appel, C. Marty, and J. Schweizer, 2022: GNSS signal-based snow water equivalent determination for different snowpack conditions along a steep elevation gradient. *The Cryosphere*, **16**, 505–531, https://doi.org/10.5194/tc-16-505-2022.

Chang, E. K. M., C. Zheng, P. Lanigan, A. M. W. Yau, and D. J. Neelin, 2015: Significant modulation of variability and projected change in California winter precipitation by extratropical cyclone activity. *Geophysical Research Letters*, **42**, 5983–5991, https://doi.org/10.1002/2015GL064424.

Choi, J., J. Lu, S.-W. Son, D. M. W. Frierson, and J.-H. Yoon, 2016: Uncertainty in future projections of the North Pacific subtropical high and its implication for California winter precipitation change. *Journal of Geophysical Research: Atmospheres*, **121**, 795–806, https://doi.org/10.1002/2015JD023858.

Colbeck, S. C., 1975a: A theory for water flow through a layered snowpack. *Water Resources Research*, **11**, 261–266, https://doi.org/10.1029/WR011i002p00261.

Colbeck, S. G., 1975b: *Analysis of hydrologic response to rain-on-snow*. 1–13 pp. https://hdl.handle.net/11681/5886.

Conway, H., and R. Benedict, 1994: Infiltration of water into snow. *Water Resources Research*, **30**, 641–649, https://doi.org/https://doi.org/10.1029/93WR03247.

Corringham, T. W., F. Martin Ralph, A. Gershunov, D. R. Cayan, and C. A. Talbot, 2019: Atmospheric rivers drive flood damages in the western United States. *Science Advances*, **5**, eaax4631, https://doi.org/10.1126/sciadv.aax4631.

Dettinger, M. D., D. R. Cayan, M. K. Meyer, and A. E. Jeton, 2004a: Simulated hydrologic responses to climate variations and change in the Merced, Carson, and American River basins, Sierra Nevada, California, 1900–2099. *Climatic Change*, **62**, 283–317, https://doi.org/10.1023/B:CLIM.0000013683.13346.4f.

——, K. Redmond, and D. Cayan, 2004b: Winter orographic precipitation ratios in the Sierra Nevada - Large-scale atmospheric circulations and hydrologic consequences. *Journal of Hydrometeorology*, **5**, 1102–1116, https://doi.org/10.1175/JHM-390.1.

DeWalle, D. R., and A. Rango, 2008: *Principles of Snow Hydrology*. 1st ed. Cambridge University Press, New York,.

Donahue, C., S. M. Skiles, and K. Hammonds, 2022: Mapping liquid water content in snow at the millimeter scale: an intercomparison of mixed-phase optical property models using hyperspectral imaging and in situ measurements. *The Cryosphere*, **16**, 43–59, https://doi.org/10.5194/tc-16-43-2022.

Dozier, J., T. H. Painter, K. Rittger, and J. E. Frew, 2008: Time-space continuity of daily maps

of fractional snow cover and albedo from MODIS. *Advances in Water Resources*, **31**, 1515–1526, https://doi.org/10.1016/j.advwatres.2008.08.011.

Du, J., 2011: NCEP/EMC 4KM Gridded Data (GRIB) Stage IV Data. Version 1.0. UCAR/NCAR - Earth Observing Laboratory (Accessed 22 Mar 2022). https://doi.org/10.5065/D6PG1QDD.

Dudley, R. W., G. A. Hodgkins, M. R. McHale, M. J. Kolian, and B. Renard, 2017: Trends in snowmelt-related streamflow timing in the conterminous United States. *Journal of Hydrology*, **547**, 208–211, https://doi.org/10.1016/j.jhydrol.2017.01.051.

Ecklund, W. L., C. R. Williams, P. E. Johnston, and K. S. Gage, 1999: A 3-GHz Profiler for Precipitating Cloud Studies. *Journal of Atmospheric and Oceanic Technology*, **16**, 309–322, https://doi.org/10.1175/1520-0426(1999)016<0309:AGPFPC>2.0.CO;2.

Eiriksson, D., and Coauthors, 2013: An evaluation of the hydrologic relevance of lateral flow in snow at hillslope and catchment scales. *Hydrological Processes*, **27**, 640–654, https://doi.org/10.1002/hyp.9666.

Eldardiry, H., A. Mahmood, X. Chen, F. Hossain, B. Nijssen, and D. P. Lettenmaier, 2019: Atmospheric river-induced precipitation and snowpack during the western United States cold season. *Journal of Hydrometeorology*, **20**, 613–630, https://doi.org/10.1175/JHM-D-18-0228.1.

Feng, S., and Q. Hu, 2007: Changes in winter snowfall/precipitation ratio in the contiguous United States. *Journal of Geophysical Research: Atmospheres*, **112**, D15109, https://doi.org/10.1029/2007JD008397.

Fish, M. A., A. M. Wilson, and F. M. Ralph, 2019: Atmospheric River Families: Definition and Associated Synoptic Conditions. *Journal of Hydrometeorology*, **20**, 2091–2108,

https://doi.org/10.1175/JHM-D-18-0217.1.

Fritze, H., I. T. Stewart, and E. Pebesma, 2011: Shifts in Western North American Snowmelt Runoff Regimes for the Recent Warm Decades. *Journal of Hydrometeorology*, **12**, 989–1006, https://doi.org/10.1175/2011JHM1360.1.

Fyfe, J. C., and Coauthors, 2017: Large near-term projected snowpack loss over the western United States. *Nature Communications*, **8**, 14996, https://doi.org/10.1038/ncomms14996.

Garcia, D., 2010: Robust smoothing of gridded data in one and higher dimensions with missing values. *Computational Statistics and Data Analysis*, **54**, 1167–1178, https://doi.org/10.1016/j.csda.2009.09.020.

Garvelmann, J., and M. Weiler, 2014: Variability of Observed Energy Fluxes during Rain-on-Snow and Clear Sky Snowmelt in a Midlatitude Mountain Environment. *Journal of Hydrometeorology*, **15**, 1220–1237, https://doi.org/10.1175/JHM-D-13-0187.1.

——, S. Pohl, and M. Weiler, 2015: Spatio-temporal controls of snowmelt and runoff generation during rain-on-snow events in a mid-latitude mountain catchment. *Hydrological Processes*, **29**, 3649–3664, https://doi.org/10.1002/hyp.10460.

Gershunov, A., and Coauthors, 2019: Precipitation regime change in Western North America: The role of Atmospheric Rivers. *Scientific Reports*, **9**, 9944, https://doi.org/10.1038/s41598-019-46169-w.

Goldenson, N., L. R. Leung, C. M. Bitz, and E. Blanchard-Wrigglesworth, 2018: Influence of atmospheric rivers on mountain snowpack in the western United States. *Journal of Climate*, **31**, 9921–9940, https://doi.org/10.1175/JCLI-D-18-0268.1.

Guan, B., N. P. Molotch, D. E. Waliser, E. J. Fetzer, and P. J. Neiman, 2010: Extreme snowfall events linked to atmospheric rivers and surface air temperature via satellite measurements.

Geophysical Research Letters, **37**, L20401, https://doi.org/10.1029/2010GL044696.

——, ——, ——, E. J. Fetzer, and P. J. Neiman, 2013: The 2010/2011 snow season in California's Sierra Nevada: Role of atmospheric rivers and modes of large-scale variability. *Water Resources Research*, **49**, 6731–6743, https://doi.org/10.1002/wrcr.20537.

——, D. E. Waliser, F. M. Ralph, E. J. Fetzer, and P. J. Neiman, 2016: Hydrometeorological characteristics of rain-on-snow events associated with atmospheric rivers. *Geophysical Research Letters*, **43**, 2964–2973, https://doi.org/10.1002/2016GL067978.

Haasnoot, M., H. Middelkoop, E. van Beek, and W. P. A. van Deursen, 2011: A method to develop management strategies for an uncertain future. *Sustainable Development*, **19**, 369–381, https://doi.org/10.1002/sd.438.

Haleakala, K., M. Gebremichael, J. Dozier, and D. P. Lettenmaier, 2021: Factors Governing Winter Snow Accumulation and Ablation Susceptibility Across the Sierra Nevada (United States). *Journal of Hydrometeorology*, **22**, 1455–1472, https://doi.org/10.1175/jhm-d-20-0257.1.

Hamlet, A. F., and D. P. Lettenmaier, 2005: Production of Temporally Consistent Gridded Precipitation and Temperature Fields for the Continental United States. *Journal of Hydrometeorology*, **6**, 330–336, https://doi.org/10.1175/JHM420.1.

Hammond, J. C., and S. K. Kampf, 2020: Subannual Streamflow Responses to Rainfall and Snowmelt Inputs in Snow - Dominated Watersheds of the Western United States. *Water Resources Research*, **56**, e2019WR026132, https://doi.org/10.1029/2019WR026132.

Harpold, A. A., 2016: Diverging sensitivity of soil water stress to changing snowmelt timing in the Western U.S. *Advances in Water Resources*, **92**, 116–129, https://doi.org/10.1016/j.advwatres.2016.03.017.

——, and P. D. Brooks, 2018: Humidity determines snowpack ablation under a warming climate. *Proceedings of the National Academy of Sciences of the United States of America*, **115**, 1215–1220, https://doi.org/10.1073/pnas.1716789115.

——, M. L. Kaplan, P. Zion Klos, T. Link, J. P. McNamara, S. Rajagopal, R. Schumer, and C. M. Steele, 2017a: Rain or snow: Hydrologic processes, observations, prediction, and research needs. *Hydrology and Earth System Sciences*, **21**, 1–22, https://doi.org/10.5194/hess-21-1-2017.

——, S. Rajagopal, J. B. Crews, T. Winchell, and R. Schumer, 2017b: Relative Humidity Has Uneven Effects on Shifts From Snow to Rain Over the Western U.S. *Geophysical Research Letters*, **44**, 9742–9750, https://doi.org/10.1002/2017GL075046.

Harr, R. D., 1986: Effects of Clearcutting on Rain-on-Snow Runoff in Western Oregon: A New Look at Old Studies. *Water Resources Research*, **22**, 1095–1100, https://doi.org/10.1029/WR022i007p01095.

Harrison, H. N., J. C. Hammond, S. Kampf, and L. Kiewiet, 2021: On the hydrological difference between catchments above and below the intermittent-persistent snow transition. *Hydrological Processes*, **35**, e14411, https://doi.org/10.1002/hyp.14411.

Hatchett, B. J., 2018: Snow level characteristics and impacts of a spring typhoon-originating atmospheric river in the Sierra Nevada, USA. *Atmosphere*, **9**, 233, https://doi.org/10.3390/atmos9060233.

——, 2021: Seasonal and Ephemeral Snowpacks of the Conterminous United States. *Hydrology*, **8**, 32, https://doi.org/10.3390/hydrology8010032.

——, D. P. Boyle, A. E. Putnam, and S. D. Bassett, 2015: Placing the 2012-2015 California-Nevada drought into a paleoclimatic context: Insights from Walker Lake, California-

Nevada, USA. *Geophysical Research Letters*, **42**, 8632–8640, https://doi.org/10.1002/2015GL065841.

——, M. L. Kaplan, and S. Burak, 2016: Some characteristics of upside-down storms in the Northern Sierra Nevada, California-Nevada, USA. *International Snow Science Workshop*, Breckenridge, Colorado, 1165–1172.

——, B. Daudert, C. B. Garner, N. S. Oakley, A. E. Putnam, and A. B. White, 2017: Winter snow level rise in the Northern Sierra Nevada from 2008 to 2017. *Water*, **9**, 899, https://doi.org/10.3390/w9110899.

——, and Coauthors, 2020: Observations of an Extreme Atmospheric River Storm With a Diverse Sensor Network. *Earth and Space Science*, **7**, https://doi.org/10.1029/2020EA001129.

Heggli, A., B. J. Hatchett, A. Schwartz, T. Bardsley, and E. Hand, 2022: Toward snowpack runoff decision support. *iScience*, **25**, 104240, https://doi.org/10.1016/j.isci.2022.104240.

Henn, B., K. N. Musselman, L. Lestak, F. M. Ralph, and N. P. Molotch, 2020: Extreme Runoff Generation From Atmospheric River Driven Snowmelt During the 2017 Oroville Dam Spillways Incident. *Geophysical Research Letters*, **47**, e2020GL088189, https://doi.org/10.1029/2020GL088189.

Hersbach, H., and Coauthors, 2020: The ERA5 global reanalysis. *Quarterly Journal of the Royal Meteorological Society*, **146**, 1999–2049, https://doi.org/10.1002/qj.3803.

Hirashima, H., F. Avanzi, and N. Wever, 2019: Wet-Snow Metamorphism Drives the Transition From Preferential to Matrix Flow in Snow. *Geophysical Research Letters*, **46**, 14548–14557, https://doi.org/10.1029/2019GL084152.

Howat, I. M., and S. Tulaczyk, 2005: Climate sensitivity of spring snowpack in the Sierra

Nevada. *Journal of Geophysical Research: Earth Surface*, **110**, F04021, https://doi.org/10.1029/2005JF000356.

Hu, J. M., and A. W. Nolin, 2019: Snowpack Contributions and Temperature Characterization of Landfalling Atmospheric Rivers in the Western Cordillera of the United States. *Geophysical Research Letters*, **46**, 6663–6672, https://doi.org/10.1029/2019GL083564.

Huang, H., M. Fischella, Y. Liu, Z. Ban, J. Fayne, D. Li, K. Cavanaugh, and D. P. Lettenmaier, 2022: Changes in mechanisms and characteristics of Western U.S. floods over the last sixty years. *Geophysical Research Letters*, e2021GL097022, https://doi.org/10.1029/2021gl097022.

Huang, X., A. D. Hall, and N. Berg, 2018: Anthropogenic Warming Impacts on Today's Sierra Nevada Snowpack and Flood Risk. *Geophysical Research Letters*, **45**, 6215–6222, https://doi.org/10.1029/2018GL077432.

——, D. L. Swain, and A. D. Hall, 2020: Future precipitation increase from very high resolution ensemble downscaling of extreme atmospheric river storms in California. *Science Advances*, **6**, eaba1323, https://doi.org/10.1126/sciadv.aba1323.

Huning, L. S., and S. A. Margulis, 2017: Climatology of seasonal snowfall accumulation across the Sierra Nevada (USA): Accumulation rates, distributions, and variability. *Water Resources Research*, **53**, 6033–6049, https://doi.org/10.1002/2017WR020915.

——, and A. AghaKouchak, 2018: Mountain snowpack response to different levels of warming. *Proceedings of the National Academy of Sciences of the United States of America*, **115**, 10932–10937, https://doi.org/10.1073/pnas.1805953115.

——, and S. A. Margulis, 2018: Investigating the variability of high-elevation seasonal orographic snowfall enhancement and its drivers across sierra nevada, California. *Journal of*

Hydrometeorology, **19**, 47–67, https://doi.org/10.1175/JHM-D-16-0254.1.

Immerzeel, W. W., and Coauthors, 2020: Importance and vulnerability of the world's water towers. *Nature*, **577**, 364–369, https://doi.org/10.1038/s41586-019-1822-y.

Ingram, L. B., 2013: California megaflood: Lessons from a forgotten catastrophe. *Scientific American*, January.

Jennings, K. S., T. G. F. Kittel, and N. P. Molotch, 2018: Observations and simulations of the seasonal evolution of snowpack cold content and its relation to snowmelt and the snowpack energy budget. *Cryosphere*, **12**, https://doi.org/10.5194/tc-12-1595-2018.

Johnston, P. E., J. R. Jordan, A. B. White, D. A. Carter, D. M. Costa, and T. E. Ayers, 2017: The NOAA FM-CW Snow-Level Radar. *Journal of Atmospheric and Oceanic Technology*, **34**, 249–267, https://doi.org/10.1175/JTECH-D-16-0063.1.

Jordan, R., 1991: A one-dimensional temperature model for a snow cover: Technical documentation for SNTHERM. 89. *Cold Regions Research and Engineering Laboratory (US)*,.

Juras, R., S. Würzer, J. Pavlásek, T. Vitvar, and T. Jonas, 2017: Rainwater propagation through snowpack during rain-on-snow sprinkling experiments under different snow conditions. *Hydrology and Earth System Sciences*, **21**, 4973–4987, https://doi.org/10.5194/hess-21-4973-2017.

Kain, J. S., S. M. Gross, and M. E. Baldwin, 2000: The Melting Effect as a Factor in Precipitation-Type Forecasting. *Weather and Forecasting*, **15**, 700–714, https://doi.org/10.1175/1520-0434(2000)015<0700:TMEAAF>2.0.CO;2.

Kapnick, S., and A. Hall, 2010: Observed climate-snowpack relationships in California and their implications for the future. *Journal of Climate*, **23**, 3446–3456,

https://doi.org/10.1175/2010JCLI2903.1.

——, and ——, 2012: Causes of recent changes in western North American snowpack. *Climate Dynamics*, **38**, 1885–1899, https://doi.org/10.1007/s00382-011-1089-y.

Kattelmann, R., 1985: Macropores in Snowpacks of Sierra Nevada. *Annals of Glaciology*, **6**, 272–273, https://doi.org/10.3189/1985AoG6-1-272-273.

——, 1997a: Flooding from rain-on-snow events in the Sierra Nevada. *IAHS Publications-Series of Proceedings and Reports-Intern Assoc Hydrological Sciences*, Vol. 239 of, 59–65.

——, 1997b: Very Warm Storms and Sierra Nevada Snowpacks. *Western Snow Conference 1997*, 125–129.

——, and J. Dozier, 1999: Observations of snowpack ripening in the Sierra Nevada, California, U.S.A. *Journal of Glaciology*, **45**, 409–416, https://doi.org/10.1017/S002214300000126X.

Khanal, S., A. F. Lutz, W. W. Immerzeel, H. de Vries, N. Wanders, and B. J. J. M. van den Hurk, 2019: The Impact of Meteorological and Hydrological Memory on Compound Peak Flows in the Rhine River Basin. *Atmosphere*, **10**, 171, https://doi.org/10.3390/atmos10040171.

Kirchner, J., S. Godsey, R. Osterhuber, J. McConnell, and D. Penna, 2020: The pulse of a montane ecosystem: coupled daily cycles in solar flux, snowmelt, transpiration, groundwater, and streamflow at Sagehen and Independence Creeks, Sierra Nevada, USA. *Hydrology and Earth System Sciences*, **24**, 5095–5123, https://doi.org/10.5194/hess-24-5095-2020.

Kirchner, P. B., R. C. Bales, N. P. Molotch, J. Flanagan, and Q. Guo, 2014: LiDAR measurement of seasonal snow accumulation along an elevation gradient in the southern Sierra Nevada, California. *Hydrology and Earth System Sciences*, **18**, 4261–4275,

https://doi.org/10.5194/hess-18-4261-2014.

Kirshbaum, D. J., and R. B. Smith, 2008: Temperature and moist-stability effects on midlatitude orographic precipitation. *Quarterly Journal of the Royal Meteorological Society*, **134**, 1183–1199, https://doi.org/10.1002/qj.

Klos, P. Z., T. E. Link, and J. T. Abatzoglou, 2014: Extent of the rain-snow transition zone in the western U.S. under historic and projected climate. *Geophysical Research Letters*, **41**, 4560–4568, https://doi.org/10.1002/2014GL060500.

Knowles, N., M. D. Dettinger, and D. R. Cayan, 2006: Trends in snowfall versus rainfall in the western United States. *Journal of Climate*, **19**, 4545–4559, https://doi.org/10.1175/JCLI3850.1.

Koch, F., and Coauthors, 2019: Retrieval of Snow Water Equivalent, Liquid Water Content, and Snow Height of Dry and Wet Snow by Combining GPS Signal Attenuation and Time Delay. *Water Resources Research*, **55**, 4465–4487, https://doi.org/10.1029/2018WR024431.

Krajčí, P., L. Holko, R. A. P. Perdigão, and J. Parajka, 2014: Estimation of regional snowline elevation (RSLE) from MODIS images for seasonally snow covered mountain basins. *Journal of Hydrology*, **519**, 1769–1778, https://doi.org/10.1016/j.jhydrol.2014.08.064.

Kunkel, K. E., M. Palecki, L. Ensor, K. G. Hubbard, D. Robinson, K. Redmond, and D. Easterling, 2009: Trends in Twentieth-Century U.S. Snowfall Using a Quality-Controlled Dataset. *Journal of Atmospheric and Oceanic Technology*, **26**, 33–44, https://doi.org/10.1175/2008JTECHA1138.1.

Langenbrunner, B., D. J. Neelin, B. R. Lintner, and B. T. Anderson, 2015: Patterns of Precipitation Change and Climatological Uncertainty among CMIP5 Models, with a Focus on the Midlatitude Pacific Storm Track. *Journal of Climate*, **28**, 7857–7872,

https://doi.org/10.1175/JCLI-D-14-00800.1.

Lavers, D. A., G. Villarini, R. P. Allan, E. F. Wood, and A. J. Wade, 2012: The detection of atmospheric rivers in atmospheric reanalyses and their links to British winter floods and the large-scale climatic circulation. *Journal of Geophysical Research*, **117**, D20106, https://doi.org/10.1029/2012JD018027.

——, F. M. Ralph, D. E. Waliser, A. Gershunov, and M. D. Dettinger, 2015: Climate change intensification of horizontal water vapor transport in CMIP5. *Geophysical Research Letters*, **42**, 5617–5625, https://doi.org/10.1002/2015GL064672.

Li, D., M. L. Wrzesien, M. Durand, J. Adam, and D. P. Lettenmaier, 2017: How much runoff originates as snow in the western United States, and how will that change in the future? *Geophysical Research Letters*, **44**, 6163–6172, https://doi.org/10.1002/2017GL073551.

——, D. P. Lettenmaier, S. A. Margulis, and K. M. Andreadis, 2019: The Role of Rain-on-Snow in Flooding Over the Conterminous United States. *Water Resources Research*, **55**, 8492–8513, https://doi.org/10.1029/2019WR024950.

López-Moreno, J. I., J. W. Pomeroy, E. Morán-Tejeda, J. Revuelto, F. M. Navarro-Serrano, I. Vidaller, and E. Alonso-González, 2021: Changes in the frequency of global high mountain rain-on-snow events due to climate warming. *Environmental Research Letters*, **16**, 094021, https://doi.org/10.1088/1748-9326/ac0dde.

Loukas, A., and M. C. Quick, 1996: Physically-based estimation of lag time for forested mountainous watersheds. *Hydrological Sciences Journal*, **41**, 1–19, https://doi.org/10.1080/02626669609491475.

Lundquist, J. D., and B. Huggett, 2008: Evergreen trees as inexpensive radiation shields for temperature sensors. *Water Resources Research*, **44**, W00D04,

https://doi.org/10.1029/2008WR006979.

——, P. J. Neiman, B. Martner, A. B. White, D. J. Gottas, and F. M. Ralph, 2008: Rain versus snow in the Sierra Nevada, California: Comparing doppler profiling radar and surface observations of melting level. *Journal of Hydrometeorology*, **9**, 194–211, https://doi.org/10.1175/2007JHM853.1.

——, J. R. Minder, P. J. Neiman, and E. Sukovich, 2010: Relationships between Barrier Jet Heights, Orographic Precipitation Gradients, and Streamflow in the Northern Sierra Nevada. *Journal of Hydrometeorology*, **11**, 1141–1156, https://doi.org/10.1175/2010JHM1264.1.

——, M. Hughes, B. Henn, E. D. Gutmann, B. Livneh, J. Dozier, and P. Neiman, 2015: High-elevation precipitation patterns: Using snow measurements to assess daily gridded datasets across the Sierra Nevada, California. *Journal of Hydrometeorology*, **16**, 1773–1792, https://doi.org/10.1175/JHM-D-15-0019.1.

——, ——, E. D. Gutmann, and S. Kapnick, 2019: Our Skill in Modeling Mountain Rain and Snow is Bypassing the Skill of Our Observational Networks. *Bulletin of the American Meteorological Society*, **100**, 2473–2490, https://doi.org/10.1175/BAMS-D-19-0001.1.

Lute, A. C., and J. T. Abatzoglou, 2014: Role of extreme snowfall events in interannual variability of snowfall accumulation in the western United States. *Water Resources Research*, **50**, 2874–2888, https://doi.org/10.1111/j.1752-1688.1969.tb04897.x.

Maher, P., M. E. Kelleher, P. G. Sansom, and J. Methven, 2020: Is the subtropical jet shifting poleward? *Climate Dynamics*, **54**, 1741–1759, https://doi.org/10.1007/s00382-019-05084-6.

Marks, D., and J. Dozier, 1992: Climate and Energy Exchange at the Snow Surface in the Alpine Region of the Sierra Nevada 2. Snow Cover Energy Balance. *Water Resources Research*,

28, 3043–3054, https://doi.org/10.1029/92WR01483.

——, J. Kimball, D. Tingey, and T. Link, 1998: The sensitivity of snowmelt processes to climate conditions and forest cover during rain-on-snow: a case study of the 1996 Pacific Northwest flood. *Hydrological Processes*, **12**, 1569–1587, https://doi.org/10.1002/(SICI)1099-1085(199808/09)12:10/11<1569::AID-HYP682>3.0.CO;2-L.

Marks, D. G., A. Winstral, M. L. Reba, J. W. Pomeroy, and M. Kumar, 2013: An evaluation of methods for determining during-storm precipitation phase and the rain/snow transition elevation at the surface in a mountain basin. *Advances in Water Resources*, **55**, 98–110, https://doi.org/10.1016/j.advwatres.2012.11.012.

Marsh, P., and M.-K. Woo, 1984: Wetting Front Advance and Freezing of Meltwater Within a Snow Cover 1. Observations in the Canadian Arctic. *Water Resources Research*, **20**, 1853–1864, https://doi.org/10.1029/WR020i012p01853.

Masuda, M., A. Yatagai, K. Kamiguchi, and K. Tanaka, 2019: Daily Adjustment for Wind-Induced Precipitation Undercatch of Daily Gridded Precipitation in Japan. *Earth and Space Science*, **6**, 1469–1479, https://doi.org/10.1029/2019EA000659.

Maurer, E. P., 2007: Uncertainty in hydrologic impacts of climate change in the Sierra Nevada, California, under two emissions scenarios. *Climatic Change*, **82**, 309–325, https://doi.org/10.1007/s10584-006-9180-9.

——, and C. Mass, 2006: Using radar data to partition precipitation into rain and snow in a hydrologic model. *Journal of Hydrologic Engineering*, **11**, 214–221, https://doi.org/10.1061/(ASCE)1084-0699(2006)11:3(214).

Mazurkiewicz, A. B., D. G. Callery, and J. J. Mcdonnell, 2008: Assessing the controls of the snow energy balance and water available for runoff in a rain-on-snow environment. *Journal*

of Hydrology, **354**, 1–14, https://doi.org/10.1016/j.jhydrol.2007.12.027.

McCabe, G. J., M. P. Clark, and L. E. Hay, 2007: Rain-on-snow events in the western united states. *Bulletin of the American Meteorological Society*, **88**, 319–328, https://doi.org/10.1175/BAMS-88-3-319.

——, D. M. Wolock, and M. Valentin, 2018: Warming is Driving Decreases in Snow Fractions While Runoff Efficiency Remains Mostly Unchanged in Snow-Covered Areas of the Western United States. *Journal of Hydrometeorology*, **19**, 803–814, https://doi.org/10.1175/JHM-D-17-0227.1.

McGowan, H. A., K. Borthwick, A. Schwartz, J. Callow, S. P. Bilish, and S. Browning, 2021: Atmospheric Rivers: An overlooked threat to the marginal snowpack of the Australian Alps. *Journal of Hydrometeorology*, **22**, 2521–2532, https://doi.org/10.1175/JHM-D-20-0293.1.

McGuire, M., A. W. Wood, A. F. Hamlet, and D. P. Lettenmaier, 2006: Use of Satellite Data for Streamflow and Reservoir Storage Forecasts in the Snake River Basin. *Journal of Water Resources Planning and Management*, **132**, 97–110, https://doi.org/10.1061/(asce)0733-9496(2006)132:2(97).

McNamara, J. P., D. Chandler, M. Seyfried, and S. Achet, 2005: Soil moisture states, lateral flow, and streamflow generation in a semi-arid, snowmelt-driven catchment. *Hydrological Processes*, **19**, 4023–4038, https://doi.org/10.1002/hyp.5869.

Medina, S., B. F. Smull, R. A. Houze, and M. Steiner, 2005: Cross-Barrier Flow during Orographic Precipitation Events : Results from MAP and IMPROVE. *Journal of the Atmospheric Sciences*, **62**, 3580–3598, https://doi.org/10.1175/JAS3554.1.

Mejia, J. F., J. Huntington, B. J. Hatchett, D. Koracin, and R. G. Niswonger, 2012: Linking Global Climate Models to an Integrated Hydrologic Model: Using an Individual Station

Downscaling Approach. *Journal of Contemporary Water Research & Education*, **147**, 17–27, https://doi.org/10.1111/j.1936-704x.2012.03100.x.

Meromy, L., N. P. Molotch, T. E. Link, S. R. Fassnacht, and R. Rice, 2013: Subgrid variability of snow water equivalent at operational snow stations in the western USA. *Hydrological Processes*, **27**, 2383–2400, https://doi.org/10.1002/hyp.9355.

Meyer, J. D. D., J. Jin, and S.-Y. Wang, 2012: Systematic Patterns of the Inconsistency between Snow Water Equivalent and Accumulated Precipitation as Reported by the Snowpack Telemetry Network. *Journal of Hydrometeorology*, **13**, 1970–1976, https://doi.org/10.1175/JHM-D-12-066.1.

Michaelis, A. C., A. Gershunov, A. Weyant, M. A. Fish, T. Shulgina, and F. M. Ralph, 2022: Atmospheric river precipitation enhanced by climate change: A case study of the storm that contributed to California's Oroville Dam crisis. *Earth's Future*, e2021EF002537, https://doi.org/10.1029/2021EF002537.

Miller, D., J. Forsythe, S. Kusselson, W. S. Iii, J. Yin, X. Zhan, and R. Ferraro, 2021: A Study of Two Impactful Heavy Rainfall Events in the Southern Appalachian Mountains during Early 2020 , Part I; Societal Impacts, Synoptic Overview, and Historical Context. *Remote Sensing*, **13**, 2452, https://doi.org/10.3390/rs13132452.

Minder, J. R., and D. E. Kingsmill, 2013: Mesoscale Variations of the Atmospheric Snow Line over the Northern Sierra Nevada: Multiyear Statistics, Case Study, and Mechanisms. *Journal of the Atmospheric Sciences*, **70**, 916–938, https://doi.org/10.1175/JAS-D-12-0194.1.

——, D. R. Durran, and G. H. Roe, 2011: Mesoscale controls on the mountainside snow line. *Journal of the Atmospheric Sciences*, **68**, 2107–2127, https://doi.org/10.1175/JAS-D-10-

05006.1.

Minola, L., F. Zhang, C. Azorin-Molina, A. A. S. Pirooz, R. G. J. Flay, H. Hersbach, and D. Chen, 2020: Near-surface mean and gust wind speeds in ERA5 across Sweden: towards an improved gust parametrization. *Climate Dynamics*, **55**, 887–907, https://doi.org/10.1007/s00382-020-05302-6.

Mizukami, N., V. Koren, M. Smith, D. Kingsmill, Z. Zhang, B. Cosgrove, and Z. Cui, 2013: The impact of precipitation type discrimination on hydrologic simulation: Rain-snow partitioning derived from HMT-west radar-detected brightband height versus surface temperature data. *Journal of Hydrometeorology*, **14**, 1139–1158, https://doi.org/10.1175/JHM-D-12-035.1.

Molotch, N. P., and R. C. Bales, 2005: Scaling snow observations from the point to the grid element: Implications for observation network design. *Water Resources Research*, **41**, W11421, https://doi.org/10.1029/2005WR004229.

——, and ——, 2006: SNOTEL representativeness in the Rio Grande headwaters on the basis of physiographics and remotely sensed snow cover persistence. *Hydrological Processes*, **20**, 723–739, https://doi.org/10.1002/hyp.6128.

Mote, P. W., 2006: Climate-Driven Variability and Trends in Mountain Snowpack in Western North America. *Journal of Climate*, **19**, 6209–6220, https://doi.org/10.1175/JCLI3971.1.

——, S. Li, D. P. Lettenmaier, M. Xiao, and R. Engel, 2018: Dramatic declines in snowpack in the western US. *npj Climate and Atmospheric Science*, **1**, 1–6, https://doi.org/10.1038/s41612-018-0012-1.

Muñoz Sabater, J., 2019: ERA5-Land hourly data from 1981 to present. Copernicus Climate Change Service (C3S) Climate Data Store (CDS). (Accessed on 30-Sep-2021).

https://doi.org/10.24381/cds.e2161bac.

Musselman, K. N., N. P. Molotch, and P. D. Brooks, 2008: Effects of vegetation on snow accumulation and ablation in a mid-latitude sub-alpine forest. *Hydrological Processes*, **22**, 2767–2776, https://doi.org/10.1002/hyp.7050.

——, F. Lehner, K. Ikeda, M. P. Clark, A. F. Prein, C. Liu, M. Barlage, and R. Rasmussen, 2018: Projected increases and shifts in rain-on-snow flood risk over western North America. *Nature Climate Change*, **8**, 808–812, https://doi.org/10.1038/s41558-018-0236-4.

NASA, NOAA, and U. S. Air Force, 1976: *U.S. Standard Atmosphere, 1976*. https://apps.dtic.mil/dtic/tr/fulltext/u2/a035728.pdf.

Neelin, D. J., B. Langenbrunner, J. E. Meyerson, A. Hall, and N. Berg, 2013: California Winter Precipitation Change under Global Warming in the Coupled Model Intercomparison Project Phase 5 Ensemble. *Journal of Climate*, **26**, 6238–6256, https://doi.org/10.1175/JCLI-D-12-00514.1.

Nippgen, F., B. L. McGlynn, R. E. Emanuel, and J. M. Vose, 2016: Watershed memory at the Coweeta Hydrologic Laboratory: The effect of past precipitation and storage on hydrologic response. *Water Resources Research*, **52**, 1673–1695, https://doi.org/10.1002/2015WR018196.

NRCS, U., 2004: National Engineering Handbook: Part 630—Hydrology, Chapter 15: Time of Concentration. *United States Department of Agriculture-Natural Resources Conservation Service,*.

O'Hara, B. F., M. L. Kaplan, and S. J. Underwood, 2009: Synoptic Climatological Analyses of Extreme Snowfalls in the Sierra Nevada. *Weather and Forecasting*, **24**, 1610–1624, https://doi.org/10.1175/2009WAF2222249.1.

Oyler, J. W., S. Z. Dobrowski, A. P. Ballantyne, A. E. Klene, and S. W. Running, 2015: Artificial amplification of warming trends across the mountains of the western United States Jared. *Geophysical Research Letters*, **42**, 153–161, https://doi.org/10.1002/2014GL062803.

Painter, T. H., K. Rittger, C. McKenzie, P. Slaughter, R. E. Davis, and J. Dozier, 2009: Retrieval of subpixel snow covered area, grain size, and albedo from MODIS. *Remote Sensing of Environment*, **113**, 868–879, https://doi.org/10.1016/j.rse.2009.01.001.

Pathak, T. B., M. L. Maskey, J. A. Dahlberg, F. Kearns, K. M. Bali, and D. Zaccaria, 2018: Climate Change Trends and Impacts on California Agriculture: A Detailed Review. *Agronomy*, **8**, 25, https://doi.org/10.3390/agronomy8030025.

Petersky, R. S., and A. A. Harpold, 2018: Now you see it, now you don't: A case study of ephemeral snowpacks and soil moisture response in the Great Basin, USA. *Hydrology and Earth System Sciences*, **22**, 4891–4906, https://doi.org/10.5194/hess-22-4891-2018.

Pierce, D. W., and D. R. Cayan, 2013: The uneven response of different snow measures to human-induced climate warming. *Journal of Climate*, **26**, 4148–4167, https://doi.org/10.1175/JCLI-D-12-00534.1.

——, and Coauthors, 2008: Attribution of declining Western U.S. Snowpack to human effects. *Journal of Climate*, **21**, 6425–6444, https://doi.org/10.1175/2008JCLI2405.1.

Polade, S. D., A. Gershunov, D. R. Cayan, M. D. Dettinger, and D. W. Pierce, 2017: Precipitation in a warming world: Assessing projected hydro-climate changes in California and other Mediterranean climate regions. *Scientific Reports*, **7**, 1–10, https://doi.org/10.1038/s41598-017-11285-y.

Pomeroy, J. W., X. Fang, and D. G. Marks, 2016: The cold rain-on-snow event of June 2013 in the Canadian Rockies — characteristics and diagnosis. *Hydrological Processes*, **30**, 2899–

2914, https://doi.org/10.1002/hyp.10905.

Priestley, A., B. Kulessa, R. Essery, Y. Lejeune, E. Le Gac, and J. Blackford, 2021: Towards the development of an automated electrical self-potential sensor of melt and rainwater flow in snow. *Journal of Glaciology*, 1–13, https://doi.org/10.1017/jog.2021.128.

Rangwala, I., T. Bardsley, M. Penscinski, and J. Miller, 2015: SNOTEL Sensor Upgrade has Caused Temperature Record Inhomogeneities for the Intermountain West: Implications for Climate Change Impact Assessments. *Western Water Assessment Climate Research Briefing, Boulder, Colorado*.

Rhoades, A. M., P. A. Ullrich, and C. M. Zarzycki, 2018: Projecting 21st century snowpack trends in western USA mountains using variable-resolution CESM. *Climate Dynamics*, **50**, 261–288, https://doi.org/10.1007/s00382-017-3606-0.

——, and Coauthors, 2020: The Shifting Scales of Western U.S. Landfalling Atmospheric Rivers Under Climate Change. *Geophysical Research Letters*, **47**, e2020GL089096, https://doi.org/10.1029/2020GL089096.

Riedel, K. S., and A. Sidorenko, 1995: Minimum bias multiple taper spectral estimation. *IEEE Transactions on Signal Processing*, **43**, 188–195, https://doi.org/10.1109/78.365298.

Robles, M. D., J. C. Hammond, S. K. Kampf, J. A. Biederman, and E. M. C. Demaria, 2021: Winter inputs buffer streamflow sensitivity to snowpack losses in the salt river watershed in the lower colorado river basin. *Water*, **13**, 3, https://doi.org/10.3390/w13010003.

Roe, G. H., 2005: Orographic recipitation. *Annual Reviews in Earth and Planetary Science*, **33**, 645–671, https://doi.org/10.1146/annurev.earth.33.092203.122541.

Rössler, O., P. Froidevaux, U. Börst, R. Rickli, O. Martius, and R. Weingartner, 2014: Retrospective analysis of a nonforecasted rain-on-snow flood in the Alps-A matter of model

limitations or unpredictable nature? *Hydrology and Earth System Sciences*, **18**, 2265–2285, https://doi.org/10.5194/hess-18-2265-2014.

Rücker, A., S. Boss, J. W. Kirchner, and J. Von Freyberg, 2019: Monitoring snowpack outflow volumes and their isotopic composition to better understand streamflow generation during rain-on-snow events. *Hydrology and Earth System Sciences*, **23**, 2983–3005, https://doi.org/10.5194/hess-23-2983-2019.

Safeeq, M., S. Shukla, I. Arismendi, G. E. Grant, S. L. Lewis, and A. Nolin, 2016: Influence of winter season climate variability on snow–precipitation ratio in the western United States. *International Journal of Climatology*, **36**, 3175–3190, https://doi.org/10.1002/joc.4545.

——, R. R. Bart, N. F. Pelak, C. K. Singh, D. N. Dralle, P. Hartsough, and J. W. Wagenbrenner, 2021: How realistic are water-balance closure assumptions? A demonstration from the southern sierra critical zone observatory and kings river experimental watersheds. *Hydrological Processes*, **35**, e14199, https://doi.org/10.1002/hyp.14199.

Scalzitti, J., C. Strong, and A. Kochanski, 2016: Climate change impact on the roles of temperature and precipitation in western U.S. snowpack variability. *Geophysical Research Letters*, **43**, 5361–5369, https://doi.org/10.1002/2016GL068798.1.

Schaefer, G. L., and D. E. Johnson, 1992: Development and operation of the SNOTEL system in the western United States. *Proc. United States/People's Republic of China Flood Forecasting Symp*, Vol. 1 of, 29–48.

Seligman, Z. M., J. T. Harper, and M. P. Maneta, 2014: Changes to snowpack energy state from spring storm events, Columbia River headwaters, Montana. *Journal of Hydrometeorology*, **15**, 159–170, https://doi.org/10.1175/JHM-D-12-078.1.

Serreze, M. C., M. P. Clark, R. L. Armstrong, A. McGinnis, and R. S. Pulwarty, 1999:

Characteristics of the western United States snowpack from snowpack telemetry (SNOTEL) data. *Water Resources Research*, **35**, 2145–2160, https://doi.org/10.1029/1999WR900090.

Serreze, M. C., M. P. Clark, and A. Frei, 2001: Characteristics of large snowfall events in the montane western United States as examined using snowpack telemetry (SNOTEL) data. *Water Resources Research*, **37**, 675–688, https://doi.org/10.1029/2000WR900307.

Siirila-Woodburn, E. R., and Coauthors, 2021: A low-to-no snow future and its impacts on water resources in the western United States. *Nature Reviews Earth & Environment*, **2**, 800–819, https://doi.org/10.1038/s43017-021-00219-y.

Singh, P., G. Spitzbart, H. Hu, and H. W. Weinmeister, 1997: Hydrological response of snowpack under rain-on-snow events: a field study. *Journal of Hydrology*, **202**, 1–20, https://doi.org/10.1016/S0022-1694(97)00004-8.

Skiles, S. M., M. Flanner, J. M. Cook, M. Dumont, and T. H. Painter, 2018: Radiative forcing by light-absorbing particles in snow. *Nature Climate Change*, **8**, 964–971, https://doi.org/10.1038/s41558-018-0296-5.

Smith, R. B., Q. Jiang, M. G. Fearon, and P. Tabary, 2003: Orographic precipitation and air mass transformation : An Alpine example. *Quarterly Journal of the Royal Meteorological Society*, **129**, 433–454, https://doi.org/10.1256/qj.01.212.

Sterle, K., B. J. Hatchett, L. Singletary, and G. Pohll, 2019: Hydroclmate variability in snow-fed rivers systems: Local water managers' perspectives on adapting to the new normal. *Bulletin of the American Meteorological Society*, **100**, 1031–1048, https://doi.org/10.1175/BAMS-D-18-0031.1.

Stewart, I. T., D. R. Cayan, and M. D. Dettinger, 2005: Changes toward earlier streamflow timing across western North America. *Journal of Climate*, **18**, 1136–1155,

https://doi.org/10.1175/JCLI3321.1.

Stewart, R. E., J. D. Marwitz, J. C. Pace, and R. E. Carbone, 1984: Characteristics through the Melting Layer of Stratiform Clouds. *Journal of Atmospheric Sciences*, **41**, 3227–3237, https://doi.org/10.1175/1520-0469(1984)041<3227:CTTMLO>2.0.CO;2.

Sun, F., A. Hall, M. Schwartz, D. B. Walton, and N. Berg, 2016: Twenty-first-century snowfall and snowpack changes over the Southern California mountains. *Journal of Climate*, **29**, 91–110, https://doi.org/10.1175/JCLI-D-15-0199.1.

——, N. Berg, A. Hall, M. Schwartz, and D. Walton, 2019: Understanding End-of-Century Snowpack Changes Over California's Sierra Nevada. *Geophysical Research Letters*, **46**, 933–943, https://doi.org/10.1029/2018GL080362.

Tamarin-Brodsky, T., and Y. Kaspi, 2017: Enhanced poleward propagation of storms under climate change. *Nature Geoscience*, **10**, 908–913, https://doi.org/10.1038/s41561-017-0001-8.

Tarouilly, E., D. Li, and D. P. Lettenmaier, 2021: Western U.S. Superfloods in the Recent Instrumental Record. *Water Resources Research*, **57**, e2020WR029287, https://doi.org/10.1029/2020WR029287.

Thomson, D. J., 1982: Spectrum Estimation and Harmonic Analysis. *Proceedings of the IEEE*, **70**, 1055–1096, https://doi.org/10.1109/PROC.1982.12433.

Trubilowicz, J. W., and R. D. Moore, 2017: Quantifying the role of the snowpack in generating water available for run-off during rain-on-snow events from snow pillow records. *Hydrological Processes*, **31**, 4136–4150, https://doi.org/10.1002/hyp.11310.

Vano, J. A., M. D. Dettinger, R. Cifelli, D. Curtis, A. Dufour, K. Miller, J. R. Olsen, and A. M. Wilson, 2019: Hydroclimatic extremes as challenges for the water management community:

Lessons from Oroville Dam and Hurricane Harvey [in "Explaining Extremes of 2017 from a Climate Perspective"]. *Bulletin of the American Meteorological Society*, **100**, S9–S14, https://doi.org/10.1175/BAMS-D-18-0135.1.

Viviroli, D., H. H. Du, B. Messerli, M. Meybeck, and R. Weingartner, 2007: Mountains of the world, water towers for humanity: Typology, mapping, and global significance. *Water Resources Research*, **43**, W07447, https://doi.org/10.1029/2006WR005653.

Wankiewicz, A., 1978: Water pressure in ripe snowpacks. *Water Resources Research*, **14**, 593–600, https://doi.org/10.1029/WR014i004p00593.

Wasko, C., R. Nathan, and M. C. Peel, 2020: Trends in Global Flood and Streamflow Timing Based on Local Water Year. *Water Resources Research*, **56**, e2020WR027233, https://doi.org/10.1029/2020WR027233.

Wayand, N. E., J. D. Lundquist, and M. P. Clark, 2015: Modeling the influence of hypsometry, vegetation, and storm energy on snowmelt contributions to basins during rain-on-snow floods. *Water Resources Research*, **51**, 8551–8569, https://doi.org/10.1002/2014WR016576.

Webb, R. W., S. R. Fassnacht, and M. N. Gooseff, 2018a: Hydrologic flow path development varies by aspect during spring snowmelt in complex subalpine terrain. *The Cryosphere*, **12**, 287–300, https://doi.org/10.5194/tc-12-287-2018.

——, M. W. Williams, and T. A. Erickson, 2018b: The Spatial and Temporal Variability of Meltwater Flow Paths: Insights From a Grid of Over 100 Snow Lysimeters. *Water Resources Research*, **54**, 1146–1160, https://doi.org/10.1002/2017WR020866.

——, K. Jennings, S. Finsterle, and S. R. Fassnacht, 2021: Two-dimensional liquid water flow through snow at the plot scale in continental snowpacks: Simulations and field data

comparisons. *Cryosphere*, **15**, 1423–1434, https://doi.org/10.5194/tc-15-1423-2021.

Welty, J., and X. Zeng, 2021: Characteristics and Causes of Extreme Snowmelt over the Conterminous United States. *Bulletin of the American Meteorological Society*, **102**, E1526–E1542, https://doi.org/10.1175/bams-d-20-0182.1.

Westerling, A. L., 2016: Increasing western US forest wildfire activity: sensitivity to changes in the timing of spring. *Philosophical Transactions of the Royal Society B: Biological Sciences*, **371**, 20150178, https://doi.org/10.1098/rstb.2015.0178.

——, H. G. Hidalgo, D. R. Cayan, and T. W. Swetnam, 2006: Warming and Earlier Spring Increase Western U.S. Forest Wildfire Activity. *Science*, **313**, 940–944, https://doi.org/10.1126/science.1128834.

Wever, N., S. Würzer, C. Fierz, and M. Lehning, 2016: Simulating ice layer formation under the presence of preferential flow in layered snowpacks. *The Cryosphere*, **10**, 2731–2744, https://doi.org/10.5194/tc-10-2731-2016.

White, A. B., D. J. Gottas, E. T. Strem, F. M. Ralph, and P. J. Neiman, 2002: An Automated Brightband Height Detection Algorithm for Use with Doppler Radar Spectral Moments. *Journal of Atmospheric and Oceanic Technology*, **19**, 687–697, https://doi.org/10.1175/1520-0426(2002)019<0687:AABHDA>2.0.CO;2.

——, B. J. Moore, D. J. Gottas, and P. J. Neiman, 2019: Winter storm conditions leading to excessive runoff above California's Oroville dam during January and February 2017. *Bulletin of the American Meteorological Society*, **100**, 55–69, https://doi.org/10.1175/BAMS-D-18-0091.1.

Wlostowski, A. N., and Coauthors, 2021: Signatures of Hydrologic Function Across the Critical Zone Observatory Network. *Water Resources Research*, **57**,

https://doi.org/10.1029/2019WR026635.

Würzer, S., T. Jonas, N. Wever, and M. Lehning, 2016: Influence of Initial Snowpack Properties on Runoff Formation during Rain-on-Snow Events. *Journal of Hydrometeorology*, **17**, 1801–1815, https://doi.org/10.1175/JHM-D-15-0181.1.

——, N. Wever, R. Juras, M. Lehning, and T. Jonas, 2017: Modelling liquid water transport in snow under rain-on-snow conditions - Considering preferential flow. *Hydrology and Earth System Sciences*, **21**, 1741–1756, https://doi.org/10.5194/hess-21-1741-2017.

Yamaguchi, S., H. Hirashima, and Y. Ishii, 2018: Year-to-year changes in preferential flow development in a seasonal snowpack and their dependence on snowpack conditions. *Cold Regions Science and Technology*, **149**, 95–105, https://doi.org/10.1016/j.coldregions.2018.02.009.

Yuba Water Agency, 2018: *2017-2018 Annual Monitoring and Measuring Report*. https://www.yubawater.org/Archive/ViewFile/Item/290.

Zappa, G., 2019: Regional Climate Impacts of Future Changes in the Mid–Latitude Atmospheric Circulation: a Storyline View. *Current Climate Change Reports*, **5**, 358–371, https://doi.org/10.1007/s40641-019-00146-7.

Zeng, X., P. D. Broxton, and N. Dawson, 2018: Snowpack Change From 1982 to 2016 Over Conterminous United States. *Geophysical Research Letters*, **45**, 12,940-12,947, https://doi.org/10.1029/2018GL079621.